A UNITED STATES DEPARTMENT OF COMMERCE PUBLICATION

SECTION A

JOURNAL OF RESEARCH

of the NATIONAL BUREAU OF STANDARDS

Volume 76A, Number 1 Jan.-Feb. 1972

Physics and Chemistry

U.S. DEPARTMENT OF COMMERCE National Bureau of Standards

Journal of Research

of the

National Bureau of Standards

A. Physics and Chemistry

Jan.–Feb. • 1972

VOLUME • 76A

NUMBER • 1

Editor: C. W. Beckett

Associate Editor: D. D. Wagman

Publication dates:
Feb. 1, Apr. 1, June 1, Aug. 1, Oct. 1, Dec. 1, 1972

J. Res. Nat. Bur. Stand. (U.S.), A
CODEN: JNBAA 76A (1) 1–66 (1972)

JOURNAL OF RESEARCH

The National Bureau of Standards Journal of Research reports research and development in the fields of activity shown at right. Also included from time to time are survey articles on topics closely related to the Bureau's scientific and technical program.

The Journal is published in three separate sections as follows:

A. Physics and Chemistry

Contains papers of interest primarily to scientists working in these fields. Issued six times a year. Annual subscription: domestic, $9.50; foreign, $11.75. Single copy, varies.

B. Mathematical Sciences

Presents studies and compilations designed mainly for the mathematician and the theoretical physicist. Issued quarterly. Annual subscription: domestic, $5.00; foreign, $6.25. Single copy, $1.25.

C. Engineering and Instrumentation

Reports research and development results of interest chiefly to the engineer and the applied scientist. Issued quarterly. Annual subscription: domestic, $5.00; foreign, $6.25. Single copy, $1.25.

The National Bureau of Standards[1] was established by an act of Congress March 3, 1901. The Bureau's overall goal is to strengthen and advance the Nation's science and technology and facilitate their effective application for public benefit. To this end, the Bureau conducts research and provides: (1) a basis for the Nation's physical measurement system, (2) scientific and technological services for industry and government, (3) a technical basis for equity in trade, and (4) technical services to promote public safety. The Bureau consists of the Institute for Basic Standards, the Institute for Materials Research, the Institute for Applied Technology, the Center for Computer Sciences and Technology, and the Office for Information Programs.

THE INSTITUTE FOR BASIC STANDARDS provides the central basis within the United States of a complete and consistent system of physical measurement; coordinates that system with measurement systems of other nations; and furnishes essential services leading to accurate and uniform physical measurements throughout the Nation's scientific community, industry, and commerce. The Institute consists of a Center for Radiation Research, an Office of Measurement Services and the following divisions:

Applied Mathematics—Electricity—Heat—Mechanics—Optical Physics—Linac Radiation[2]—Nuclear Radiation[2]—Applied Radiation[2]—Quantum Electronics[3]—Electromagnetics[3]—Time and Frequency[3]—Laboratory Astrophysics[3]—Cryogenics[3].

THE INSTITUTE FOR MATERIALS RESEARCH conducts materials research leading to improved methods of measurement, standards, and data on the properties of well-characterized materials needed by industry, commerce, educational institutions, and Government; provides advisory and research services to other Government agencies; and develops, produces, and distributes standard reference materials. The Institute consists of the Office of Standard Reference Materials and the following divisions:

Analytical Chemistry—Polymers—Metallurgy—Inorganic Materials—Reactor Radiation—Physical Chemistry.

THE INSTITUTE FOR APPLIED TECHNOLOGY provides technical services to promote the use of available technology and to facilitate technological innovation in industry and Government; cooperates with public and private organizations leading to the development of technological standards (including mandatory safety standards), codes and methods of test; and provides technical advice and services to Government agencies upon request. The Institute also monitors NBS engineering standards activities and provides liaison between NBS and national and international engineering standards bodies. The Institute consists of the following technical divisions and offices:

Engineering Standards Services—Weights and Measures—Flammable Fabrics—Invention and Innovation—Vehicle Systems Research—Product Evaluation Technology—Building Research—Electronic Technology—Technical Analysis—Measurement Engineering.

THE CENTER FOR COMPUTER SCIENCES AND TECHNOLOGY conducts research and provides technical services designed to aid Government agencies in improving cost effectiveness in the conduct of their programs through the selection, acquisition, and effective utilization of automatic data processing equipment; and serves as the principal focus within the executive branch for the development of Federal standards for automatic data processing equipment, techniques, and computer languages. The Center consists of the following offices and divisions:

Information Processing Standards—Computer Information—Computer Services—Systems Development—Information Processing Technology.

THE OFFICE FOR INFORMATION PROGRAMS promotes optimum dissemination and accessibility of scientific information generated within NBS and other agencies of the Federal Government; promotes the development of the National Standard Reference Data System and a system of information analysis centers dealing with the broader aspects of the National Measurement System; provides appropriate services to ensure that the NBS staff has optimum accessibility to the scientific information of the world, and directs the public information activities of the Bureau. The Office consists of the following organizational units:

Office of Standard Reference Data—Office of Technical Information and Publications—Library—Office of International Relations.

[1] Headquarters and Laboratories at Gaithersburg, Maryland, unless otherwise noted; mailing address Washington, D.C. 20234.
[2] Part of the Center for Radiation Research.
[3] Located at Boulder, Colorado 80302.

U.S. DEPARTMENT OF COMMERCE
Maurice H. Stans, Secretary

NATIONAL BUREAU OF STANDARDS
Lewis M. Branscomb, Director

Order all publications from the Superintendent of Documents
U.S. Government Printing Office, Washington, D.C. 20402

Use of funds for printing this publication approved by the Director of the Bureau of the Budget (June 22, 1966).

JOURNAL OF RESEARCH of the National Bureau of Standards — A. Physics and Chemistry
Vol. 76A, No. 1, January–February 1972

The Absorption Spectra of Krypton and Xenon in the Wavelength Range 330–600 Å

K. Codling* and R. P. Madden

Institute for Basic Standards, National Bureau of Standards, Washington, D.C. 20234

(September 20, 1971)

A total of 153 krypton resonances in the spectral region 330–500 Å and 253 xenon resonances in the spectral region 375–600 Å are reported. A detailed listing of the resonances is given, with wavelength and line shape information. The analysis of the spectra is very incomplete and will require detailed theoretical calculation to significantly improve it. In Kr, 45 resonances and in Xe, 56 resonances have been grouped into probable Rydberg series, for which classifications are suggested. The resonances are due, in the main, to either the excitation of the inner subshell "s" electron ($s^2p^6 \rightarrow sp^6np$) or to the excitation of two of the outer "p" electrons simultaneously ($s^2p^6 \rightarrow s^2p^4nln'l'$). These high-lying excited states autoionize, resulting in resonances with window-, asymmetric-, or absorption-type profiles. Where possible, comparisons are made with previous work.

Key words: Autoionization; far ultraviolet; krypton; photoionization; resonances; xenon.

1. Introduction

This communication is intended as the final report on the absorption spectra of the noble gases He through Xe, observed in the wavelength range 80–600 Å. Earlier papers have dealt with the discovery and analysis (in some cases tentative) of the structure in the photoionization continuua of He[1],[1] Ne[2], and Ar[3]. We present here the spectra of Kr and Xe in the wavelength range 330–600 Å. Two previous publications have described the structure observed between 80 and 200 Å, due to the excitation of a single inner-shell d electron[4] and also the simultaneous excitation of an outer-shell p and an inner-shell d electron[5]. (The excitation of the outer p electron had been observed many years before [6].)

In the wavelength range 400–500 Å, Samson [7] observed two distinct resonances in the photoionization continuum of Kr using a many-lined spark discharge as a background source. Subsequently, many more autoionizing states in both Kr and Xe between 380 and 600 Å were reported [8] and recently, highlights of the present, more detailed experimental observations of the Kr and Xe spectra have been published [9]. In an accompanying paper [10], absolute cross-section measurements were made in the region of some of the more prominent resonances.

The following analysis of the Kr and Xe spectra is necessarily far from complete. The breakdown of strict L–S coupling, evident throughout the Ar spectrum, is even more pronounced in Kr and Xe. Consequently, considerable theoretical work is required, of an *ab initio* type, before a reasonable analysis of the Kr and Xe spectra can be made. In the hope of stimulating such calculations on noble gas atoms, we present here final numbers on wavelengths of the resonances observed, along with a rough guide as to the profiles of some of the resonances. The accompanying spectra and densitometer traces together with the published resonance profiles [10] may be helpful in comparing theoretical predictions with the experimental observations, at least for the low-lying levels.

2. Experimental Procedure

The spectra shown in figure 1 were taken using a three-meter grazing-incidence spectrograph [11]. The grating of 600 lines per mm and a 0.01 mm spectrograph entrance slit yielded a resolution of 0.06 Å. The source of continuum was provided by the radiation emitted by the NBS–SURF (Synchrotron Ultraviolet Radiation Facility). For this synchrotron the radiated power per unit wavelength peaks at 335 Å. Spectra were photographed from 80–600 Å with a grating blazed at 200 Å. The noble gas filled the spectrograph at pressures typically in the range of 0.01 to 0.10 torr, with absorption path lengths between entrance slit and plate of the order of 1 m. Since the synchrotron continuum is free from overlying emission and absorption lines, any features observed were due to the gas itself.

The spectra were photographed on Eastman SWR plates.[2] Wavelength calibration was obtained by super-

*Present Address: University of Reading, Physics Department, Whiteknights Park, Reading, Berks, England.

[1] Figures in brackets indicate the literature references at the end of this paper.

[2] A commercial material is identified in this paper in order to adequately specify the experimental procedure. Such identification does not imply recommendation or endorsement by the National Bureau of Standards.

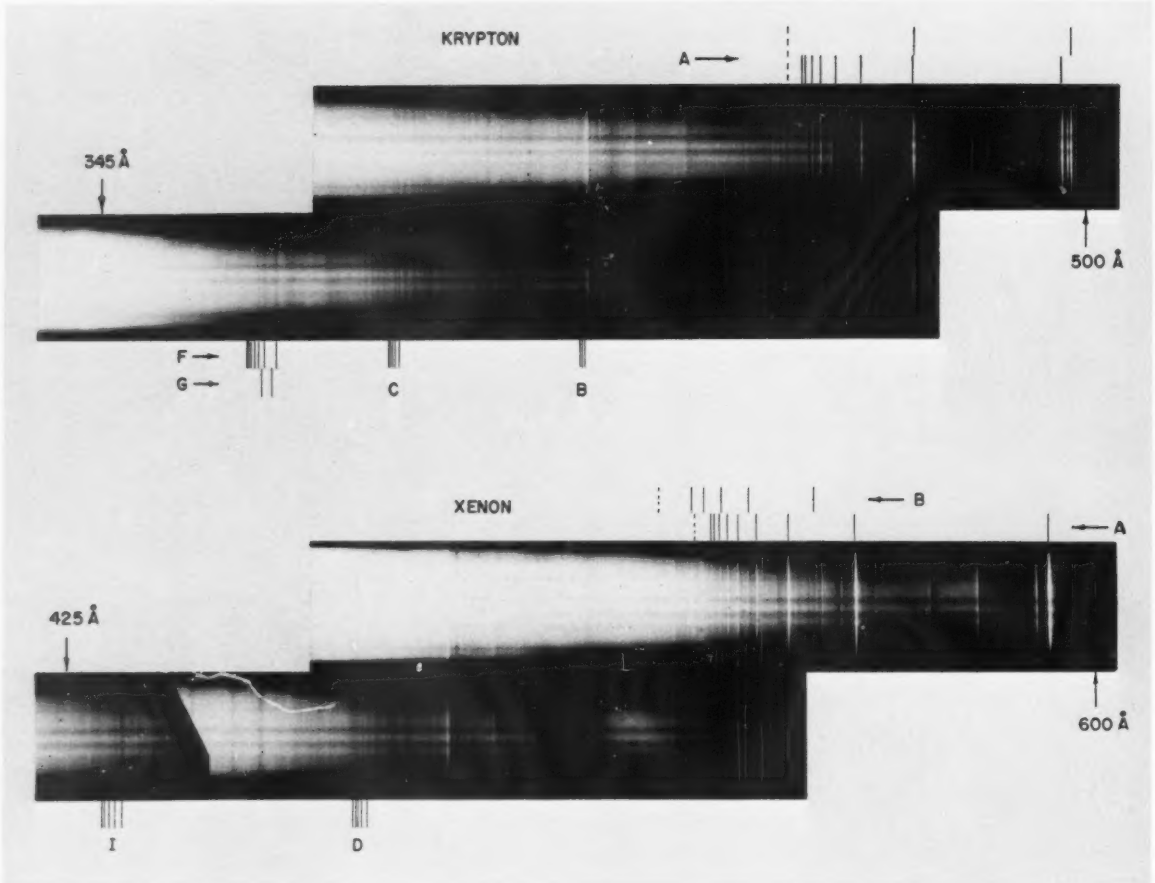

FIGURE 1. *Upper Spectrum. The absorption spectrum of* Kr *between 345 and 500 Å, taken at two different pressures to accentuate the various regions of the spectrum.*

(The background continuum cross section varies by over a factor of 3 through this region.) Black denotes absorption and therefore the prominent series of resonances due to the excitation of the subshell 4*s* electron to outer *p* orbitals are of the "window" type. The remaining resonances are due to the simultaneous excitation of two 4*p* electrons. Such resonances, grouped in series B, C, F, and G, are listed in table 3.

Lower Spectrum. The absorption spectrum of Xe *between 425 and 600 Å, taken at three different pressures.*

(The background continuum cross section varies by over a factor of 4 in this region). The prominent series of "window" resonances labeled A, are due to the excitation of a subshell 5*s* electron to outer *p* orbitals. Short series labeled C, D, and I are due to simultaneous excitation of two 5*p* electrons and are listed in table 4.

imposing the absorption spectrum of He on the Kr and Xe spectra and by using the previously determined fact that wavelengths could be reliably predicted, by application of the grating equation, to an accuracy of at least 0.01 Å. As an additional check, where long Rydberg series existed, use was made of the fact that such series converge in the limit to a well established state of Kr II or Xe II. In the cases where only small perturbations exist good quantum defects were obtained using known limits and the measured wavelengths of the Rydberg series lines.

3. Classification of Spectra

The ground state of Kr is $4s^24p^6\ ^1S_0$, that of Xe $5s^25p^6\ ^1S_0$. The ionization potentials of Kr and Xe are 14.0 and 12.1 eV respectively. Thus, when photons of an energy between 20 and 40 eV are incident upon these gases, the basic process observed is photoionization. However, as well as exciting an outer p electron to continuum ϵs and ϵd states, it is possible to excite a subshell s electron to p-type orbitals or excite two electrons simultaneously. In the latter case, either two outer p electrons or both an outer p and a subshell s electron can be excited.

Thus, in Kr for example, one may excite to configurations of the type: $4s4p^6np$ and $4s^24p^4nln'l'$ where $ll' = sp, pd, sf, df$. Transitions of the type $4s4p^5nln'l'$ where $ll' = ss, pp, sd$ etc., have not been positively identified in Kr and Xe, although unidentified resonances exist in the appropriate energy region, and the existence of similar excitations has been fairly well established in Ar [3].

The total line list of 153 resonances in Kr and 253 resonances in Xe are listed in terms of their wave-

length, wavenumber and resonance type in tables 1 and 2. By resonance type we mean the following. When a high-lying discrete state such as the $4s4p^65p$ state of Kr is excited by photoabsorption, the lifetime of this excited state is extremely short ($\sim 10^{-13}$ s). The state decays into the adjacent continuum by autoionization, with the ejection of an energetic electron, the ion being left in its ground or excited state. The interaction of a discrete state with the continuum of states of similar energy and parity has been dealt with by Fano and Cooper [12]. The resonances in the continuum which result from this interaction may be broad, and can have a variety of profiles.

TABLE 1. *Code number, wavelength (λ), wave number (ν), and profile type for all observed* Kr *resonances, listed in order of decreasing wavelength*

Number	Wavelength (Å)	Wave number (cm^{-1})	Comment[a]	Number	Wavelength (Å)	Wave number (cm^{-1})	Comment[a]
1	[b]501.23 ± .05	199509	−*sx*	52	421.56 ± .03	237214	−*sx*
2	498.83 ± .05	200469	−*dw*	53	421.23 ± .03	237400	−*sx*
3	[c]*497.50 ± .05	201005	+*dw*	54	420.90 ± .05	237586	−*sx*
4	496.90 ± .05	201248	*dw*	55	420.36 ± .05	237891	−*da*
5	*496.07 ± .05	201584	−*dw*	56	419.96 ± .05	238118	*sa*
6	492.52 ± .05	203037	−*sw*	57	419.74 ± .05	238243	*sa*
7	488.71 ± .05	204620	−*dx*	58	419.51 ± .05	238373	*sa*
8	488.06 ± .05	204893	−*dx*	59	419.10 ± .10	238607	*da*
9	472.26 ± .03	211748	+*sw*	60	418.83 ± .03	238760	*sw*
10	*471.48 ± .03	212098	+*sw*	61	418.70 ± .03	238834	*sw*
11	*471.23 ± .03	212211	−*sw*	62	418.33 ± .05	239046	*sa*
12	469.08 ± .03	213183	−*sx*	63	*417.96 ± .03	239257	*sa*
13	464.70 ± .10	215193	−*sw*	64	*417.62 ± .03	239452	*sa*
14	*462.71 ± .03	216118	+*sw*	65	*417.39 ± .05	239584	*sa*
15	461.83 ± .03	216530	−*sx*	66	*417.22 ± .05	239682	*sa*
16	460.45 ± .03	217179	*sa*	67	416.76 ± .05	239946	*sw*
17	459.91 ± .03	217434	−*sa*	68	416.01 ± .10	240379	*dw*
18	*458.69 ± .03	218012	+*sw*	69	[d]414.78 ± .10	241092	*sw*
19	457.86 ± .03	218407	−*sw*	70	413.58 ± .10	241791	*sw*
20	457.51 ± .03	218574	*sa*	71	412.79 ± .05	242254	+*sw*
21	456.67 ± .03	218976	*sa*	72	412.47 ± .05	242442	*sw*
22	*456.12 ± .03	219241	*sw*	73	409.70 ± .2	244081	*dda*
23	455.29 ± .03	219640	−*sx*	74	406.85 ± .10	245791	*da*
24	*454.73 ± .03	219911	*sw*	75	405.30 ± .10	246731	*da*
25	454.01 ± .03	220259	*sa*	76	403.34 ± .05	247930	*da*
26	*453.73 ± .03	220395	*sw*	77	401.50 ± .2	249070	*dda*
27	*453.15 ± .03	220677	*sw*	78	400.33 ± .07	249794	*da*
28	*452.68 ± .03	220907	*sw*	79	399.75 ± .07	250156	*da*
29	*452.34 ± .03	221073	*sw*	80	399.30 ± .10	250438	*da*
30	*452.07 ± .03	221205	*sw*	81	396.77 ± .10	252035	−*dw*
31	451.98 ± .03	221249	*sw*	82	394.24 ± .07	253653	*da*
32	*451.86 ± .03	221307	*sw*	83	393.50 ± .07	254130	*da*
33	*451.69 ± .03	221391	*sw*	84	392.70 ± .07	254647	*da*
34	*451.56 ± .03	221455	*sw*	85	391.83 ± .05	255213	*da*
35	*451.45 ± .03	221508	*sw*	86	*391.44 ± .05	255467	*sa*
36	450.16 ± .03	222143	−*sw*	87	*390.49 ± .05	256088	*da*
37	449.93 ± .03	222257	+*sw*	88	390.04 ± .05	256384	*sa*
38	449.22 ± .03	222608	−*sw*	89	*389.48 ± .05	256753	*da*
39	448.29 ± .03	223070	+*sw*	90	*388.84 ± .05	257175	*da*
40	446.54 ± .05	223944	−*sx*	91	*388.37 ± .05	257486	*sa*
41	444.02 ± .03	225215	+*sx*	92	*388.05 ± .05	257699	*sa*
42	439.00 ± .2	227790	*dw*	93	*387.79 ± .05	257872	*sa*
43	434.30 ± .05	230256	−*dw*	94	*387.60 ± .05	257998	*sa*
44	433.98 ± .05	230425	*sw*	95	387.45 ± .05	258098	*sa*
45	427.15 ± .03	234110	*sa*	96	***387.08 ± .05**	258345	−*da*
46	426.53 ± .05	234450	−*da*	97	386.26 ± .05	258893	−*da*
47	425.33 ± .07	235112	*da*	98	385.45 ± .07	259437	*sa*
48	424.05 ± .05	235821	*dw*	99	***385.03 ± .05**	**259720**	**−*sw***
49	423.61 ± .05	236066	*sw*	100	**384.38 ± .05**	**260159**	***sa***
50	423.17 ± .07	236312	*dw*	101	***384.03 ± .05**	**260396**	**−*sw***
51	422.58 ± .03	236642	*sa*	102	**383.47 ± .05**	260777	***sa***
				103	**383.22 ± .05**	**260947**	***sa***

TABLE 1. *Code number, wavelength (λ), wave number (ν), and profile type for all observed* Kr *resonances, listed in order of decreasing wavelength* — Continued

Number	Wavelength (Å)	Wave number (cm^{-1})	Comment[a]	Number	Wavelength (Å)	Wave number (cm^{-1})	Comment[a]
104	382.95 ± .05	261131	*sa*	129	*367.03 ± .05	272457	+ *sa*
105	[d] 382.45 ± .05	261472	*da*	130	*366.70 ± .05	272702	+ *sa*
106	382.07 ± .05	261732	*sa*	131	*366.49 ± .05	272859	+ *sa*
107	381.87 ± .05	261869	*sa*	132	365.50 ± .2	273600	*dda*
108	381.51 ± .05	262116	*sa*	133	363.80 ± .2	274880	*dda*
109	381.31 ± .05	262254	*sa*	134	362.70 ± .2	275710	*sa*
110	380.80 ± .05	262605	*sa*	135	362.30 ± .2	276010	*sa*
111	379.30 ± .2	263640	*dda*	136	361.90 ± .2	276320	*sa*
112	*378.97 ± .05	263873	*sa*	137	359.60 ± .2	278090	*sa*
113	*378.65 ± .05	264096	*sa*	138	358.20 ± .2	279170	*sa*
114	*378.43 ± .05	264250	*sa*	139	357.30 ± .2	279880	*sa*
115	*378.23 ± .05	264389	*sa*	140	356.50 ± .2	280500	*sa*
116	375.03 ± .2	265390	*dda*	141	[d] 355.60 ± .2	281210	*da*
117	5.03 ± .05	266645	*sa*	142	354.80 ± .2	281850	*da*
118	374.66 ± .05	266909	*sa*	143	354.40 ± .2	282170	*da*
119	374.20 ± .05	267237	*sa*	144	350.30 ± .2	285470	*da*
120	373.00 ± .2	268100	*dda*	145	349.30 ± .2	286290	*da*
121	371.86 ± .05	268918	*sa*	146	348.30 ± .2	287110	*da*
122	371.37 ± .05	269273	*sa*	147	347.00 ± .2	288180	*da*
123	*370.87 ± .05	269636	*sa*	148	345.10 ± .2	289770	*dda*
124	*370.13 ± .05	270175	*sw*	149	343.50 ± .2	291120	*da*
125	*369.13 ± .05	270907	*sa*	150	342.30 ± .2	292140	*sa*
126	*368.60 ± .05	271297	*sw*	151	341.80 ± .2	292570	*sa*
127	*368.14 ± .05	271636	*sa*	152	341.10 ± .2	293170	*sa*
128	*367.56 ± .05	272064	+ *sa*	153	337.40 ± .3	296380	*da*

[a] Sign plus (+) or minus (−) represents the sign of q in the Fano [12] representation of noninteracting resonances. The letters s, d, dd, give a very rough idea of the sharpness or diffuseness of lines on a photographic plate. Naturally, this apparent width varies with gas pressure. The letters *x*, *w* or *a* indicate specifically if the resonance has been measured at (*x*) the point of highest rate of change of plate density, (*w*) the point of maximum plate density, or (*a*) the point of minimum plate density (maximum absorption); e.g., sw means a sharp resonance of low unknown (q) measured at the peak transmission point.

[b] Errors shown represent the estimated absolute uncertainty. In the case of Kr the relative accuracies are of the order of 0.02 Å better than the estimated absolute uncertainty.

[c] Resonances denoted by an asterisk (*) are listed in table 3 as possible members of Rydberg series.

[d] Possible double resonance.

TABLE 2. *Code number, wavelength (λ), wave number (ν), and profile type for all observed* Xe *resonances, listed in order of decreasing wavelength*

Number	Wavelength (Å)	Wave number (cm^{-1})	Comment[a]	Number	Wavelength (Å)	Wave number (cm^{-1})	Comment[a]
1	[b] 599.99 ± .05	166669	*sw*	17	556.51 ± .02	179691	+ *sx*
2	595.93 ± .03	167805	− *sw*	18	555.52 ± .02	180012	− *sw*
3	[c]* 591.77 ± .03	168985	+ *dw*	19	555.28 ± .02	180089	*sw*
4	589.54 ± .02	169624	− *sw*	20	552.31 ± .02	181058	+ *sx*
5	586.29 ± .02	170564	− *sw*	21	552.00 ± .02	181159	*sw*
6	582.74 ± .02	171603	− *sx*	22	* 550.76 ± .02	181567	+ *sx*
7	581.11 ± .02	172084	*sw*	23	549.60 ± .02	181951	*sa*
8	579.98 ± .02	172420	*sw*	24	549.19 ± .05	182086	*sa*
9	579.16 ± .02	172664	− *sw*	25	548.14 ± .02	182435	*sa*
10	570.79 ± .02	175196	*sw*	26	547.79 ± .02	182552	*sa*
11	570.47 ± .05	175294	*sw*	27	546.88 ± .02	182855	*sa*
12	562.39 ± .02	177813	*sa*	28	* 546.08 ± .02	183123	+ *sw*
13	560.64 ± .05	178368	− *sa*	29	545.26 ± .02	183399	*sw*
14	560.44 ± .05	178431	+ *sa*	30	544.95 ± .05	183503	*sa*
15	558.78 ± .02	178961	− *sx*	31	* 544.18 ± .02	183763	− *sx*
16	* 557.83 ± .02	179266	+ *sw*	32	543.89 ± .02	183861	+ *sw*

TABLE 2. *Code number, wavelength (λ), wave number (ν), and profile type for all observed* Xe *resonances listed in order of decreasing wavelength*—Continued

Number	Wavelength(Å)	Wave number (cm^{-1})	Comment[a]	Number	Wavelength(Å)	Wave number (cm^{-1})	Comment[a]
33	543.49 ± .05	183996	*sw*	95	499.74 ± .03	200104	−*sw*
34	541.95 ± .02	184519	*sa*	96	498.54 ± .03	200586	*sa*
35	[d] 541.46 ± .05	184686	*sa*	97	497.33 ± .05	201074	*sw*
36	540.62 ± .02	184973	*sw*	98	497.06 ± .05	201183	+*sx*
37	* 540.54 ± .02	185000	*sw*	99	496.11 ± .05	201568	*da*
38	* 539.33 ± .02	185415	−*sx*	100	495.69 ± .10	201739	*sa*
39	537.75 ± .02	185960	*sa*	101	495.42 ± .05	201849	*sw*
40	* 537.46 ± .02	186060	*sw*	102	495.15 ± .05	201959	*sw*
41	537.38 ± .02	186088	*sw*	103	495.02 ± .05	202012	*sa*
42	537.22 ± .02	186143	*sw*	104	494.39 ± .05	202269	−*sw*
43	536.83 ± .02	186279	−*sw*	105	493.80 ± .05	202511	−*sa*
44	535.95 ± .02	186585	−*sa*	106	493.42 ± .05	202667	−*sa*
45	* 535.55 ± .02	186724	*sw*	107	492.91 ± .03	202877	*sa*
46	535.13 ± .02	186870	−*sx*	108	492.10 ± .2	203210	*dda*
47	* 534.58 ± .02	187063	−*sx*	109	491.22 ± .03	203575	−*sw*
48	* 534.27 ± .02	187171	*sw*	110	490.20 ± .05	203998	−*sx*
49	[d]* 533.34 ± .05	187498	*sw*	111	489.93 ± .05	204111	*sa*
50	533.00 ± .02	187617	−*sw*	112	489.66 ± .03	204223	*sa*
51	* 532.76 ± .02	187702	*sw*	113	489.19 ± .03	204420	*da*
52	532.06 ± .02	187949	−*sw*	114	488.91 ± .03	204537	*sa*
53	531.83 ± .02	188030	−*sw*	115	488.59 ± .03	204671	+*sa*
54	* 531.37 ± .02	188193	−*sw*	116	488.23 ± .03	204821	+*sa*
55	* 531.21 ± .02	188249	*sw*	117	487.93 ± .03	204947	*sa*
56	531.04 ± .02	188310	*sw*	118	487.79 ± .03	205006	*sw*
57	* 530.93 ± .02	188349	*sw*	119	487.68 ± .03	205052	*sw*
58	* 530.83 ± .03	188384	*sw*	120	487.03 ± .05	205326	*sw*
59	* 530.74 ± .03	188416	*sw*	121	486.71 ± .05	205461	*sw*
60	530.10 ± .02	188644	−*sw*	122	485.55 ± .03	205952	+*sw*
61	529.94 ± .03	188701	*sw*	123	485.25 ± .05	206079	−*sw*
62	* 529.34 ± .02	188914	*sw*	124	483.12 ± .05	206988	+*sa*
63	528.93 ± .03	189061	*sa*	125	482.20 ± .05	207383	*sa*
64	* 528.42 ± .03	189243	+*sa*	126	481.28 ± .05	207779	*sw*
65	* 528.05 ± .05	189376	+*sw*	127	480.47 ± .05	208130	−*sa*
66	526.35 ± .02	189988	−*sw*	128	478.93 ± .10	208799	*da*
67	526.15 ± .02	190060	*sw*	129	478.30 ± .05	209074	*da*
68	525.86 ± .02	190165	*sw*	130	477.51 ± .05	209420	*da*
69	* 525.77 ± .02	190197	*sw*	131	477.12 ± .05	209591	*sw*
70	525.27 ± .03	190378	−*sw*	132	476.77 ± .05	209745	*sw*
71	521.97 ± .05	191582	*sw*	133	476.00 ± .3	210080	*dda*
72	521.81 ± .05	191641	*sw*	134	475.19 ± .05	210442	*sw*
73	521.54 ± .10	191740	*da*	135	*474.36 ± .05	210810	*da*
74	518.88 ± .10	192723	*sa*	136	*473.42 ± .05	211229	*da*
75	517.24 ± .10	193334	*da*	137	*472.83 ± .05	211492	*sa*
76	514.42 ± .10	194394	*da*	138	*472.36 ± .05	211703	*sa*
77	513.86 ± .10	194606	*da*	139	*472.01 ± .05	211860	*sa*
78	513.27 ± .10	194829	*da*	140	*471.67 ± .05	212013	*sa*
79	512.32 ± .05	195191	*sa*	141	*470.46 ± .05	212558	*sa*
80	510.46 ± .05	195902	*sa*	142	*469.40 ± .05	2130[illegible]	*sa*
81	509.54 ± .03	196255	*sa*	143	*468.67 ± .05	213370	*sa*
82	509.27 ± .03	196359	*sa*	144	*468.15 ± .05	213607	*sa*
83	[d] 507.85 ± .10	196909	*dw*	145	467.72 ± .05	213803	*sa*
84	506.69 ± .05	197359	*sw*	146	467.54 ± .05	213885	*sa*
85	506.36 ± .05	197488	+*sw*	147	467.02 ± .05	214124	*da*
86	505.89 ± .10	197671	*sa*	148	466.30 ± .2	214450	*da*
87	505.42 ± .03	197855	−*sx*	149	465.80 ± .05	214684	*sa*
88	504.40 ± .05	198255	−*sx*	150	465.10 ± .05	215008	*da*
89	503.64 ± .05	198555	−*sx*	151	464.35 ± .05	215355	*sa*
90	502.87 ± .05	198859	−*sx*	152	463.27 ± .07	215857	*sa*
91	502.13 ± .03	199152	−*sw*	153	462.63 ± .07	216155	*sa*
92	501.74 ± .05	199306	*sw*	154	462.23 ± .07	216343	*sa*
93	501.39 ± .05	199446	*sw*	155	*461.00 ± .05	216920	+*sa*
94	500.37 ± .05	199852	−*sw*	156	460.31 ± .10	217245	*dda*

TABLE 2. *Code number, wavelength* (λ), *wave number* (*ν*), *and profile type for all observed* Xe *resonances, listed in order of decreasing wavelength* — Continued

Number	Wavelength(Å)	Wave number (cm^{-1})	Comment[a]	Number	Wavelength(Å)	Wave number (cm^{-1})	Comment[a]
157	*459.68 ± .05	217543	*sa*	206	*432.31 ± .05	231315	*da*
158	459.23 ± .05	217756	*da*	207	431.87 ± .05	231551	*sa*
159	*458.63 ± .05	218041	*sa*	208	*431.55 ± .05	231723	*sa*
160	*458.04 ± .05	218322	*sa*	209	*431.26 ± .05	231879	*sa*
161	456.80 ± .2	218910	*da*	210	*430.90 ± .05	232072	*sa*
162	456.71 ± .07	218957	−*sa*	211	*430.63 ± .05	232218	*sa*
163	456.42 ± .05	219096	−*sa*	212	*430.45 ± .05	232315	*sa*
164	455.83 ± .05	219380	*sa*	213	*430.31 ± .05	232391	*sa*
165	455.40 ± .05	219587	*sa*	214	429.67 ± .05	232737	+*sa*
166	454.95 ± .05	219804	−*sa*	215	428.36 ± .05	233448	*sa*
167	*454.34 ± .05	220099	−*sa*	216	428.14 ± .05	233568	*sa*
168	454.00 ± .05	220264	*sa*	217	427.92 ± .05	233689	*sa*
169	453.70 ± .05	220410	*sa*	218	426.61 ± .05	234406	+*sa*
170	*453.42 ± .05	220546	−*sa*	219	425.88 ± .05	234808	*da*
171	453.11 ± .07	220697	*sa*	220	425.51 ± .05	235012	*da*
172	452.70 ± .07	220897	−*sx*	221	424.97 ± .05	235311	*sa*
173	*452.35 ± .10	221068	*dda*	222	424.47 ± .10	235588	*da*
174	452.06 ± .07	221210	*sa*	223	424.02 ± .10	235838	*da*
175	450.33 ± .05	222059	−*da*	224	423.43 ± .10	236167	*da*
176	449.67 ± .05	222385	*da*	225	422.73 ± .10	236558	*da*
177	449.15 ± .05	222643	*da*	226	420.40 ± .2	237870	*dda*
178	448.42 ± .05	223005	*da*	227	418.00 ± .2	239230	*dda*
179	448.01 ± .05	223209	*sa*	228	413.70 ± .10	241721	*da*
180	447.61 ± .05	223409	*da*	229	410.30 ± .10	243724	*da*
181	445.91 ± .05	224260	*sa*	230	408.94 ± .10	244535	*sa*
182	*445.61 ± .05	224411	*da*	231	408.50 ± .10	244798	*sa*
183	445.41 ± .05	224512	*da*	232	407.67 ± .10	245296	*sa*
184	444.93 ± .05	224754	*sa*	233	406.32 ± .10	246111	*sa*
185	444.38 ± .05	225033	*sa*	234	406.07 ± .10	246263	*sa*
186	*443.73 ± .07	225362	*da*	235	404.96 ± .10	246938	*sa*
187	443.27 ± .05	225596	*da*	236	404.63 ± .10	247139	*sa*
188	442.91 ± .05	225779	*da*	237	403.87 ± .10	247604	*sa*
189	*442.41 ± .07	226035	*da*	238	401.90 ± .2	248820	*da*
190	*441.46 ± .10	226521	*sa*	239	401.24 ± .10	249227	*sa*
191	*441.01 ± .07	226752	*sa*	240	400.90 ± .10	249439	*sa*
192	*440.59 ± .07	226968	*sa*	241	399.94 ± .10	250038	*da*
193	*440.33 ± .07	227102	*sa*	242	399.56 ± .10	250275	*da*
194	439.92 ± .07	227314	*da*	243	399.00 ± .2	250630	*da*
195	439.30 ± .07	227635	*da*	244	397.72 ± .15	251433	*da*
196	438.29 ± .07	228159	*sa*	245	396.70 ± .2	252080	*da*
197	437.64 ± .07	228498	*sa*	246	395.66 ± .15	252742	*da*
198	437.22 ± .05	228718	*sa*	247	392.28 ± .15	254920	*dda*
199	436.82 ± .05	228927	*sa*	248	387.39 ± .15	258138	*da*
200	436.60 ± .05	229043	*sa*	249	385.62 ± .15	259323	*da*
201	436.15 ± .05	229279	+*da*	250	384.56 ± .15	260037	*da*
202	435.75 ± .05	229489	*da*	251	383.33 ± .15	260872	*da*
203	435.16 ± .05	229801	*sa*	252	377.20 ± .15	265111	*da*
204	*434.34 ± .05	230234	*da*	253	375.34 ± .15	266425	*da*
205	*433.30 ± .05	230787	*da*				

[a] Sign plus (+) or minus (−) represents the sign of q in the Fano [12] representation of noninteracting resonances. The letters *s*, *d*, *dd*, give a very rough idea of the sharpness or diffuseness of lines on a photographic plate. Naturally, this apparent width varies with gas pressure. The letters *x*, *w*, or *a* indicate specifically if the resonance has been measured at (*x*) the point of highest rate of change of plate density, (*w*) the point of maximum plate density, or(*a*) the point of minimum plate density (maximum absorption); e.g., *sw*, means a sharp resonance of low unknown(q) measured at the peak transmission point.

[b] Errors shown represent the estimated absolute uncertainty. In the case of Xe the relative accuracies are of the order of 0.02 Å better than the estimated absolute uncertainty.

[c] Resonances denoted by an asterisk (*) are listed in table 4 as possible members of Rydberg series.

[d] Possible double resonance.

The absorption cross section in the region of a resonance can be parameterized in the form:

$$\sigma(E)=\sigma_a\frac{(q+\epsilon)^2}{1+\epsilon^2}+\sigma_b$$

with $\epsilon=(E-E_r)/\frac{1}{2}\Gamma$, where the quantities E and E_r are the photon energy and the resonance energy ($\epsilon=0$), respectively. The parameter q is the resonance profile index and is defined in terms of transition matrix elements between the ground state, the modified discrete state and the continuum states. The half-width of the resonance is Γ, the quantity σ_a is the cross section associated with the fraction of the available continua with which the discrete state interacts, and σ_b is the cross section associated with the fraction of the continua which does not enter into the interaction. The parameter ρ, called the correlation index [12], is obtained from the relation $\rho^2=\dfrac{\sigma_a}{\sigma_a+\sigma_b}$.

Experimentally, when q is positive, a region of low absorption at low energy immediately precedes a region of increased absorption at higher energy. For a negative q, the reverse is true. If q is of the order of 1, the resonance appears quite asymmetric. If q is large and ρ^2 is small, the resonance looks like a conventional Lorentz absorption profile (absorption-type resonance), but if q is close to zero, the resonance has only a reduced-absorption zone (window-type resonance). When possible, in tables 1 and 2 the sign q is given. Where the letter x, a, and w are used, the resonance appears to be an asymmetric, absorption or window-type resonance, respectively, and has been measured as such.

3.1. One-Electron Transitions

The most prominent series should be those associated with one-electron transitions. This was found to be the case in Ne and Ar, and is equally true in Kr and Xe. The ground state of the noble gases is a $^1S_0$. In a photoexcitation process, therefore, the upper state involved must have $J=1$, regardless of the coupling conditions.

Since strict L–S coupling is not applicable, the strongest Rydberg series would be due to transitions:

$$\text{Kr: } 4s^24p^6\,{}^1S_0\rightarrow 4s4p^6(^2S_{1/2})np;\ n=5,6\ \ldots\ \text{(two } J=1 \text{ components)}$$

$$\text{Xe: } 5s^25p^6\,{}^1S_0\rightarrow 5s5p^6(^2S_{1/2})np;\ n=6,7\ \ldots\ \text{(two } J=1 \text{ components)}$$

The upper configurations have *only* two $J=1$ states, and transitions to upper states of other J cannot occur due to the rigorous selection rules: $\Delta J=0,\ \pm1$; $0\not\rightarrow 0$.

Thus we might expect to resolve at low n values, the two $J=1$ members converging to the known $^2S_{1/2}$ limits of Kr II or Xe II. (This limit occurs in Kr at 450.62 Å and in Xe at 529.91 Å).

In the case of Kr, we see three "strong" window resonances in the region where the first members of the one-electron excitation series should occur. In Xe, one "strong" resonance and three somewhat weaker resonances are observed. "Strong" in this case means high visibility rather than a large oscillator strength, since the visibility of resonances depends also on the interference effects. Additionally, the ability to see window resonances is photographically enhanced at lower pressures.

The choice of the two $J=1$ components of the first member of the Rydberg series is by no means unambiguous. The two components chosen in Kr are seen in the top photograph of figure 1 and again in the densitometer trace, figure 2. The resonances are denoted by their code numbers 3 and 5, see table 1. The wavelengths, principal quantum numbers (n) and effective quantum numbers (n^*) are given in table 3, part A. Recent work appears to support the above choice. Reader et al. [13] noted that the effective quantum number of the 5p electron in the $4s4p^65p$ state in the isoelectronic sequence Zr V, Nb VI, and Mo VII consistently differed from the n^* in the $4s^24p^65p$ state of Nb V, Mo VI, and Tc VII by 0.040. Extrapolating this relationship the n^* for the $4s4p^65p$ state of Kr I can be obtained from the n^* for the $4s^24p^65p$ state of Rb I (2.289). The result, 2.329, is in good agreement with the value of 2.323 for the assigned resonance to this state in table 3.

In Xe, the most prominent member of the quartet of resonances (Code Nos. 1, 2, 3, 4) has been chosen as the first member of the one-electron excitation series: 3, 16, 28 etc. This series can be seen in the lower photograph of figure 1 and also in the densitometer trace figure 3. The wavelengths and effective quantum numbers are given in table 4, part A. A choice has not been made for the second $J=1$ component in Xe, although it is likely to be resonance 1 or 2.

Recent work [13] suggests that the main $J=1$ component in Xe should have an effective quantum number $n^*=2.391$. If resoance 4 is taken as the first member of the series, its effective quantum number is 2.398. Resonance 3 chosen here gives $n^*=2.359$. This choice was made upon the basis of the great similarity in resonance profiles of line 3 and the following members of the series, resonances 16 and 28. Figure 3 clearly shows that line 3 is asymmetric, with a low positive q, whereas resonance 4 has a q of the *opposite* sign. In fact, Ederer [10] has shown that the values of q and ρ^2 for resonance 3 are 0.23(±.04) and 0.65(±.03), for resonance 4 are −0.14(±.04) and 0.50(±.04) and for resonance 16 are 0.16(±.04) and 0.67(±.02). In addition, we can compare the equivalent one-electron excitation states in Ne, Ar, Kr, and Xe and the way in which the first member of the Rydberg series is always depressed (moved to longer wavelengths) relative to a simple theoretical estimate of its location, due to screening effects. The increase in this screening effect from Ne through Kr leads us to expect the strongest $J=1$ component in Xe to lie almost exactly where it is. Nevertheless, it is conceivable that configuration interaction may cause resonances to interchange intensi-

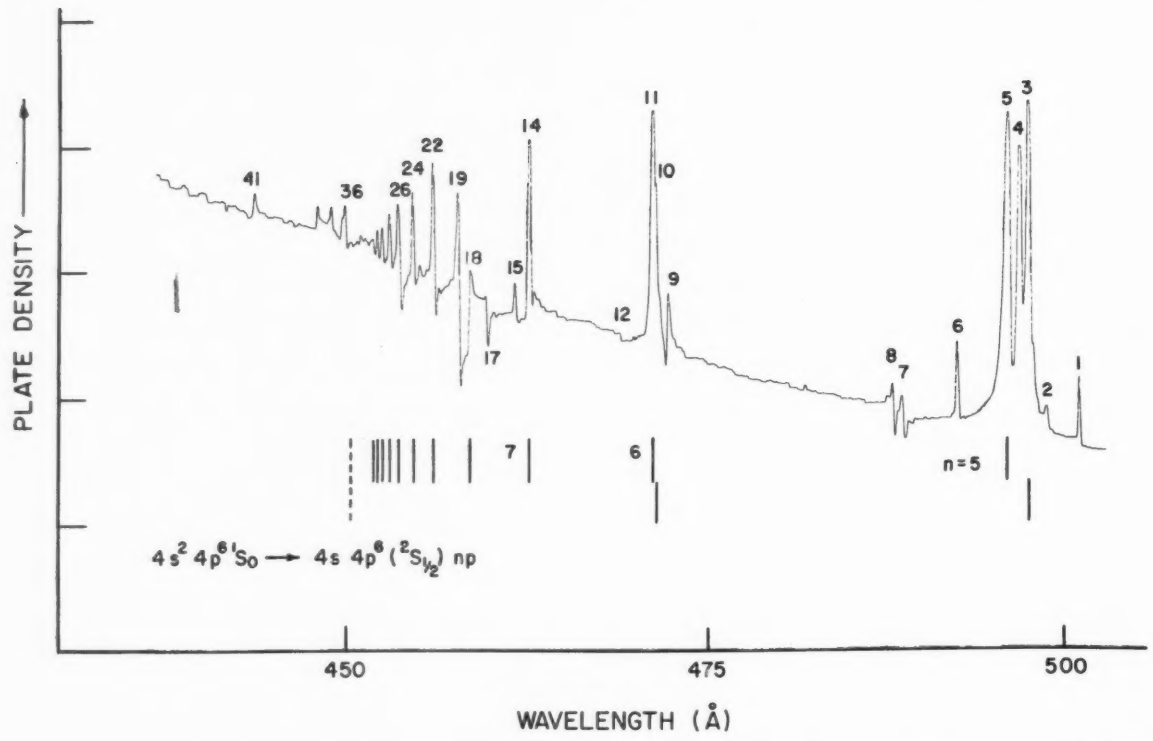

FIGURE 2. *A microdensitometer trace of the absorption spectrum of* Kr *in the region 435–500* Å.

The main series of "window" resonances are indicated by vertical lines. Note the two $J=1$ components for the $n=5$ and 6 members. The code numbers alongside the resonances allow determination of their wavelengths (and in some cases classification) via tables 1 and 3.

TABLE 3. *Resonances in* Kr I *grouped as members of possible series converging to the limits indicated*

The principal quantum number (n), and effective quantum number (n^*) associated with the appropriate series limits are given. The levels in Kr II to which these series converge are arranged in order of increasing energy. Their positions are obtained from data [18] on the Kr II, added to 112915 cm^{-1}, the first ionization energy of Kr I.

Code number	λ (Å)	n	n^*
(A) Limit: $-4s4p^6(^2S_{1/2}) = 221915$ cm^{-1}; Series: $-4s4p^6np$			
5	496.07	5	2.323
11	471.23	6	3.363
14	462.71	7	4.351
18	458.69	8	5.303
22	456.12	9	6.406
24	454.73	10	7.399
26	453.73	11	8.498
27	453.15	12	9.42
28	452.68	13	10.43
29	452.34	14	11.41
30	452.07	15	12.43
32	451.86	16	13.44
33	451.69	17	14.47
34	451.56	18	15.44
35	451.45	19	16.43
Second series of two available, having $J=1$ final state			
3	497.50	5	2.304
10	471.48	6	3.343

Code number	λ (Å)	n	n^*
(B) Unknown limit[a] = 240300 cm^{-1}			
63	417.96	13	10.26 [a] (9.35)
64	417.62	14	11.38 (10.18)
65	417.39	15	12.38 (10.88)
66	417.22	16	13.32 (11.49)
(C): $-4p^4(^1S)5s(^2S_{1/2}) = 258727$ cm^{-1}; Series: $-4p^45snp$			
86	391.44	8	5.59
87	390.49	9	6.45
89	389.48	10	7.46
90	388.84	11	8.41
91	388.37	12	9.41
92	388.05	13	10.33
93	387.79	14	11.33
94	387.60	15	12.27
96	387.08	16	13.21
(D) Limit: $-4p^4(^1D)4d(^2D_{5/2}) = 262429$ cm^{-1}; Series: $-4p^44dnp$			
99	385.03	9	6.37
101	384.03	10	7.35

TABLE 3. *Resonances in* Kr I *grouped as members of possible series converging to the limits indicated* – Continued

The principal quantum number (n), and effective quantum number (n^*) associated with the appropriate series limits are given. The levels in Kr II to which these series converge are arranged in order of increasing energy. Their positions are obtained from data [18] on the Kr II, added to 112915 cm^{-1}, the first ionization energy of Kr I.

Code number	λ (Å)	n	n^*	Code number	λ(Å)	n	n^*
(E) Limit: $-4p^4(^1D)4d(^2P_{1/2}) = 265100\ cm^{-1}$; Series: $-4p^44dnp$							
112	378.97	12	9.46	127	368.14	10	7.27
113	378.65	13	16.46	128	367.56	11	8.17
114	378.43	14	11.36	129	367.03	12	9.36
115	378.23	15	12.43	130	366.70	13	10.44
				131	366.49	14	11.35
(F) Limit[b]: $-4p^4(^1D)4d(^2S_{1/2}) = 273710\ cm^{-1}$; Series: $-4p^44dnp$				(G) Limit: $-4p^4(^1S)4d(^2D_{5/2}) = 273927\ cm^{-1}$; Series: $-4p^44dnp$			
123	370.87	8	5.19	124	370.13	8	5.41
125	369.13	9	6.26	126	368.60	9	6.46

[a] The nearest known limit [18] is $(^1D)5s(^2D_{3/2})$ at 240512 cm^{-1}. One could assume this limit to be the appropriate one, giving the values of n^* shown in parentheses. Noninteger difference in n^* through the series could possibly be explained by configuration interaction effects.
[b] This limit was previously assigned [19] to $4p^4(^3P)5d(^4P_{1/2})$. It was recently reassigned [18] by Minnhagen.

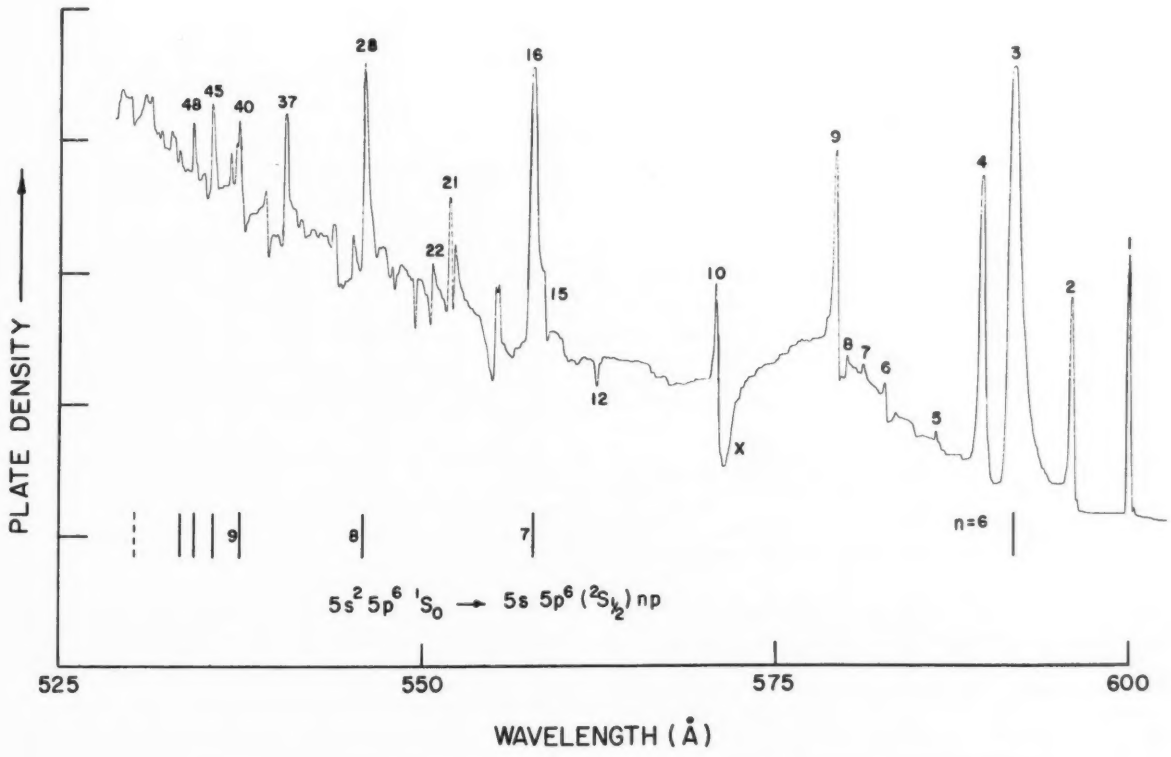

FIGURE 3. *A microdensitometer trace of the absorption spectrum of* Xe *in the region 525–600* Å.

The main series of "window" resonances is denoted by vertical lines. The code numbers allow determination of wavelengths (and in some cases classification) via tables 2 and 4. The absorption feature labeled X, is the third order of an absorption line [4] at 190.41 Å.

TABLE 4. *Resonances in* Xe I *grouped as members of possible series converging to the limits indicated*

The principal quantum number (n) and effective quantum number (n^*) associated with the appropriate series limits are given. The levels in Xe II to which these series converge are obtained by adding 97834 cm^{-1}, the lowest ionization energy of Xe I, to terms [19] of Xe II.

Code number	λ (Å)	n	n^*
(A) Limit: $-5s5p^6(^2S_{1/2})$ = 188708 cm^{-1}; Series: $-5s5p^6np$			
3	591.77	6	2.359
16	557.83	7	3.409
28	546.08	8	4.433
[a] 37	540.54	9	5.440
40	537.46	10	6.438
45	535.55	11	7.437
48	534.27	12	8.450
[b] 49	533.34	13	9.52
51	532.76	14	10.44
55	531.21	19	15.47
57	530.93	21	17.48
58	530.83	22	18.41
59	530.74	23	19.39
(B) Limit: $-5p^4(^3P)6s(^4P_{5/2})$ = 190902 cm^{-1}; Series: $-5p^46snp$			
22	550.76	7	3.429
38	539.33	8	4.472
47	534.58	9	5.346
54	531.37	10	6.364
62	529.34	11	7.431
65	528.05	12	8.480
(C) Limit: $-5p^4(^3P)6s(^4P_{3/2})$ = 192898 cm^{-1}; Series: $-5p^46snp$			
31	544.18	7	3.466
[b] 49	533.34	8	4.508
64	528.42	9	5.480
69	525.77	10	6.374
(D) Unknown Limit [c] = 212665 cm^{-1}			
135	474.36	8	7.691
136	473.42	9	8.742
137	472.83	10	9.68
138	472.36	11	10.68
139	472.01	12	11.68
140	471.67	13	12.97
(E) *Limit:* $-5p^4(^3P)6p(^4D_{3/2})$ = 214617 cm^{-1}; Series: $-5p^46pnd$ [d]			
141	470.46	10	7.30
142	469.40	11	8.34
143	468.67	12	9.38
144	468.15	13	10.42
(F) Limit: $-5p^4(^3P)6p(^4S_{3/2})$ = 219463 cm^{-1}; Series: $-5p^46pnd$			
155	461.00	9	6.57
157	459.68	10	7.56
159	458.63	11	8.78
160	458.04	12	9.80
(G) Limit: $-5p^4(^1S)5d(^2D_{3/2})$ = 222136 cm^{-1}; Series: $-5p^45dnp$			
167	454.34	11	7.34
170	453.42	12	8.31
173	452.35	13	9.41
(H) Limit: $-5p^4(^1D)6p(^2F_{7/2})$ = 227898 cm^{-1}; Series: $-5p^46pnd$			
182	445.61	8	5.61
186	443.73	9	6.58
189	442.41	10	7.67
190	441.46	11	8.93
191	441.01	12	9.79
192	440.59	13	10.87
193	440.33	14	11.74
(I) Limit: $-5p^4(^3P)7s(^4P_{1/2})$ = 232895 cm^{-1}; Series: $-5p^47snp$			
204	434.34	10	6.42
205	433.30	11	7.22
206	432.31	12	8.34
208	431.55	13	9.68
209	431.26	14	10.39
210	430.90	15	11.55
211	430.63	16	12.73
212	430.45	17	13.76
213	430.31	18	14.75

[a] The resonance at 540.62 Å is an alternative choice for the $n=9$ member.

[b] This resonance appears to be double and is used in series (A) and (C).

[c] The nearest Xe II levels are $5p^4(^1D)5d(^2F_{5/2,\,7/2})$ at 212585 cm^{-1} and 212748 cm^{-1}, either of which would allow an nf series.

[d] The quantum defects for this series are more appropriate to a running p electron. However, assuming a correct assignment for the level in Xe II, parity considerations require a running d electron (or an s electron).

ties, and affect their shapes. Good theoretical calculations will be required to resolve this situation.

If we move to higher series members in Kr, we find that resonance 18 has an unusually low effective quantum number and a low intensity (see fig. 2). On the basis of the quantum defect alone, resonance 18, the $n=8$ member of this series, was chosen as a member of the Rydberg series. Clearly, resonance 19 is much "stronger" (see also Ederer [10]) and was observed by Samson [15] and classified as a member of the series with $n^*=5.593$. Once again, there is ambiguity. The remainder of the series is quite definitely established on a basis of quantum defects, intensities and profiles.

In tracing the development of the Xe series, we find the $n=9$ member to be double and an arbitrary choice must be made from resonances 36 and 37. Other workers [14, 15] did not resolve these resonances. Configuration interactions cause members $n=15$ through 18 and $n=20$ to be missing.

TABLE 5. *A comparison of the wavelengths of some of the resonances measured in the present work and those of other workers*

The Siegbahn [16] wavelengths are obtained using the conversion factor $\lambda = 12398/E(eV)$.

Krypton				Xenon				
Code	Present work	Samson [15]	Siegbahn [16]	Code	Present work	Samson [15]	Mansfield [17]	Siegbahn [16]
1	501.23	501.14		1	599.99	599.95	599.81	
3	497.50	497.44	497.1	2	595.93	595.92	595.83	
4	496.90	496.85		3	591.77	591.81	591.67	592.1
5	496.07	496.00	495.7	4	589.54	589.62	589.50	589.5
10	471.48	471.55	471.2	5	586.29		586.24	
14	462.71	462.69	462.8	6	582.74		582.72	
18	458.69		458.8	7	581.11		581.07	
19	[a] 457.86	457.85		8	579.98		579.94	
22	456.12	456.10	456.0	9	579.16	[14] 579.25	579.15	
24	454.73	454.71	455.0	10	570.79	[14] 570.90	570.80	
26	453.73	453.71	453.8	15	558.78		558.78	
27	453.14	453.14		16	557.83	557.92	557.86	557.7
29	452.32	452.32		19	555.28		555.32	
30	452.07	452.01		21	552.00	[14] 552.07	552.02	
32	451.86	451.85		22	550.76		550.77	
				28	546.08	546.16		546.2
				[b] 36	540.62	540.71		540.5
				37	540.54			
				40	537.46	537.40		
				45	535.55	535.62		

[a] Resonance 18 was chosen in the present work, on the basis of quantum defect; for $4s4p^68p$. However, resonance 19 is a considerably stronger line seen also by Samson and assigned to the $8p$ state.

[b] Two resonances, equally strong, just resolved.

Finally, in table 5, we see a comparison of the long wavelength resonances in Kr and Xe with other workers. In Kr, the present data is compared with the photoabsorption work of Samson [14, 15] and the electron spectroscopic observations of Siegbahn and co-workers [16]. In Xe, comparison is also made with the photoabsorption work of Mansfield [17] (Mansfield measured Kr also, and was in agreement with the present work for the stronger transitions). The error limits quoted by Samson are ± 0.05 Å, those of Siegbahn et al. are of the order of 0.2 Å. Mansfield gave no estimated error, but he had some calibration problems in the region of 585–600 Å due to lack of standards. The accuracy of the present measurements is also impaired in this region of the spectrum because of slight instrumental errors and this is reflected in the somewhat increased error limits given to the resonances in that region. Almost all of the wavelengths of Samson agree, within the combined error limits, with the present data, even in the range 585–600 Å.

The data of Siegbahn et al. was obtained by firing electrons of an energy of several keV into the noble gases, and measuring the energies (typically 8 to 14 eV) of the electrons released in the subsequent autoionization process, with a spherical electrostatic analyzer. Rydberg series of electron lines were found corresponding to transitions from excited states of neutral atoms to the ground state of the ions. By measuring the kinetic energy of electrons produced in the autoionization process:

$$4s4p^6np \rightarrow 4s^24p^5(^2P_{1/2,\,3/2}) + e$$

and knowing the energy of the $4s^24p^5(^2P_{1/2,\,3/2})$ states of Kr II, they were able to calculate the energy of the excited state before autoionization. Since the Siegbahn data was normalized to the present data at certain wavelengths, it cannot be thought of as independent. It is interesting, however, to note that these workers picked out a second $J=1$ component for the $4s4p^65p$ state of Kr. Even though the absolute wavelengths of resonances 3 and 5 disagree by 0.3 Å, the difference in wavelengths of 1.4 Å is in agreement with the present data. In Xe, however, the implication might be that resonances 3 and 4 are the two $J=1$ components, in agreement with another recent estimate [13], and in disagreement with the present classification. It should be pointed out, however, that excitation by electron bombardment can excite, in general, many transitions not allowed optically and that often such nonoptically allowed transitions are preferred. In addition, the resonance profiles may be completely different.

3.2. Two-Electron Transitions

It has been pointed out that only two $J=1$ components can be expected for states such as $4s4p^65p$ in Kr.

The remaining resonances in Kr, such as 1, 2, 4, 6, 7, 8 etc. (see fig. 2) must therefore be classified, from energy considerations, in terms of *two*-electron transitions, viz:

$$\text{Kr: } 4s^2 4p^6\ {}^1S_0 \rightarrow 4s^2 4p^4 ({}^3P, {}^1D, {}^1S)\ nln'l' \text{ and in}$$

$$\text{Xe: } 5s^2 5p^6\ {}^1S_0 \rightarrow 5s^2 5p^4\ ({}^3P, {}^1D, {}^1S)\ nln'l'.$$

Here $ll' = sp, sf, pd, pf$.

The term possibilities are just those outlined previously in Ar [3]. As shown, the grandparent term may be ^3P, ^1D, or ^1S. Taking the simplest case of $5s5p$ in Kr, the number of possible $J=1$ components is 14, with 3 of these being $^1P_1$, in strict $L-S$ coupling. We know, however, that $L-S$ coupling does not prevail, and we may expect a large number of excited states with $J=1$. Experimentally, one observes few of this potentially large number of resonances.

As in Ar, we can make crude estimates of the expected positions of resonances from the known levels of the ion [18, 19] and typical quantum defects for the s, p, d, and f electrons. Because the spectra observed are quite rich and because of screening and configuration interaction effects, such estimates cannot be sufficiently accurate to establish definite assignments.

In the cases of Ne and Ar a number of low-lying two-electron excitation states were identified. In Kr and Xe virtually none have been assigned. In the absence of good calculations, we can only identify series with high-lying members. Intensity sharing interactions appear to be responsible for the fact that we see any series at all.

In both Kr and Xe, quantum defects have been calculated for all the resonances to the available [18, 19] known limits. As a result of this analysis, only 28 resonances in Kr and 43 in Xe have been grouped into probable Rydberg series. In the Ar case, one experimental fact was very obvious—that of all the possible excited configurations, those of the type:—$3p^4 3dnl$ and $3p^4 4snl$ *dominated the spectrum*. Series such as $3p^4 4pns$ were hardly in evidence. This tendency is equally pronounced in Kr, where *all* of the series are of the type $4p^4 5snp$ or $4p^4 4dnp$.

Turning to table 3 (B), the unidentified series having a limit at 240300 cm^{-1} may be due to transitions to states $(^1D)5s(^2D_{3/2})np$. However, using Minnhagen's value for this limit [18], we must then invoke certain configuration interaction effects to explain the unusual run of effective quantum numbers (inside the brackets).

In Xe, if the present tentative assignments are correct, the emphasis on running electrons of odd parity is no longer evident. Indeed, there are apparently two series of the type $5p^4 6pnd$. Another series is tentatively labelled $6pnd$ (table 4 (E)) but the defects are more appropriate for a running p electron—forbidden on the grounds of nonconservation of parity *if* the state in Xe II has been correctly identified [19].

Also in table 4, the series (D) with an unidentified limit, may well be associated with a series of the type $5p^4 5dnf$.

Some of the more obvious series in Kr and Xe are indicated by lines above and below the spectra of figure 1. In Kr we can see the series A, B, C, F and G of table 3; in Xe we see the series A, B, D and I of table 4.

4. Conclusions

The one- and two-electron excitation resonances listed into the series above represent only one quarter of those observed. The basic problem is one of unfolding the complicated configuration interactions present, which displace levels from the locations expected on simple theoretical grounds, and produce intensity anomalies. Even within a single series, the profiles of the resonances may change with increasing principal quantum number. In others, only high series members are evident. It appears that a substantial theoretical effort will be required to analyze the spectra further, even in those regions where relatively few resonances occur. Original prints of the spectra shown in figure 1 can be made available to those interested in furthering the interpretation.

5. References

[1] Madden, R. P., and Codling, K., Astrophys. J. **141,** 364 (1965).
[2] Codling, K., Madden, R. P., and Ederer, D. L., Phys. Rev. **155,** 26 (1967).
[3] Madden, R. P., Ederer, D. L., and Codling, K., Phys. Rev. **177,** 136 (1969).
[4] Codling, K., and Madden, R. P., Phys. Rev. Letters **12,** 106 (1964).
[5] Codling, K., and Madden, R. P., Appl. Opt. **4,** 1431 (1965).
[6] Beutler, H., Zeit. Phys. **93,** 177 (1935).
[7] Samson, J. A. R., Phys. Rev. **132,** 2122 (1963).
[8] Madden, R. P., and Codling, K., J. Opt. Soc. Am. **54,** 268 (1964).
[9] Codling, K., and Madden, R. P., Phys. Rev. **A4,** 2261, (1971).
[10] Ederer, D. L., Phys. Rev. **A4,** 2263, (1971).
[11] Madden, R. P., Ederer, D. L., and Codling, K., Appl. Opt. **6,** 31 (1967).
[12] Fano, U., and Cooper, J. W., Phys. Rev. **137,** A1364 (1965).
[13] Reader, J., Epstein, G. L., and Ekberg, J. O., J. Opt. Soc. Am. (in press).
[14] Samson, J. A. R., Phys. Letters **8,** 107 (1964).
[15] Samson, J. A. R., Advances in Atomic and Molecular Physics (Academic Press Inc. New York 1966) Vol. 2, p. 177.
[16] Siegbahn, K., Nordling, C., Johansson, C., Hedman, J., Heden, P. F., Hamrin, K., Gelius, U., Bergmark, T., Werme, L. O., Manne, R., and Baer, Y., ESCA Applied to Free Molecules (North-Holland Publishing Co., Amsterdam 1969).
[17] Mansfield, M. W. D., Ph.D. Thesis, Physics Dept., Imperial College London (1969).
[18] Minnhagen, L., Strihed, H., and Peterson, R., Arkiv. för Fys. Bd 39 nr **34,** 471 (1969).
[19] Moore, C. E., Atomic Energy Levels, Nat. Bur. Stand. (U.S.) Circ. 467, Vols. **2** and **3** (1952, 1958).

(Paper 76A1–693)

JOURNAL OR RESEARCH of the National Bureau of Standards—A. Physics and Chemistry
76A, No. 1, January–February, 1972

A Reference Calorimeter for Laser Energy Measurements*

E. D. West, **W. E. Case,** **A. L. Rasmussen,** **and L. B. Schmidt****

Institute for Basic Standards, National Bureau of Standards, Boulder, Colorado 80302

(September 3, 1971)

Principles and detailed procedures are described for measuring laser energy and power in terms of electrical energy based on voltage, resistance, and frequency standards. The construction of a small isoperibol calorimeter used for the measurements is described. The calorimeter will accommodate 0.01 to 20 J and 4×10^{-5} to 1 W cw and is limited to a maximum pulse intensity of 0.1 J/cm². The standard deviation of comparison measurements using two calorimeters and a beam splitter is 0.08 percent when the smaller energy input is not less than 0.3 J. The estimated limits of systematic error for one calorimeter are ± 1.0 percent of the laser energy measured by the calorimeter.

Key words: Calorimetry; laser; laser calorimetry; laser energy measurement; laser power measurement.

1. Introduction

Calibration of a device for laser power and energy measurements is just the process by which the output of the device is translated into watts or joules based on standards maintained by the National Bureau of Standards. Evidently, methods of measurement which can compare laser outputs directly to the basic electrical standards offer considerable advantages by reducing the number of steps in the calibration process and the associated propagation of errors. These more direct methods of measurements have been the object of a program conducted at NBS [1, 2, 3, 4].[1] The main thrust of the work has been to apply calorimetric methods to the measurement of laser power and energy, and, through the use of beam splitters, to provide monitored beams of known energy for calibrating other measuring devices. More recently the work has been directed toward calorimeters which are simple enough for non-experts to operate, rugged enough to ship between laboratories, but accurate enough to provide a means of referring laser power and energy to the NBS electrical standards—a reference calorimeter. In this paper we describe principles and procedures for referring laser power and energy to electrical standards by means of a group of calorimeters, which we designate the C-series*, meeting most of the above requirements. It is contemplated that calorimeters of this type will be the basis of a service to calibrating laboratories to check on their overall accuracy and precision, much in the manner of the present system used with the standards of mass [5, 6].

Besides reducing the number of steps in the calibration process, calorimetry has other advantages. Calorimetry can be used to measure the energy in a pulse or, by the use of a suitable timer, a wide range of average power levels. A calorimeter properly designed and operated can make a valid comparison of energies independent of the time required to put the energy into the calorimeter. It is valid to compare energy in a pulse to cw energy put in over a 5 minute period, for example, or to compare a laser pulse to an electrical input of 10 to 300 sec duration. To conform with calorimetric tradition, we should probably restrict the term calorimeter to devices which can perform such time-dependent energy comparisons and relegate other so-called calorimeters to the category of thermal detectors. It is a technique that has been in use for about 100 years, so that a great deal of information on the design and operation of calorimeters is available [7, 8, 9, 10]. Calorimeters can be shaped to approximate a total absorber, to reduce the dependence of the calibration on the wavelength of the laser radiation. They can be constructed so that the calibration factor does not depend on where the laser beam strikes the calorimeter. This geometric variation of the calibration factor is rather common—not only in thermal devices, such as bolometers, thermopiles, and conduction calorimeters, but also in devices which respond to light quanta, such as photoelectric tubes. A calorimeter will retain its calibration factor for a very long time, unless it is damaged by a gross error, such as exceeding the maximum ratings for power density or energy. Using a beam-splitter, intercomparison and calibration of energy measuring calorimeters can be made independent of the laser stability, either in cw power or the energy of single or multiple pulses.

The requirements for laser power and energy measurements are extremely varied—wavelengths from 0.4 μm to 30 μm, continuous power levels from 10^{-6} to 10^{3} W, pulse powers in gigawatts, and

*Contribution of the National Bureau of Standards. Not subject to copyright.

**Quantum Electronics Division, National Bureau of Standards, Boulder, Colo. 80302.

[1] Figures in brackets indicate the literature references at the end of this paper.

*There have been three designs thus far, designated C1, C2, and C3. The first was a prototype. The principal difference between C2 and C3 is that C3 has an incomplete outer shield and a conical mirror so that the calorimeter can accommodate laser beams of larger diameter.

energies from 10^{-3} to 10^{3} J in single or repetitive pulses. Calorimeters are probably adaptable to a greater range of these requirements than other methods of laser power and energy measurements, but they too must be designed for a restricted portion of the problems. The practical operating parameters for the C-series calorimeters are summarized in table 1.

Although this paper describes a particular calorimeter in detail, its main purpose is to describe apparatus design and experimental techniques which any laboratory can follow to refer laser power and energy measurements to electrical standards.

2. The Theory of the Measurement

The C-series calorimeters, in common with the liquid cell calorimeter [3], are of the isoperibol type; that is they operate in an environment in which the temperature does not change with time. The theory for this type of calorimeter has been worked out in detail from its basis in the First Law of Thermodynamics and a generalized boundary-value heat flow problem describing isoperibol calorimeters [11]. The application of the theory to data reduction for temperatures taken at equal time intervals has been worked out for both a least squares computer program and a manual approximation [12]. The theory is summarized in the equation

$$W = E\left[T_F - T_I + \epsilon \int_{t_I}^{t_F} (T - T_\infty)\, dt\right] \qquad (1)$$

where W is the thermodynamic work done on the calorimeter, either by a laser beam or by a calibrating electrical current; E is the energy equivalent determined with a known work quantity; T is the temperature (or a quantity linearly related to the temperature [12]); ϵ is the cooling constant described below; and t is time. The work quantity W is the actual work done by the laser beam; an additional measurement is required to determine any power or energy in the beam which is scattered back out of the calorimeter. The quantity in brackets is traditionally called the corrected temperature rise ΔT_c and is determined from observations of the temperature over the time of the experiment. The quantity $E(T_F - T_I)$ is very nearly the change in the internal energy of the calorimeter and the product $E\epsilon$ times the integral is very nearly the heat exchanged between the calorimeter and the surroundings. The subscripts I and F refer to the initial and final rating periods, as outlined below. The initial and final temperatures must be observed during rating periods as defined by equation (2). The convergence temperature T_∞ is the temperature observed an infinite time, in a practical sense, after a disturbance of the calorimeter.

TABLE 1. *Operating parameters of C3 calorimeters*

Energy (cw)	0.03 to 3 J (0.01 to 20 J slightly less accurate)
Wavelength (with BK7 window)	0.4 to 2 μm
Aperture (max beam size)	2 cm
Cooling constant (reciprocal time constant)	0.003 s^{-1}
Power range (cw)	4×10^{-5} to 2 W
Max pulse intensity (pulse $< 10^{-3}$ s)	0.1 J/cm^2
Precision (standard deviation of an electrical calibration)	0.2 percent
Systematic error	less than 1.0 percent

The other equation essential to the measurement [11, 12, 13], is the following:

$$\frac{dT}{dt} = -\epsilon(T - T_\infty). \qquad (2)$$

When the temperature obeys this equation the calorimeter is said to be in a rating period. The measurement requires that rating periods both precede and follow the work input to the calorimeter. Two equations—one for each rating period—can be solved for the convergence temperature T_∞ and the cooling constant ϵ. Obviously T_∞ is the temperature when its rate of change dT/dt is zero. It is shown [11] that ϵ is the smallest eigenvalue of the heat flow problem; it can be varied by changing the thermal contact between the calorimeter and its constant-temperature environment, by removing air in the space around the calorimeter, for example.

It is important to note that equations (1) and (2) take into account the fact that the calorimeter has an opening for the laser beam and therefore must be somewhat influenced by objects in the room.Only the variation during an experiment of the radiation from the room will have an effect and this variation will appear in the random error of the calibration factor. For measurements at low light levels it may be preferable to keep objects in the room, such as supervisors, in fixed positions.

The use of equation (1) with actual data requires averaging techniques to achieve the highest accuracy and precision [12, 13]. We reduce data for the C-series and other isoperibol calorimeters by a simple least squares computer program [12]. Alternatively it may be accomplished manually. A simple manual method sacrifices very little precision or accuracy [12].

The least squares program in effect fits the integral of equation (2) to the data in the initial and final rating periods to obtain the best values for T_F, T_I, ϵ, and T_∞ in equation (1). The integration is carried out by the trapezoidal rule.

Equation (1) contains all of the quantities used in the computation of the energy equivalent E and is therefore the starting point for the analysis of errors in electrical calibration experiments.

Calorimetry compares laser energy actually absorbed to electrical energy. The energy in the beam as

it strikes the calorimeter is greater than the energy absorbed because of the losses in the window on the calorimeter and the small reflectance of the calorimeter proper. If W_l is the incident laser energy and τ_w is the transmission of the window, then $\tau_w W_l$ is the energy incident on the calorimeter proper, which absorbs a fraction α, so that the work quantity W in equation (1) is just $\alpha\tau_w W_l$. As we measure it, the quantity α also allows for a possible small heat exchange term. When the laser beam strikes the absorbing surface, that surface will be heated above the corresponding temperature in the electrical experiment. There will be a corresponding increase in the heat loss by thermal radiation over that accounted for by isoperibol theory. We call this the excess thermal radiation and treat it along with the absorption. Writing ΔT_c for the corrected temperature rise, we obtain the laser energy incident on the calorimeter window in terms of observable quantities

$$W_l = \frac{E\Delta T_c}{\tau_w \alpha}. \tag{3}$$

The determination of the energy in the laser beam depends on the determination of the four quantities on the right of equation (3). This paper will be concerned mainly with these quantities. Equation (3) contains all the quantities required to compute the energy from a laser beam and is therefore the starting point for the analysis of errors in laser experiments.

Systematic errors may also be due to inadequacies of the theory of the measurement. Problems related to the adequacy of the linear theory are discussed in references [11] and [12].

3. The Calorimeter

The calorimeter and its constant-temperature surroundings are shown in a schematic vertical section in figure 1a. Figure 1b is a photograph of the calorimeter as used. The apparatus is roughly cylindrical and symmetrical about a horizontal axis. The calorimeter proper, in which the laser beam is absorbed, consists of a main copper cylinder with a conical mirror on one end and a small cone closing the other. The mirror cone has a half-angle of 25° and accommodates a collimated-beam 2 cm in diameter by reflecting the outer part of it into the calorimeter. The small cone and the cylinder are blackened inside, by oxidizing the copper in C3–1, for example, to provide a good absorber that is reasonably resistant to high energy or power in the laser beam. This cavity construction avoids most of the error caused by variation of the absorptivity over the surface of the absorber. The outer surface of the calorimeter is gold-plated for corrosion resistance and low emittance for radiant heat transfer. The closed end, where most of the radiant energy is absorbed, is fitted with a thin copper shield in the form of a cylinder soft-soldered to a copper ring around the main cylinder. A calibrating electrical heater is wound under this shield. The shield serves to make the laser and electrical sources "equivalent" for evaluating heat transfer from the calorimeter. The problem with accounting for heat transfer is that the calibrating and laser sources cannot be in exactly the same geometrical locations and, therefore, will set up different temperature gradients. Although this geometrical effect can never be eliminated, it can, in principle, be made as small as desired. This principle is discussed in reference [11]. Application to our particular case is discussed below. The length of the cylinder represents a compromise between total absorption of radiation and the time required to make a measurement. A longer cylinder will absorb a larger fraction of the incident radiation, but the time required is increased roughly as the square of the length.

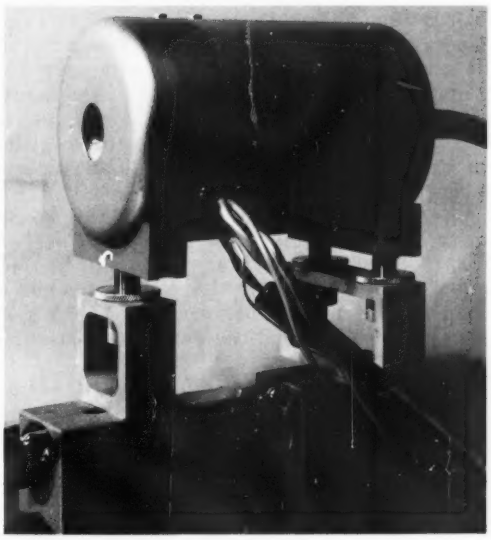

FIGURE 1b. *Photograph of a calorimeter of the C3 design.*

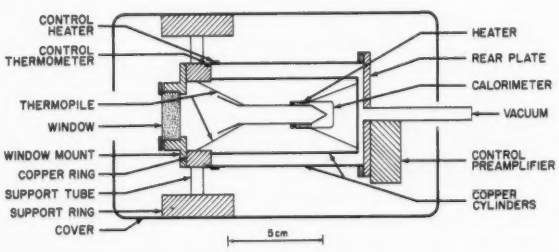

FIGURE 1a. *Diagram of C3 calorimeters.*

Laser radiation enters through the window and is absorbed inside the calorimeter. The temperature is measured by an 8-junction thermopile. Electrical calibrations are carried out by applying a voltage to the heater in the calorimeter.

The calibrating heater is about 100Ω of #40 manganin wire (.075 mm diameter) wound bifilarly to cancel inductive effects. The heater current leads are #36 copper (0.12 mm) about 8 cm long. Potential leads are attached midway along the current leads between the surface of the calorimeter and the inner surface of the surroundings. This construction avoids possible sig-

nificant systematic errors [14, 15] in comparing electrical energy to laser energy. The heat generated in the leads is 0.2 percent of the heat generated in the calorimeter. We estimate that the potential leads are located so as to allocate this 0.2 percent to better than 1/20 of itself (8 mm of wire in 16 cm of leads) for a maximum systematic error of 0.01 percent of the energy measured.

The calorimeter is suspended in the constant-temperature surroundings by an 8-junction thermopile of #36 alloy wires (0.12 mm). The thermopile output is approximately 600 μV/K. Pure metals were avoided for the thermopile because of their greater thermal conductivity and the consequent increase in the cooling constant.

The space between the calorimeter and its surroundings is evacuated to about 10^{-3} Torr (0.1 pascal) to reduce heat transfer and decrease the cooling constant. The smaller cooling constant makes the internal (stored) energy of the calorimeter about four times as large as the heat exchange term. On the basis of a few experiments made at pressures higher than usual we believe that the precision of the measurement is improved by reducing the pressure and that smaller power and energy can be measured. This observation is in accord with the practice in very accurate (0.01 percent) isoperibol calorimetry of making the heat exchange term about 1 percent of the internal energy [13].

The constant-temperature environment consists of a copper ring and two coaxial copper cylinders soldered to the ring. The inner cylinder is closed at the rear, but has four holes through which four junctions of the thermopile are drawn taut. The outer cylinder is closed by a rear plate with an "O" ring seal. A window, which in this case is a 1° wedge of borosilicate glass BK7, is mounted on the front of the constant-temperature surroundings. The wedge virtually eliminates possible problems with interference. It is mounted so that a line from the thinnest part to the thickest part is nearly horizontal. Vacuum seals for the window mount are made with "O" rings.

The constant-temperature surroundings are mounted in a heavy support ring by means of three thin-wall stainless steel tubes 0.6 cm in diameter. Aluminum covers are fastened to the support ring. Thermopile and heater leads are brought out through the support ring. This construction allows easy access to the inner parts of the calorimeter.

4. Temperature Control

The temperature control of the surroundings is a critical part of the measurement. The theory treats a temperature constant in time. If the temperature varies appreciably this will cause two errors: (1) The heat exchange term will be incorrectly determined, because no allowance is made for temperature variation. (2) The internal energy will be incorrectly evaluated, because of an error in temperature measurement. The internal energy is proportional to the temperature difference $T_F - T_I$. Since the thermopile with which we determined T_F and T_I has its reference junctions on the surroundings, a change in the reference junction temperature between the two temperature observations will appear directly as an error in the difference.

The controlled temperature is sensed by a resistance bridge as described by Maier [16], wound in the copper ring. The bridge consists of alternate arms of copper and manganin of about 100 Ω resistance fastened to the ring with an epoxy resin which cures at 100° C. The bridge balances at about 33° C. The bridge supply is 2 V DC. The output is amplified by an operational amplifier having a low offset voltage and gain stabilized with a feedback resistor. The amplified signal is fed to intermediate operational amplifiers which provide proportional and integral (reset) control to an output transistor. This transistor regulates the current in a 30-Ω control heater wound near the control thermometer on the outer surface of the surroundings.

The temperature is controlled to $\pm$ 0.1 mK as calculated from the gain of the operational amplifier and the bridge parameters. Our experience indicates that our temperature control is not the limiting factor in the precision of the measurement.

The temperature-controlled surroundings does not form a complete thermal enclosure for the calorimeter. Some heat is transferred by radiation through the window, although it is opaque to most room-temperature radiation, which is a maximum at 10μm. To this small extent the room is a part of the thermodynamic surroundings. In principle, the variation in room temperature would set a lower limit on the laser energy to be measured accurately in isoperibol calorimeters, but we have not yet established such a limit. Other factors are probably more important at the present time.

5. Operation of the Calorimeter

The output of the thermopile, which measures the difference between the temperature of the calorimeter and that of the temperature-controlled surroundings, is amplified by a D.C. amplifier linear to 0.01 percent, having a maximum gain of 10^5 at 100 μV full scale. The output of the amplifier (10 V max) is read by a digital voltmeter. At selected equal intervals of a few seconds, the voltmeter reading is transferred to a data coupler and then printed by a typewriter which simultaneously punches a paper tape.

In preparing for an experiment, the D.C. amplifier is allowed to warm up while the temperature control is established. About 15 min after the temperature of the surrondings is under control the rate of change of the calorimeter temperature in equation (2) becomes small enough to make a measurement. It is not unreasonable to wait until it is zero or nearly so, but it need not be zero. We keep the rate of change in the initial rating period less than about ten percent of the rate of change in the final rating period, because we believe that the increase in internal energy can be measured more accurately than heat exchange. If the calorimeter is

cooling rapidly in the initial rating period, the heat exchange term for the experiment will be large.

The experiment cannot be started until equation (2) is obeyed, but 15 min will usually prove more than adequate for this purpose. In any case, this point is checked in the computer data analysis.

When one is satisfied that equation (2) holds, a number of data points are logged (20 to 50) and then the electrical or laser input is made. We frequently log a minimum of 20 points at 4 s intervals (80 s) After the input enough points are taken to make sure that 20 to 50 points are in the final rating period when higher order exponentials have become negligible and equation (2) again holds. The final rating period can usually be started about 40 sec after the input is stopped. The computer program [12] prints deviations of individual points from the integral form of the equation (2) to show whether the rating period was started too soon. If it was, the calculation is merely repeated with a later set of points.

6. Electrical Calibrations

The electrical calibrating circuit diagram in figure 2 is based on principles long in use in calorimetry. The diagram is included to facilitate discussion of the errors in the measurement. Electrical calibrations are carried out using the calorimeter heater as a four-terminal resistor, measuring the D.C. current in the heater, the voltage across it, and the time the power is on. The heater current is determined from the voltage across a standard resistor. Two different standard resistors are used to accommodate different heater currents. The voltages are measured with digital voltmeters. These voltmeters and the standard resistor were calibrated by the RF Power, Current, and Voltage Section of NBS.

The power source for calibration is a D.C. supply operating up to 12 volts and 0.3 amp regulated to 0.1 percent. This regulation is a matter of convenience; the voltages required for the power computation are measured. The heater power is varied by changing the fixed value series resistor.

The time is read by a counter-timer with a built-in crystal-controlled oscillator. The oscillator is checked against a 100 kHz standard frequency supplied from the Time and Frequency Division of NBS. The timer is connected in parallel with the calibrating heater and is triggered by the voltage across the heater. Any leakage current in the timer is by-passed around the standard resistor to avoid a systematic error in the heater power.

We consider the errors in the electrical calibration by returning to equation (1). Abbreviating the corrected temperature rise by ΔT_c, we write the electrical work W_{el} done on the calorimeter

$$W_{el}=E\Delta T_c.$$

The electrical work is the product of the voltage V_h across the heater, the current given by the voltage

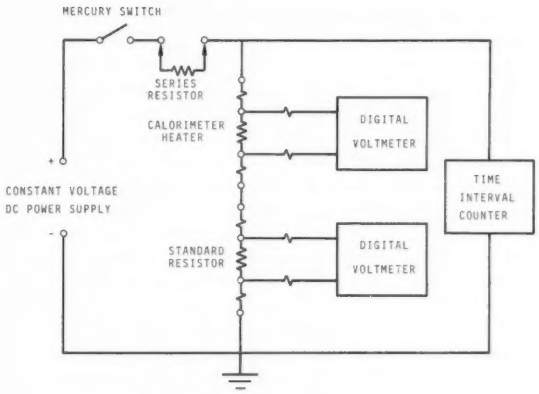

FIGURE 2. *Circuit for electrical calibration.*

Electrical work is the product of the voltage across the heater, the current, which is the voltage across the standard resistor divided by its resistance, and the time. Any current in the timer circuit by-passes the standard resistor.

V_r across the standard resistor divided by its resistance R, and the time t. Substituting for W and solving for E

$$E=\frac{V_h V_r t}{R\Delta T_c}.$$

The uncertainty in $E=f(V_h, V_r, t, R, \Delta T_c)$ due to systematic errors in the quantities V_h, V_r, t, R, and ΔT_c may be evaluated in the following manner. The systematic error δE in E caused by a systematic error δV_h in V_h is approximately

$$\delta E=\frac{\partial f}{\partial V_h}\,\delta V_h$$

However δV_h is unknown except that evidence has been presented that δV_h is limited by $\pm dV_h$. It follows that the error δE in E due to δV_h is limited by $\pm\left|\frac{\partial f}{\partial V_h}\right| dV_h$. Similarly, limits on the errors in E due to the other four parameters may be obtained. If the error sources are uncorrelated it is clearly unlikely that they will affect E in the same direction and at their extreme magnitudes. However it is conservative, and customary for a small number of error sources, to add the limits directly. Expressed as a fraction, the resulting limit to the systematic error in E is given by:

$$\frac{dE}{E}=\left|\frac{d\Delta T_c}{\Delta T_c}\right|+\left|\frac{dV_h}{V_h}\right|+\left|\frac{dV_r}{V_r}\right|+\left|\frac{dR}{R}\right|+\left|\frac{dt}{t}\right|$$

A more complete discussion is given by Ku [17]. The systematic error in ΔT_c is taken to be zero. A systematic error in ΔT_c would imply that either the laser or the electrical experiment affects the thermopile output in some way other than by changing the temperature of the junctions. It is possible for electrical leakage to bias the thermopile output, but checks for this source of error are easily made. A strip chart recorder connected to the nanovoltmeter will respond much more

448-417 O - 72 - 2

rapidly to electrical leakage than to the slow thermal effect, so that leakage is easy to detect as an instantaneous offset. Such an offset must be distinguished from a possible inductive effect of switching, which will appear as a spike and not an offset. We do not find either an offset or a spike due to an inductive effect. The major systematic errors are in the two voltmeters. The systematic errors in the voltage measurements are estimated to be less than 0.1 percent for one voltmeter and 0.03 percent for the other. The standard resistor calibration is stated to be accurate to 0.005 percent. No correction has been made for the temperature change of the standard resistor. This quantity is extremely small and, in any case, appears as part of the standard deviation in the electrical experiments. The counter-timer is compared to an NBS frequency accurate to about one part in 10^9. The trigger error was found to be less than 0.5 microsecond, which checks the manufacturer's specifications for the counter. The counter has a least count error as used of 1×10^{-5}, but this is a random error and will be taken into account in the standard deviation. We restrict the heater current to a minimum time of 1 sec, so that the estimated systematic error in the time interval due to time base, trigger error and counting error is negligible compared to the other systematic errors.

Limits to the systematic error in E are ± 0.15 percent obtained by summing the estimated limits of ± 0.11 percent, ± 0.03 percent and ± 0.005 percent estimated for V_h, V_r and R respectively. The heater lead error discussed above has been included as part of the error in V_h. The contributions of t and ΔT_c are taken to be negligible compared to 0.15 percent.

A chronological control chart for the electrical calibrations of calorimeter No. C3–1 is shown in figure 3. The individual determinations of the energy equivalent are plotted in the order in which they were made. The weighted average of all points is shown as a heavy dashed line. Points below 0.3 J were given 1/16 weight because of the poorer precision. The estimated standard deviation for an individual measurement is 0.22 percent and is plotted in the lighter dashed lines.

To ascertain whether the energy equivalent changes significantly with the total energy input, the energy equivalent of calorimeter C3–1 is plotted against energy

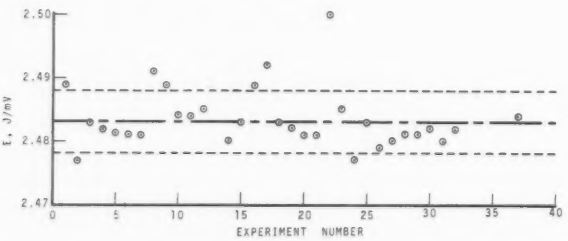

FIGURE 3. *Control chart showing calibration factor for C3–1 versus experiment number in chronological order.*

The heavy dashed line represents the weighted mean and the lighter dashed lines represent ± one standard deviation. The calibrations cover 7 months in the development of the measurement.

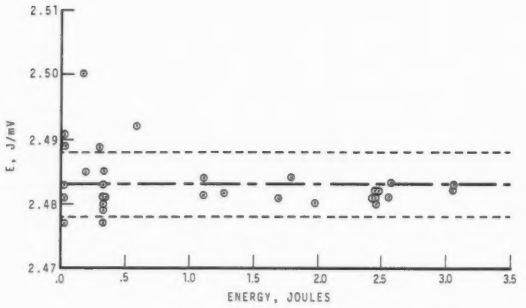

FIGURE 4. *Control chart of the calibration factor for C3–1 versus energy.*

The heavy dashed line represents the mean and the lighter dashed lines represent ± one standard deviation. Points below 0.3 J scatter more and were given less weight.

input in the control chart in figure 4. The lack of a significant trend with the energy input is evidence for the adequacy of the linear theory in this range. We have used the approximation that the thermopile emf is proportional to the temperature. This approximation may impair the accuracy for larger energy inputs. A few experiments at 10 J and 20 J appear to have good precision but differ a small but significant amount from the average. Present procedures sacrifice some accuracy in this range. Procedures now being developed for converting to a better temperature scale will probably extend the accurate range to these greater energies.

In a third control chart in figure 5 the energy equivalent is plotted against the cooling constant. The cooling constant is an indication of the pressure in the calorimeter; a smaller cooling constant corresponds to a lower pressure. The chart reveals no dependence of the energy equivalent on the cooling constant for calorimeter C3–1. We did find a variation of the energy equivalent of about 0.2 percent in an earlier calorimeter C2–2. While this effect can be taken into account, it is more convenient to maintain an adequately low pressure.

7. Arrangements for Optical Intercomparisons

A typical experimental arrangement for optical intercomparisons or calibrations is shown in figure 6.

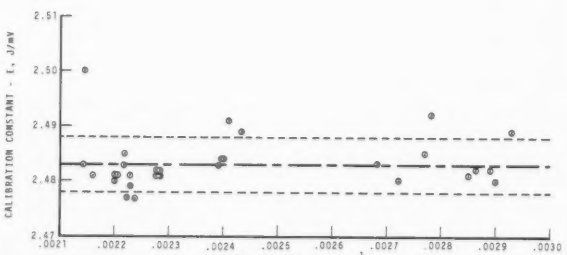

FIGURE 5. *Control chart of the calibration factor* E *plotted against the cooling constant to demonstrate the lack of a significant trend.*

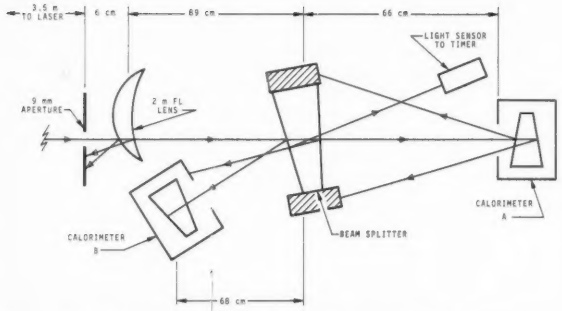

FIGURE 6. *Schematic diagram showing experimental arrangement for intercomparing two calorimeters.*

The aperture removes some unwanted divergent radiation. The lens reduces the beam diameter so that it will fit comfortably in the calorimeter. The first surface reflection is taken to the calorimeter at *B*. The second internal reflection from the beam splitter activates a light sensor which starts and stops a counter-timer.

In this arrangement the laser is an ion laser using argon or krypton gas. The beam is first passed through a 9 mm aperture stop placed about 3 meters from the exit port of the laser. The distance from the laser serves to reduce any possible effect on results of radiation due to pumping power. In this laser the pumping power is several thousand times the output power, so that a very small fraction of the pumping power could cause large errors in output power measurement. The pumping power radiation diverges rapidly, so that its effect decreases rapidly with distance from the exit port. Divergent radiation can cause a systematic error in comparison or calibration of devices having appreciably different entrance apertures or placed at different optical path lengths. Under these circumstances one device will capture more of the divergent radiation than the other. The purpose of the 9 mm aperture stop is to remove a small amount of extraneous laser radiation which makes an appreciable angle with the main beam. This extraneous radiation creates some confusion in setting up the experimental arrangement, but the main problem is that divergent radiation can cause systematic errors in comparison of two calorimeters having different apertures. The edge of the aperture must be kept out of any bright part of the beam to avoid diffraction effects and the corresponding divergence of the beam. The stop is painted black on both sides as a safety measure.

The beam passes next through a lens having a 2 m focal length. The purpose of the lens is to reduce the size of the beam so that there is no question that all of the beam enters the calorimeters. A shorter focal length lens may make the beam so small that a dust particle or imperfection in the optics may have an appreciable effect. The beam strikes the lens about 15 mm from the center so that reflections are carried out of the path of the main beam. The two largest reflections are absorbed on the back of the aperture stop.

The beam splitter is a 1° wedge of "c" cut sapphire. Wedges are used to make it easier to sort out the various reflections and to avoid possible problems with interference. The 1° angle is a compromise chosen to facilitate removal of undesired reflections without introducing problems related to the polarization of the laser beam. The laser beam strikes the first surface at an incident angle of approximately 2.3 degrees. This small angle is chosen to reduce dependence on the polarization of the laser beam. The first surface reflection is taken into calorimeter and the second surface reflection is terminated as a safety measure. The second internal reflection is taken to the silicon detector which triggers the counter-timer for time-interval measurements.

The alignment of calorimeters of the C3 type is simple. The beam is centered on the opening in the front of the calorimeter. The calorimeter is then oriented so that the two main reflections strike the black support of the beam splitter at the level of the main beam coming through. This arrangement assures that the angle of incidence on the window is the same as that used in determinig the transmission of the window. These reflected beams are at equal angles to the main beam, so that the effects of polarization can again be neglected, and both the main beam and the second internal reflection are practically centered on the absorbing cylinder in the calorimeter.

It is important to distinguish between the first surface reflection and the first internal reflection. The distinction is not apparent to the eye, so we use the scheme shown in the diagram in figure 7. When the two reflections straddle the main beam, the second internal reflection will be on the same side of the main beam as the first internal reflection.

8. Window Transmission Measurements

The arrangement for measuring the transmission of the window for C3 calorimeters is similar to that in figure 6. The calorimeter at A is moved to 1.1 m from the beam splitter and the window to be checked is placed midway between them. The window, a 1° wedge, is oriented so that the two brightest reflected beams make equal angles with the incident beam, as described in the preceding section. The second internal reflection does not enter the calorimeter, as it will when

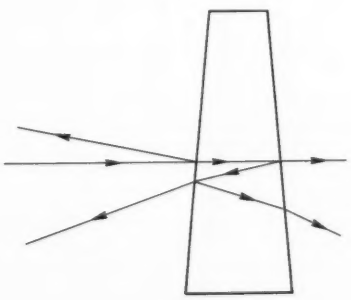

FIGURE 7. *Beam splitter illustrating method of distinguishing the front surface reflection and the first internal reflection.*

The splitter is oriented so that the two reflections make equal angles with the incident beam. The first and second internal reflections are then on the same side of the incident beam.

it is mounted on the calorimeter, so that the measured transmission must be increased by a few tenths of a percent, depending on the material of the window.

Since the transmission of the window is measured before it is placed on the calorimeter, a procedure has been developed which gives the measured transmission independent of the transmission of whatever temporary windows are on the calorimeters at the time.

The procedure starts with a determination of the ratio R of the energy W_t in the beam transmitted by the beam splitter to the energy W_r in the beam reflected from the beam splitter. Using subscripts A and B to refer to the calorimeters in those positions, we write from equation 3

$$R=\frac{W_t}{W_r}=\frac{E_A\,\Delta T_A}{\tau_A\,\alpha_A}\,\frac{\tau_B\,\alpha_B}{E_B\,\Delta T_B}. \tag{4}$$

Insertion of a window in the transmitted beam will reduce the energy transmitted to the calorimeter at A. Using primes to allow for a possible change in the laser output, we observe the following ratio

$$R'=\frac{\tau_w W'_t}{W'_r}=\frac{E_A\,\Delta T'_A}{\tau_A\,\alpha_A}\,\frac{\tau_B\,\alpha_B}{E_B\,\Delta T'_B} \tag{5}$$

As we would predict, the ratio W'_t/W'_r is observed to be independent of the laser power level, so that $W'_t/W'_r=W_t/W_r$. Substitution for this ratio in eq (5) from eq (4) gives the equation

$$\frac{\tau_w\,E_A\,\Delta T_A\,\tau_B\,\alpha_B}{\tau_A\,\alpha_A\,E_B\,\Delta T_B}=\frac{E_A\,\Delta T'_A\,\tau_B\,\alpha_B}{\tau_A\,\alpha_A\,E_B\,\Delta T'_B} \tag{6}$$

The transmission and absorption quantities for the two calorimeters appear on both sides of the equation and can be canceled. The energy equivalents E_A and E_B are constants, independent of the energy or ΔT_c over the operating range. Cancelling these and rearranging, we obtain the equation for the transmission of the window.

$$\tau_w=R'/R=\frac{\Delta T'_A\,\Delta T_B}{\Delta T_A\,\Delta T'_B}. \tag{7}$$

After the transmission is measured, the window is placed on the calorimeter. The transmission actually used is the measured transmission increased by a few tenths of a percent because the second internal reflection, which is discarded in the transmission measurement, enters the calorimeter when the window is mounted on the calorimeter.

Transmission measurements for calorimeter C3–1 at 676 nm are shown in Table 2. From these data we calculate the transmission of the window to be $\tau=0.9115$, including a correction of .0016 for the second internal reflection. The standard deviation of τ based on these measurements is 0.032 percent.

A systematic error in the transmission might arise (1) from gradual changes in the window between transmission measurements or (2) from nonuniform scattering or transmission by the glass. The first of these might come from slow formation of a coating of some kind. This kind of error can be avoided by repeating the transmission measurements at reasonable intervals. Measurements of the transmission of the window of calorimeter C3–1 made three months apart agree to 0.07 percent, although the first set of measurements was made with the calorimeter operating in air. In this case, the transmission of 0.9122 is the ratio of the energy measured with the window in its actual operating position to the energy measured with the window removed—no correction is necessary for the second internal reflection. The individual measurements are less precise without the window; the standard deviation is 0.11 percent. The 0.07 percent difference in the two values of the transmission is not significant at the 95 percent confidence level. Measurements on another window of the same type gave the value of 0.9122 for the transmission; this value is the average of nine measurements and its standard deviation is 0.025 percent.

TABLE 2. *Beam ratio data for C3–1 window*

R (eq. 4)	R' (eq. 5)
11.5482	10.5193
11.5511	10.5026
11.5549	10.5044
11.5436	10.5141
	10.5073
	10.5077
Ave 11.5494	10.5092
$s=0.0048$	0.0063

On the basis of the preceding information, we estimate that the systematic error in W_t due to error in measuring τ will not exceed ± 0.12 percent of τ, or 3 times the standard deviation plus an error of .0002 in the intensity of the second internal reflection.

9. Absorption by the Calorimeter; Excess Thermal Radiation

It is evident from equation (3) that the fraction α of the incident radiation absorbed by the calorimeter must be known accurately and that the error in the fraction absorbed enters directly into the over-all accuracy of the measurement. It is also possible that there is an excess of thermal radiation from C3–1 in the laser experiment. The absorbing surface will have to run slightly hotter relative to the thermopile than in the electrical experiment because the heat flows from this surface to the metal parts of the calorimeter. Both the scattered radiation and this excess thermal radiation are taken into account in our determination of the quantity α, which for brevity's sake we term the fraction absorbed.

The fraction absorbed by the calorimeter is measured with the experimental arrangement shown in figure 8. A small calorimeter R1, constructed on its own window mount is placed in the evacuated calorimeter space in such a way that it intercepts practically all of the radiation, including thermal radiation, escaping from the interior of the calorimeter C3–1.

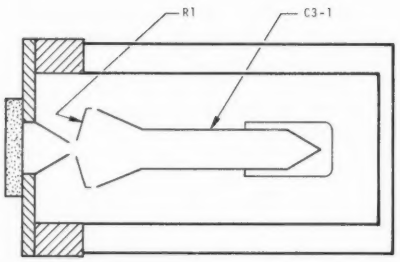

FIGURE 8. *Experimental arrangement for measuring the fraction of the incident radiation absorbed.*

A small laser beam passes through the aperture and through a slightly larger opening in the calorimeter R1 into the calorimeter C3–1, where most of the radiation is absorbed and measured. The small amount of radiation not absorbed by calorimeter C3–1 is absorbed and measured by calorimeter R1 and the fraction α absorbed by C3–1 is calculated from the two measurements.

Calorimeter R1 consists of an aluminum dish 2 cm in diameter and about 30 μm thick weighing 0.2 g with a 2.0 mm hole in the center. The dish is painted black on the surface facing calorimeter C3–1 and is mounted on three nickel-chromium alloy wires. The temperature is measured by a four-junction thermopile relative to the metal window mount, which is fastened to the temperature-controlled copper ring (fig. 1a). Calorimeter R1 is calibrated in a separate evacuated enclosure using a monitored 676 nm laser beam as in figure 6. The mean energy equivalent from 3 experiments is 4.35×10^{-4} J/μV and the standard deviation of the mean is 0.6 percent. The cooling constant for R1 as a separate entity is 0.02 s^{-1}.

Two types of experiments are carried out. In a laser experiment, a small beam enters calorimeter C3–1 through a 1.5 mm aperture and the 2 mm opening in calorimeter R1. The beam is focused at the aperture. In an electrical calibration, calorimeter C3–1 is heated in the usual way in order to observe the temperature change in R1 in response to thermal radiation from C3–1.

The major additional problem with two calorimeters in the same enclosure as in figure 8 is that they radiate energy to one another. In the present case, thermal radiation to R1 from C3–1 is far greater than the scattered laser radiation striking R1 directly and the problem is to extract the desired information from the data taken in the two experiments described above.

Since the scattered radiation is a small fraction $1-\alpha$ of the incident laser radiation, this fraction can be in error by a large percent of itself without impairing the determination of α and hence the over-all accuracy of the calorimetric measurement of laser energy. We take advantage of this by using a simplified heat flow problem as the theoretical basis for the experiment.

In the case of an electrical calibration at constant power, the temperature of calorimeter R1 will rise due to thermal radiation from calorimeter C3–1. For a laser input, laser radiation will be scattered back from C3–1 and absorbed by R1 along with the excess thermal radiation. The temperature of R1 will rise faster than it would due to the thermal radiation alone. Typical data for the two experiments normalized to the power level of C3–1, are plotted in figure 9. Both electrical and laser inputs were of 30 seconds duration starting at zero time.

To find the fraction $1-\alpha$ of the incident radiation received by R1 we treat the two calorimeters in a constant-temperature enclosure as a linear system, as in reference [11], and make use of the ideas of superposition and convolution. A constant electric power input to C3–1 will produce a typical time-temperature response in R1 because the calorimeters are thermally coupled by radiative heat transfer. A constant power R1 would produce a different response; the temperature would rise more rapidly for such a direct input. The time-temperature response of R1 to a laser input to C3–1 will be a superposition of these two responses: most of the laser beam is absorbed by C3–1, and R1 responds to the accompanying thermal radiation, but a small fraction of the beam will be scattered and absorbed on R1, giving a quicker response. The excess thermal radiation will produce a similar effect. The absorbing surface is a thin layer of copper oxide which will quickly reach a temperature excess proportional to the constant laser power, so that this component of the radiation to R1 would lag very little behind the input to C3–1. The observations therefore can account for the combined scattering of the laser beam and the excess thermal radiation. Knowing the time-temperature response of R1 to the thermal radiation from C3–1 in the electrical experiment, we

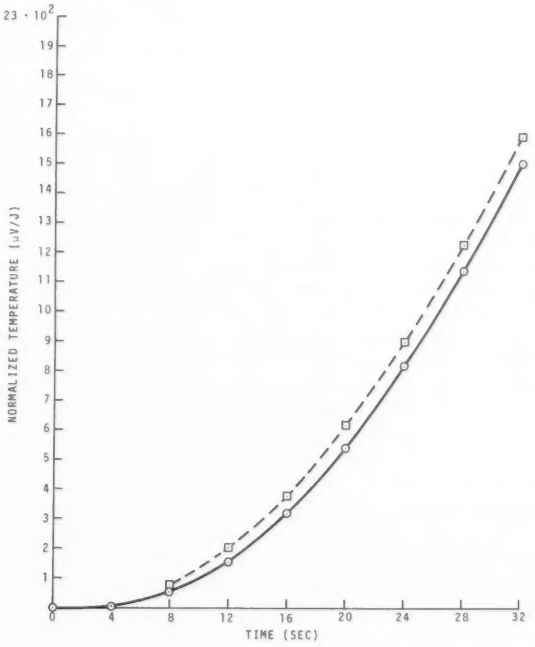

FIGURE 9. *Data for finding the absorption factor for calorimeter C3–1; comparison of time-temperature curves for calorimeter R1.*

In an electrical experiment "o" the temperature of R1 rises due to thermal radiation from C3–1; in a laser experiment "□" a small fraction of the incident radiation is scattered to calorimeter R1 so that its temperature rises faster than in the electrical experiment.

can subtract it from the time-temperature curve for the laser input and the remainder will be the response to the combined laser and excess thermal radiation not present in the calibration experiment.

The analysis of the resulting data is based on a simplified heat flow problem discussed by West and Churney [18] and by Churney, Armstrong and West [19]. Familiarity with their arguments will make the following discussion easier to follow. We begin by setting up an equation for the conservation of energy in calorimeter R1. The rate of increase in internal energy of R1 is the product of its heat capacity C and the rate of change of temperature dT/dt. When there is no direct laser input to R1 this increase in internal energy is equal to the rate of heat transferred to R1. This heat transfer is the product of a heat transfer coefficient h_s and the temperature difference $T_s - T$ between the constant-temperature surroundings and R1 plus the product of another heat transfer coefficient h_c and the temperature difference $T_c - T$ between C3–1 and R1. In equation form

$$CdT/dt = h_s(T_s - T) + h_c(T_c - T). \tag{8}$$

When $dT/dt = 0$, the system is in a steady state, which is characterized by the subscript ∞. For this steady state

$$0 = h_s(T_s - T_\infty) + h_c(T_{c\infty} - T_\infty). \tag{9}$$

For calorimetry we are not interested in this steady state, so long as it is steady. Subtraction of the steady-state equation gives

$$CdT/dt = -(h_s + h_c)(T - T_\infty) + h_c(T_c - T_{c\infty}). \tag{10}$$

The "temperatures" in equation (10) represent only that part of the temperature due to the laser input to R1; that part of the temperature due to the thermal part of the radiation has been subtracted from the composite observed temperatures before equation (10) is applied. The temperature C3–1, which has six times the heat capacity of R1, will not rise much due to radiation from R1. The last term in equation (10) will therefore not contribute much to the temperature rise of R1 because $T_c - T_{c\infty}$ is small, so we neglect this term. With this approximation and putting $b = (h_s + h_c)/C$, we integrate equation (10)

$$T - T_\infty = \mathrm{A}e^{-bt} \tag{11}$$

where $A = T_0 - T_\infty$ at time $t = 0$.

We now introduce the scattered laser power into the problem. Let A represent the temperature due to an input to R1 of 1 J at time $t = 0$; then $A = 1/C$. For an input of $p\,d\tau$ joules at time τ, equation (11) becomes

$$T - T_\infty = (p/C)e^{-b(t-\tau)}d\tau. \tag{12}$$

We can find the temperature due to a constant power input p starting at time $t = 0$ by integrating equation (12) over all elapsed time $\tau = 0$ to $\tau = t$:

$$\frac{T - T_\infty}{p} = \frac{1}{bC}(1 - e^{-bt}). \tag{13}$$

The temperature will have a maximum or new steady state value from which we obtain the scattered laser power p relative to the total power P to C3–1

$$\frac{p}{P} = bC\frac{(T_{\max} - T_\infty)}{(P\Delta t)}\Delta t.$$

The constant C is obtained by calibration as described above. The cooling constant b is obtained from a semi-log plot of $(T_{\max} - T_x) - (T - T_x)$. In the actual case these temperatures were divided by the electrical or laser power to C3–1, so that we obtain the fraction of the incident light scattered to R1. The results of four sets of paired electrical and laser experiments gave for the fraction scattered to R1 0.11 percent, 0.17 percent, 0.13 percent, 0.12 percent (chronological order). The average is 0.13 percent. The radiation lost through the hole in R1 is neglected. The 2 mm hole is 4 percent of the total area. The painted surface of R1 absorbs about 97.6 percent of the incident radiation, and contributes a negligible error (2.4 percent of 0.13 percent). The standard deviation of the mean of these measurements is 0.02 percent.

It is possible that the absorption varies with the position in the calorimeter. To investigate this possibility we made 7 measurements of the beam ratio with a beam 3 mm in diameter and 8 measurements with a beam slightly over 4 mm in diameter. The latter illuminates about twice as large an area. The mean of the first set was 11.527 and of the second set 11.528 with a pooled standard deviation of 0.0092. The difference is not significant, but, of course, the experiments are not sufficient to eliminate the possibility.

We estimate limits to the systematic error of ± 0.2 percent in the fraction absorbed α to allow for (1) a possible error in time, which affects the positioning of the two curves in figure 9, (2) three times the standard deviation of the mean, and (3) possible variations in the fraction absorbed with the location of the beam in the absorbing cavity. This estimated systematic error must be increased if part of the radiation strikes the gold-plated conical surface.

The gold-plated conical surface will reflect most of the incident radiation into the absorbing cavity, but some will be scattered back out of the calorimeter. We compare the response of the calorimeter to radiation incident on the conical surface and directly into the cavity, but this measurement is not simply a comparison of the fractions absorbed. A basic idea of calorimetric theory is that the method of accounting for heat exchange introduces an error in the comparison of laser beams absorbed at different locations in the calorimeter—the geometric effect discussed in the next section. Also, when the calorimeter is moved so that the beam strikes in a different place, the beam comes through a different part of the window, so there may be a small effect due to imperfections in the window. Radiation striking the gold-plated cone will therefore produce a different effect because of variation in absorption, the geometric effect and the

window. Measurements made with a 676 nm cw laser beam 4 mm in diameter are shown in table 3. The beam ratio is the ratio of the energy measured by C3–1 to the energy measured by the monitor. The largest variation is 0.8 percent less than the ratio measured at the center of the calorimeter opening. The only change made in these experiments is movement of C3–1.

The conical area is not ordinarily used for intercomparisons with other devices, so this systematic error ordinarily does not affect results of intercomparisons, although some allowance must still be made for possible geometric effects. When a large beam is used, a systematic error must be estimated based on the beam size and the above measurements.

10. The Geometric Effect

The theory of calorimetry predicts a systematic error in the comparison of two heat sources due to the fact that the errors in accounting for heat exchange with the environment do not exactly cancel when the sources develop heat in different parts of the calorimeter. This systematic error tends to decrease as the two sources are made more remote from the surface of the calorimeter and the heat exchange is made small. Tests can be performed with known sources in different locations such as a known beam striking the calorimeter in different places or using electrical heaters in two different locations. The latter technique is more precise because it eliminates some of the uncertainties associated with small beams, such as a change in scattering by the window. Larger beams are unsatisfactory because they allow too little variation in position and they tend to average out the geometric effect. We have performed the experiments described in the preceding section to test for the geometric effect in C3–1. These tests, described in the preceding section, do not separate the geometric effect from the effects of light scattering by the gold-plated surface and by the window. The experiment was carried out with a 4 mm beam striking the gold-plated surface. In practice, the beam is directed at the absorbing cavity and only that part of a beam outside a 1 cm diameter would strike the gold-plated surface. The largest variation in Table 3 (0.8 percent) therefore represents an unrealistically high estimate of the limits of systematic error due to the geometric effect.

TABLE 3. *Beam Ratios for Light Incident on Conical Surface*

	Beam ratio	Difference from center (percent)
Centered	11.532	.....
	11.525	.....
5 mm Right	11.436	−0.8
	11.433	
4 mm Right	11.468	−0.5
4 mm Left	11.514	−0.1
5 mm Left	11.490	−0.3
	11.495	

We have checked the geometric effect in an earlier version of the calorimeter C2–2 using two electrical heaters. The heaters are located at each end of the absorbing cylinder so that they greatly exaggerate the geometrical effect since a laser beam would mainly be absorbed at the closed end. The averages of six experiments with each heater are 3.614 and 3.606. The standard deviation of the mean is 0.0061, so that the two agree within twice the standard deviation. The difference between the average values is 0.22 percent. On the basis of the geometric effect in Calorimeter C2–2 and the data in Table 3, which may possibly be due to the geometric effect, we estimate limits to the systematic error of ± 0.5 percent of the energy measured. Note that we would have to make some allowance for a systematic error in any case because the tests that can be made are only indicative of the magnitude of the error; they do not prove that there is no possible way that a greater systematic error could not be incurred.

11. Precision and Accuracy of a Laser Energy Measurement

In analyzing the over-all precision and accuracy of the measurement we first examine some errors not yet considered.

Polarization. The angle of incidence of the laser beam on the calorimeter window is 0.75°. We calculate a maximum error of 4×10^{-5} in the transmission due to a change from vertically polarized to horizontally polarized light.

Thermal radiation from the window. Some of the incident radiation will be absorbed by the window, raising its temperature and increasing the thermal radiation to the calorimeter over that present during electrical calibrations. This radiation will not reach the calorimeter C3–1 in the absorption measurements because of calorimeter R1, figure 8, so it must be treated separately. We calculate that a 20 J laser input will raise the glass temperature 4 mK, assuming no heat loss from the glass. The resulting thermal radiation to the calorimeter will be less than 0.01 percent of the input.

Errors from data logging equipment. The gain stability and linearity of the data acquisition equipment does not contribute a systematic error. Short term instability will appear in the random error. If there is a long term drift it will show up on the chronological control chart for the energy equivalent, figure 3. Nonlinearity will limit the useful range of the calorimeter and will show up in the control chart of energy equivalent plotted against total energy input.

It is prudent here, as with the digital voltmeters, to utilize most of the scale of the instruments. In this way least count and percent-of-scale errors are minimized. Measurements and calibrations for a given energy should be made on the same scale.

Precision and accuracy of a measurement of a laser energy input. The error in measuring a laser input is estimated by reference to equation (3). Following the recommendations of Eisenhart [20], we present

the systematic and random errors separately. The limits of systematic error estimated above for the various factors are: $dE/E = \pm 0.21$ percent; $d\alpha/\alpha = \pm 0.2$ percent; $d\tau/\tau = \pm 0.12$ percent; thermal radiation from the window ± 0.01 percent; and the geometric variation $= \pm 0.5$ percent so the limits on the total systematic error are estimated to be the sum of these or ± 1.0 percent of the measured energy. As more data become available, better, and probably smaller, limits can be placed on the systematic errors.

The random error associated with the measurement of a laser energy W_l input to the calorimeter is a useful quantity because it is one of the criteria for judging its merits relative to other devices and its applicability to a particular problem. This random error is due entirely to the random error in determining ΔT_c since the other factors on the right-hand side of equation (3) are constants:

$$W_l = \frac{E \Delta T_c}{\tau \alpha} \tag{3}$$

To estimate the random error from repeated measurements on a particular laser we would have to depend on the stability of the laser, a dependence we are not willing to assume. In general, the random error is best estimated from electrical calibration data because the contribution from the electrical measurements can be negligible. In our particular case, experimental evidence indicates that the old digital voltmeters are not sufficiently stable. The standard deviation of an electrical calibration is 0.22 percent of the measured energy based on 18 determinations. The standard deviation as a percent of the measured energy increases as the measured energy decreases below about 0.3 J for both electrical and laser inputs, so we will confine our considerations to energies greater than 0.3 J. The pooled standard deviation based on three sets of beam ratio experiments (19 experiments, 16 degrees of freedom) is 0.08 percent. The standard deviation of a measurement with either calorimeter by itself must, of course, be less than 0.08 percent, but in any case this 0.08 percent is so much smaller than the 0.22 percent for electrical calibrations that we conclude that the electrical measurements themselves are making a major contribution to the random error.

For lack of a better basis, we estimate the random error associated with a laser energy input from the beam ratio measurements, making a few simplifying assumptions. Since the absorption of the cavity and the window transmission were measured only for C3–1, we first assume that these quantities are the same for both calorimeters. These quantities then cancel in equation (4) and we have for the beam ratio

$$R = E_A \Delta T_A / E_B \Delta T_B.$$

From propagation of error formulas we know that the standard deviation s_R of determinations of R can be expressed in terms of the standard deviations s_A and s_B of the corrected temperature rises ΔT_A and ΔT_B:

$$\left(\frac{s_R}{R}\right)^2 = \left(\frac{s_A}{\Delta T_A}\right)^2 + \left(\frac{s_A}{\Delta T_B}\right)^2.$$

If we assume that the standard deviations of ΔT_A and ΔT_B are dependent on the input energy and expressible as a constant fraction, that is, if

$$s_A/\Delta T_A = s_B/\Delta T_B,$$

then $s_A/\Delta T_A = 0.0008/\sqrt{2}$ or 0.057 percent. Assuming that $s_A = s_B$ and that they are independent of the energy input, and using $\Delta T_A = 17 \Delta T_B$ from the data, we estimate the standard deviation for the measurement of a laser input to be 0.02 percent at 0.1 J and 0.002 percent at 1 J. Until better electrical calibration data are available, we will use the more conservative estimate of 0.06 percent for the random error associated with a laser energy input to calorimeter C3–1.

One anticipated use for the C series calorimeters is in testing or calibration of other devices. For this purpose we currently use the experimental arrangement in figure 6. One calorimeter is used as a monitor (at either position) and the device to be tested is substituted at the other position. The beam ratio R is given by equation (4).

$$R = \frac{E_A \Delta T_A}{\tau_A \alpha_A} \frac{\tau_B \alpha_B}{E_B \Delta T_B}. \tag{4}$$

The standard deviation of this ratio is 0.08 percent. If a device to be calibrated is now substituted for B the ratio can be written in terms of the calibration factor F and the scale reading S of the device to be calibrated

$$R' = \frac{E_A \Delta T'_A}{\tau_A \alpha_A} \frac{1}{FS}.$$

If we are careful to maintain the experimental optical arrangement applying to equation (4), then $R = R'$ and we obtain for the calibration experiment

$$FS = \frac{\Delta T'_A}{\Delta T_A} \frac{E_B \Delta T_B}{\tau_B \alpha_B}.$$

The systematic error in the monitoring calorimeter at A cancels in this equation but the random error from our measuring system is increased because there are now two contributions from the monitor in ΔT_A and $\Delta T'_A$. The random error in the scale reading S will make an additional contribution to the error in the calibration factor F. The point is that the precision and accuracy of any measurement made with the C3 calorimeters will depend on what additional parameters are introduced. Each measurement must be examined from this point of view and planned so as to eliminate additional errors if possible.

12. Intercomparison of Calorimeters

The C series calorimeters are being proposed as devices for measuring laser energy relative to electrical standards, so it is important to compare C3–1 to some

of the liquid cell calorimeters which have been the main basis of NBS laser power and energy measurements [1, 3]. For this comparison we selected two liquid cell calorimeters having laboratory designations AF2 and AF6. The ratios of the energy measured in a designated calorimeter to the energy measured by the monitor calorimeter are given in Table 4. These ratios differ from others given in this paper because an extra lens was inserted so as to give a beam 1.1 cm in diameter on the liquid cells. To avoid a possible bias from interference effects, the liquid cell calorimeters were repositioned for each experiment. The means of measurements of AF2 and AF6 differ from the mean of the measurements for C3–1 by −2.1 percent and −1.8 percent respectively. Considering the claim of 2 percent for the "estimated calibration uncertainty" of a typical liquid cell calorimeter and the random and systematic errors considered earlier in this paper, the differences of about 2 percent seem somewhat too large. We therefore investigated two possible sources of systematic error in the liquid cell calorimeters: (1) the possibility that the small amount of energy reflected from the glass-solution interface might result in an appreciable systematic error and (2) the possibility that the geometric effect had been underestimated.

In the first series of experiments we used a 676 nm beam 4 mm in diameter and let it strike the liquid cell in the center and at distances of 4 and 5 mm from the center in all directions. The results are given in Table 5 in chronological order. The calorimeter was re-aligned after each measurement. The measurements have a standard deviation of 1 percent, appreciably larger than normal, but the mean differs from the value in Table 2 obtained with C3–1 by the same −2.1 percent. We conclude from these experiments that there may be a measurable interference effect if the liquid cell calorimeter is used with small beams, but that there is no appreciable geometric effect associated with the distribution of energy anywhere on the exposed surface of the window.

There is another possible systematic error due to the geometric effect in an axial direction, which comes about because heat generated by the electrical heater is closer to the silver housing than heat generated by a laser beam. In an electrical calibration the thermocouple located on the silver housing responds very quickly [1] but the glass surface will run colder during the heat input because heat must reach the glass through poor thermal conductors. In a laser experiment, the beam is mostly absorbed in the first millimeter of liquid behind the glass and the heat generated must flow to both the glass and the housing through poor thermal conductors. The net effect is that the integral $\int T\,dt$, which accounts for the heat exchange, is overestimated in an electrical experiment relative to a laser experiment and the resulting energy equivalent calculated from equation (1) is too small.

To get some estimate of the magnitude of this effect, we have taken a liquid cell calorimeter of an earlier design with an extra thermocouple mounted on the center of the front glass surface. An electrical calibration was carried out and the time-temperature data were taken with both thermocouples. The corrected rise was calculated for each of them by equation (1). The results differed by 3.6 percent. Since the thermocouple on the housing overestimates the heat exchange and the thermocouple on the glass underestimates it, the true value lies in between. Qualitatively, this is in the direction required to reconcile the differences between the liquid cell calorimeters and C3–1.

TABLE 4. *Intercomparison of calorimeters*

Date	Ratio AF2 to monitor	Ratio AF6 to monitor	Ratio C3–1 to monitor
4–28	10.538		10.773
	10.541		
4–29	10.545		10.777
	10.540		10.767
4–30		10.580	10.765
		10.577	
		10.587	
5–5	10.534		10.766
	10.546		10.782
	Mean 10.541	10.581	10.772
	s = .004	s = .005	s = .007

TABLE 5 *Beam ratio measurements with liquid cell calorimeter*

Ratio	Beam location
11.430	Center
11.213	5 mm right of center
11.382	Center
11.124	4 mm left
11.223	5 mm left
11.494	4 mm above
11.246	4 mm below
11.278	Center
11.310	Center
11.130	Center
11.327	4 mm right
Ave 11.287	
s = 0.117	

We are grateful to Peter V. Tryon for help with analysis of the data and discussions of the errors and to Barbara E. Orr for most of the computations.

13. References

[1] Jennings, D. A., West, E. D., Evenson, K. M., Rasmussen, A. L., and Simmons, W. R., NBS Technical Note 382 (1969).
[2] Jennings, D. A., and West, E. D., Rev. Sci. Instr. **41,** 565 (1970).
[3] Jennings, D. A., IEEE Transactions on Instr. and Meas. **IM 15,** 161 (1966).
[4] Birky, M. M., Applied Optics **10,** 132 (1971).
[5] Pontius, P. E., and Cameron, J. M., NBS Monograph 103, U.S. Government Printing Office, Washington, D.C. (1966).
[6] Pontius, P. E., NBS Technical Note 288, U.S. Government Printing Office, Washington, D.C. (1966).
[7] Experimental Thermochemistry, F. D. Rossini, ed., (Interscience Publishers, Inc., New York, 1956).
[8] Experimental Thermochemistry, Vol. II, H. A. Skinner, ed., (Intersicence Publishers, Inc., New York, 1962).
[9] Experimental Thermodynamics, Vol. I, (J. P. McCullough and D. W. Scott, ed., Plenum Press, New York, 1967).
[10] Roth, W. A., and Becker, F., Kalorimetrische Methoden zur Bestimmung Chemischer Reaktionswarmen, F. Vieweg and Son, Braunschweig, Germany (1956).
[11] West, E. D., and Churney, K. L., J. Appl. Phys, **41,** 2705 (1970).
[12] West, E. D., NBS Technical Note 396, U.S. Government Printing Office, Washington, D.C. (1971).
[13] Coops, J., Jessup, R. S., and Van Nes, K., in Experimental Thermochemistry, F. D. Rossini, ed., (Interscience Publishers, Inc., New York, 1956).
[14] Ginnings, D. C., and West, E. D., Rev. Sci. Instr. **35,** 965 (1964).
[15] West, E. D., and Ishihara, S., Rev. Sci. Instr. **40,** 1356 (1969).
[16] Maier, C. G., J. Phys. Chem. **34,** 2860 (1930).
[17] Ku, H. H., Precision Measurement and Calibration, NBS Special Publication 300, Vol. I, U.S. Government Printing Office, Washington, D.C. (1969) p. 331.
[18] West, E. D., and Churney, K. L., J. Appl. Phys. **39,** 4206 (1968).
[19] Churney, K. L., Armstrong, G. T., and West, E. D., Status of Thermal Analysis, NBS Special Publication 338, U.S. Government Printing Office, Washington, D.C. (1970).
[20] Eisenhart, C., in ref. 17, p. 21.

(Paper 76A1–694)

JOURNAL OF RESEARCH of the National Bureau of Standards—A. Physics and Chemistry
Vol. 76A, No. 1, January–February 1972

Accurate Calculations of Properties of the Two-Tube Electrostatic Lens. I. Improved Digital Methods for the Precise Calculation of Electric Fields and Trajectories

S. Natali,* D. Di Chio,* and C. E. Kuyatt

Institute for Basic Standards, National Bureau of Standards, Washington, D.C. 20234

(September 29, 1971)

Digital methods of high precision have been developed for the calculation of electric fields and trajectories in electrostatic lenses and a computer program was written to apply these methods to the two-tube lens. The increased precision results from the use of nine-point formulas in the relaxation calculation of potentials in place of previously used five-point formulas and from the use of an improved predictor-corrector method for the calculation of trajectories. Trajectories obtained with these methods are sufficiently precise to determine third-order aberration coefficients.

Key words: Calculation of electric fields; calculation of electron trajectories; electron lens; 9-point relaxation formulas; predictor-corrector method; two-tube electrostatic lens.

1. Introduction

As part of a general program to determine precise properties of electrostatic lenses, highly precise digital methods were developed for the calculation of electric fields and trajectories in electrostatic lenses and a computer program was written to apply these methods to the two-tube lens.[1] Our methods are easily generalizable to a wide class of electrostatic lenses.

The two-tube lens was chosen to test the digital methods since considerable data are available for this lens. Comparison of our results with the existing data shows that our methods have increased the accuracy of the calculation of lens properties and makes it possible, for the first time, to determine all of the third-order aberration coefficients of the two-tube lens for meridional trajectories.

2. Calculation of the Potentials

2.1. Statement of the Problem

Since a two-tube lens is cylindrically symmetric, the potential distribution inside the cylinders can be obtained by solving Laplace's equation in cylindrical coordinates (see fig. 1)

$$\frac{\partial^2 V(r,z)}{\partial r^2}+\frac{1}{r}\frac{\partial V(r,z)}{\partial r}+\frac{\partial^2 V(r,z)}{\partial z^2}=0 \qquad (1)$$

giving as boundary conditions the potentials on a contour starting and ending on the axis. Let V_1 and V_2 be the potentials on the two cylinders, D the inside diameter, and S the size of the gap between the two cylinders. The following boundary conditions were used : (see fig. 1)

AB: $V=V_1$
BC: $V=V_1$
CD: $V=V_1$
DE: $V=$ linear variation from V_1 to $\frac{1}{2}(V_1+V_2)$
EF: $V=\frac{1}{2}(V_1+V_2)$

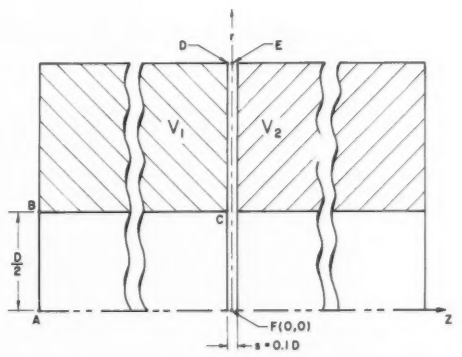

FIGURE 1. *Schematic of the two-tube electrostatic lens, showing r, z, coordinate system and boundary used in the relaxation calculation of potentials.*

$AF=BC=3.5D$. $CD=1.25D$.

* Present address: Istituto di Fisica, Universita di Bari, Bari, Italy.
[1] A detailed description of the computer program will be published separately.

In the actual calculations the distance AF is typically 3.5 D. It is sufficient to calculate the potentials only inside $ABCDEFA$ since cylindrical symmetry requires

$$V(-r, z) = V(r, z)$$

and the symmetry about the midplane of the lens requires

$$V(r, -z) = V_1 + V_2 - V(r, z).$$

In addition, once the solution $V_0(r, z)$ is obtained for the case $V_1 = 0$, $V_2 = 1$, then the solution for any other potentials V_1, V_2 on the tubes can be obtained from the formula

$$V(r, z) = V_1 + (V_2 - V_1)\, V_0(r, z)$$

2.2. Method of Solution

Laplace's equation (eq 1) was solved by the relaxation method on a matrix of equally spaced points [1].[2] The domain $ABCDEFA$ was divided into a network of equal sides h. Let i be the index running along the z axis, and j the index along r. Let $V_{i,j}$ be the potential at mesh point (i, j). Then the first order difference form of eq (1) is:

$$\frac{V_{i,j+1} - 2V_{i,j} + V_{i,j-1}}{h^2} + \frac{V_{i,j+1} - V_{i,j-1}}{2hr_j} + \frac{V_{i+1,j} - 2V_{i,j} + V_{i-1,j}}{h^2} = 0 \qquad (2)$$

From eq (2) the relationship between $V_{i,j}$ and the four adjacent points is easily obtained:

$$V_{i,j} = \frac{V_{i,j+1} + V_{i,j-1} + V_{i+1,j} + V_{i-1,j}}{4} + \frac{1}{8r_j}(V_{i,j+1} - V_{i,j-1}) \qquad (3)$$

Here we assume that r_j is measured in units of h.

On the axis where

$$\lim_{r \to 0} \frac{1}{r}\frac{\partial V}{\partial r} = \left(\frac{\partial^2 V}{\partial r^2}\right)_{r=0} \qquad (4)$$

eq (3) becomes

$$V_{i,j} = \frac{1}{6}(4V_{i,j+1} + V_{i+1,j} + V_{i-1,j}). \qquad (5)$$

In order to increase the accuracy of the relaxation method, we have expressed $V_{i,j}$ in terms of the potentials of eight adjacent points. This is accomplished by using Stirling differentiation formulas [2] for five points at equal intervals in both the r and z directions. The resulting formulas, including those special formulas required for points near the boundaries, are listed in table 1.

The basic nine-point formula used to relax the network is I1, and its specialization to axial points is I2. Formula I3 was obtained from I1 assuming symmetry about the axis. Formulas I4 and I6 which were used for points near the left boundary are just special cases of the five-point formulas given in eqs (3) and (5). Formula I5 was obtained from I1 and the relation

$$V_{M+1,j} = 2V_{M,j} - V_{M-1,j}. \qquad (6)$$

[2] Figures in brackets indicate the literature references at the end of this paper.

TABLE 1. *Formulas used for relaxation*

Number	Potential	Location	Formula
I1	$V_{i,j}$	x x x x ● x x x x	$V_{i,j} = \frac{1}{5}\left\{4 + \frac{1}{12}\left(4A - B + \frac{C}{j-1}\right)\right\}$ $A = V_{i,j-1} + V_{i,j+1} + V_{i-1,j} + V_{i+1,j}$ $B = V_{i,j-2} + V_{i,j+2} + V_{i-2,j} + V_{i+2,j}$ $C = V_{i,j-2} - 8V_{i,j-1} + 8V_{i,j+1} - V_{i,j+2}$
I2	$V_{i,1}$	x x - - - - - - - x - x - ● - x - x - - - - - - - Axis	$V_{i,1} = \frac{2}{15}\left\{\frac{4}{3}(V_{i-1,1} + V_{i+1,1} + 4V_{i,2}) - \frac{1}{12}(V_{i+2,1} + V_{i-2,1} + 4V_{i,3})\right\}$

TABLE 1. *Formulas used for relaxation*—Continued

Number	Potential	Location	Formula
I3	$V_{i,2}$	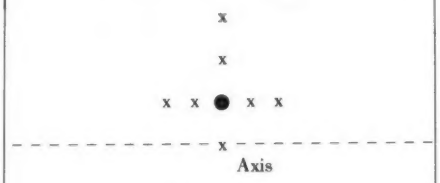	$V_{i,2}=\frac{1}{5}\left\{A+\frac{1}{12}(4A-B-C)\right\}$ $A=V_{i,1}+V_{i,3}+V_{i-1,2}+V_{i+1,2}$ $B=2V_{i,4}+V_{i-2,2}+V_{i+2,2}$ $C=8(V_{i,1}-V_{i,3})$
I4	$V_{2,j}$		$V_{2,j}=\frac{1}{4}(V_{3,j}+V_{2,j+1}+V_{2,j-1}+V_{1,j})$ $+\frac{1}{8(j-1)}(V_{2,j+1}-V_{2,j-1})$
I5	$V_{M-1,j}$	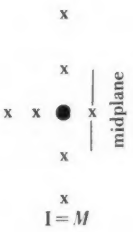	$V_{M-1,j}=\frac{12}{59}\left\{A+\frac{1}{12}\left(4A-B+\frac{C}{j-1}\right)\right\}$ $A=V_{M-1,j-1}+V_{M-1,j+1}+V_{M-2,j}+V_{M,j}$ $B=V_{M-1,j-2}+V_{M-1,j+2}+V_{M-3,j}+2V_{M,j}$ $C=-V_{M-1,j+2}+V_{M-1,j-2}+8(V_{M-1,j+1}-V_{M-1,j-1})$
I6	$V_{2,1}$	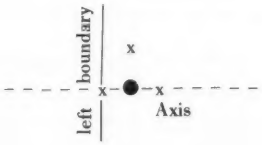	$V_{2,1}=\frac{1}{6}(4V_{2,2}+V_{3,1}+V_{1,1})$
I7	$V_{M-1,1}$	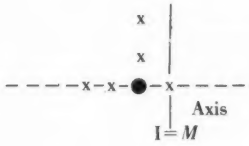	$V_{M-1,1}=\frac{12}{89}\left\{\frac{4}{3}(V_{M-2,1}+V_{M,1}+4V_{M-1,2})\right.$ $\left.-\frac{1}{12}(2V_{M,1}+V_{M-3,1}+4V_{M-1,3})\right\}$
I8	$V_{M-1,2}$	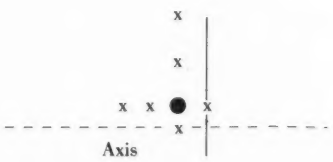	$V_{M-1,2}=\frac{12}{59}\left\{A+\frac{1}{12}(4A-B-C)\right\}$ $A=V_{M-1,1}+V_{M-1,3}+V_{M-2,2}+V_{M,2}$ $B=2V_{M-1,4}+V_{M-3,2}+2V_{M,2}$ $C=-8(V_{M-1,3}-V_{M-1,1})$
I9	$V_{i,j}$ (in gap)	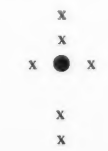	$V_{i,j}=\frac{2}{9}\left\{V_{i,j+1}+V_{i,j-1}+V_{i+1,j}+V_{i-1,j}\right.$ $-\frac{1}{12}(V_{i,j-2}+V_{i,j+2}-4V_{i,j+1}-4V_{i,j+1})$ $\left.+\frac{1}{12(j-1)}(V_{i,j-2}-8V_{i,j-1}+8V_{i,j+1}-V_{i,j+2})\right\}$

TABLE 1. *Formulas used for relaxation* – Continued

Number	Potential	Location	Formula
I10	$V_{i,N-1}$	tube x —— $j=N$ x x ● x x x	$V_{i,N-1}=\frac{2}{9}\left(A-\frac{B}{12}+\frac{C}{2(N-2)}\right)$ $A=V_{i,N}+V_{i,N-2}+V_{i-1,N-1}+V_{i+1,N-1}$ $B=V_{i-2,N-1}+V_{i+2,N-1}-4(V_{i-1,N-1}+V_{i+1,N-1})$ $C=V_{i,N}-V_{i,N-2}$

Formula I7 was obtained from I2 and eq (6), and I8 was obtained from I3 and eq (6). Formula I9 was derived by substituting into Laplace's equation the three-point formula for the derivative with respect to z and the five-point formulas for the derivatives with respect to r. Finally, Formula I10 was derived by substituting into Laplace's equation the three-point formulas for the derivatives with respect to r and the five-point formula for the derivative with respect to z.

2.3. Overrelaxation Procedure

The relaxation method is based on successive iterations of formulas I1 through I10 until the values assumed by the $V_{i,j}$ in two successive iterations differ by less than a preselected amount. Since the convergence is very slow, overrelaxation is used. The potential at point (i, j) after the mth iteration is then given by

$$V_{i,j}^{m}=V_{i,j}^{m-1}+\omega\left(V^{*m}_{i,j}-V_{i,j}^{m-1}\right) \tag{7}$$

where V^* is the potential calculated from formulas I1 through I10. The quantity ω is called the overrelaxation or acceleration factor, and its optimum value is problem dependent.

To determine ω we use the method of Carré [3]. Twelve iterations are first performed using a value $\omega=1.375$ which is certainly smaller than the optimal value ω_0, and a quantity W is calculated from the last three iterations:

$$W=\frac{\sum_{n=1}^{N}\left|V_n^{(m+1)}-V_n^{(m)}\right|}{\sum_{n=1}^{N}\left|V_n^{(m)}-V_n^{(m-1)}\right|}\cdot \tag{8}$$

The next estimate of the acceleration factor is then calculated from

$$\omega_l=\frac{2}{1+\sqrt{1-\dfrac{(W+\omega-1)^2}{W\omega^2}}} \tag{9}$$

Carré has shown the importance of not exceeding the optimum value ω_0, and finds empirically that a value

$$\omega_m=\omega_l-\frac{1}{4}(2-\omega_l) \tag{10}$$

is close to ω_0 but never exceeds it. The next twelve iterations are then performed using the acceleration factor ω_m and new estimates of W, ω_l, and ω_m calculated from eqs (8–10). The entire process is repeated twelve times or until two successive estimates ω_l, ω_{l+1} from eq (9) satisfy the inequality

$$\frac{\omega_{l+1}-\omega_l}{2-\omega_l}<0.05\cdot \tag{11}$$

Succeeding iterations are then made with the last estimate of ω_0 from eq (9) and are repeated until

$$\left|V_{i,j}^{m}-V_{i,j}^{m-1}\right|\cdot\frac{W}{1-W}\leqslant\epsilon \tag{12}$$

for all points on the mesh. The quantity ϵ is the desired precision for the potentials.

2.4. Program Organization

The radius of the lens was divided into 40 mesh points, with 320 mesh points along the axis for the half-lens. Hence, the program must relax 12,800 points. In addition, a 5×100 matrix is relaxed in the gap between the tubes, with 15 points overlapping the main matrix (see fig. 2). The time required to relax the complete network to a precision of $\epsilon=10^{-8}$ was about

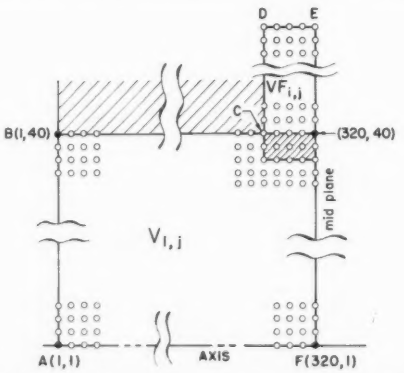

FIGURE 2. *Layout of mesh points showing overlapping of the main matrix with the auxiliary matrix used in the lens gap. Cross-hatched region is area of overlap.*

TABLE 2. *Axial potentials* V(z) *for the two-tube electrostatic lens*

$z=0$ at the center of the gap, $V_1=0$, $V_2=1$.

Z/D	$V(z)$						
	gap = 0.1 D			gap = 0			
	Present results	Read et al.	Grivet-Bernard	Verster	Read et al.	El-Kareh	Grivet-Bernard
0	.500000	.500000	.500000	.500000	.500000	.500000	.500000
.025	.467115	.467206	.467237	.466896	.466896		.467089
.05	.434532	.434703	.434753	.434101	.434101		.434462
.075	.402538	.402789	.402816	.401911	.401911		.402393
.1	.371399	.371715	.371679	.370599	.370599	.370606	.371138
.125	.341351	.341722	.341566	.340406	.340406		.340925
.15	.312592	.313005	.312673	.311533	.311533		.311952
.175	.285279	.285722	.285159	.284138	.284138		.284379
.2	.259528	.259991	.259146	.258334	.258334	.258327	.258327
.225	.235413	.235884	.234720	.234195	.234195		.233883
.25	.212969	.213438	.211932	.211752	.211752		.211093
.3	.173079	.173517	.171309	.171921	.171921	.171925	.170510
.35	.139566	.139957	.137100	.138518	.138518		.136380
.4	.111851	.112180	.108812	.110938	.110938	.110939	.108190
.45	.089212	.089479	.085771	.088438	.088438		.085253
.5	.070897	.071103	.067235	.070253	.070253	.070247	.066813
.6	.044436	.044536	.040802	.044009	.044009	.044012	.040542
.7	.027676	.027690	.024483	.027403	.027403	.027405	.024331
.8	.017178	.017141	.014590	.017006	.017006	.017003	.014504
.9	.010642	.010571	.008658	.010535	.010535	.010538	.008611
1.0	.006586	.006544	.005125	.006520	.006520	.006520	.005100
1.1	.004074	.004048	.003029	.004033	.004033	.004029	.003016
1.2	.002519	.002501	.001789	.002494	.002494	.002498	.001782
1.3	.001557	.001545	.001056	.001542	.001542	.001543	.001053
1.4	.000962	.000954	.000623	.000953	.000953	.000951	.000621
1.5	.000595	.000589	.000368	.000589	.000589	.000591	.000367
1.6	.000368	.000364	.000217	.000364	.000364		.000217
1.7	.000227	.000225	.000128	.000225	.000225		.000128
1.8	.000141	.000139	.000075	.000139	.000139		.000075
1.9	.000087	.000086	.000044	.000086	.000086		.000045
2.0	.000054	.000053	.000026	.000053	.000053		.000026
2.1	.000033	.000033	.000015	.000033	.000033		.000016
2.2	.000020	.000020	.000009	.000020	.000020		.000009
2.3	.000013	.000013	.000005	.000013	.000013		.000005
2.4	.000008	.000008	.000003	.000008	.000008		.000003
2.5	.000005	.000005	.000002	.000005	.000005		.000002

16 min on an IBM 360/65 computer, using double precision arithmetic (~ 15 decimal digits).

2.5. Results

In table 2 the potentials we obtain along the axis are compared with potentials obtained with other methods. Our potentials are in agreement with Verster's calculated potentials [4] to within 0.3 percent. The systematic difference between our results and those of Verster is probably due to a difference in gap size, which in the present calculations is 0.1 D while Verster uses a zero gap.

Also given are potentials calculated with the Grivet-Bernard approximation [6] for gap widths of 0.1 D and zero. The agreement with our results and also with the results of Verster is good close to the gap but becomes progressively poorer away from the gap as could be expected with the approximations used by Grivet and Bernard. Note that the systematic difference between our results and those of Verster is in the same direction and roughly the same size as the differences between the Grivet-Bernard potentials for the same gap sizes.

We have also included the results of a calculation for the zero-gap case carried out by El-Kareh [5]. The agreement with Verster's calculation is extremely good. It should be noted that in deriving lens properties,

El-Kareh uses the Grivet-Bernard approximation for the axial potentials.

The Grivet-Bernard approximation assumes a linear potential variation across the gap, while our method of continuing the relaxation process into the gap shows that the actual potential variation in the gap differs substantially from linear, as shown in table 3. To assess the effect of the nonlinear potential variation in the gap, we made special calculations assuming a linear variation in the gap. It was found that the change in axial potential and lens properties was less than 0.1 percent.

TABLE 3. *Linearly interpolated potentials compared to values from relaxation in the lens gap*

$V_1 = 1$, $V_2 = 20$. l = distance measured from edge of tube along inner diameter of the tube. s = gap width = 0.1 D.

l/s	Interpolated	Relaxation
0	1.000	1.000
.125	3.375	3.987
.25	5.750	6.315
.375	8.125	8.441
.5	10.500	10.500
.625	12.875	12.559
.75	15.250	14.685
.875	17.725	17.013
1.0	20.000	20.000

Finally, very recent calculations of Read et al. [7] are given. For the zero-gap case, the same infinite series was evaluated by Read et al., as by Verster and by El-Kareh. The agreement is extremely good. For the finite-gap case, Read et al. use a new method involving a determination of charge distributions on the tubes which give agreement with the boundary conditions. The agreement with our results is within 0.0005.

3. The Ray Tracing Program

3.1. Statement of the Problem

Using the potentials obtained by relaxation we must solve numerically the Lorentz equation:

$$\mathbf{F} = -e\mathbf{E} \tag{13}$$

where $\mathbf{F}$ is the force on the electron, and $\mathbf{E}$ is the electric field which must be calculated from the potentials at the mesh points. We restrict to the nonrelativistic case and to cylindrically symmetric electrostatic fields. In addition we consider only meridional rays, that is, rays lying in a plane through the axis of the lens. Equation (13) then reduces to the two equations:

$$\left.\begin{aligned} \frac{d^2z}{dt^2} &= -\frac{e}{m}E_z(r, z) \\ \frac{d^2r}{dt^2} &= -\frac{e}{m}E_r(r, z). \end{aligned}\right\} \tag{14}$$

Making the change of variables

$$\left.\begin{aligned} \tau^2 &= \frac{2e}{m}t^2 \\ u &= \frac{dz}{d\tau} \\ v &= \frac{dr}{d\tau} \end{aligned}\right\} \tag{15}$$

eqs (15) become

$$\left.\begin{aligned} \frac{dz}{d\tau} &= u(r, z) \\ \frac{du}{d\tau} &= -\frac{1}{2}E_z(r, z) \\ \frac{dr}{d\tau} &= v(z, r) \end{aligned}\right\} \qquad \frac{dv}{d\tau} = -\frac{1}{2}E_r(r, z). \tag{16}$$

We express the initial conditions as

$$\left.\begin{aligned} z(\tau_0) &= z_0 \\ \left(\frac{dz}{d\tau}\right)_0 &= u_0 \\ r(\tau_0) &= r_0 \end{aligned}\right\} \qquad \left(\frac{dz}{d\tau}\right)_0 = v_0. \tag{17}$$

3.2. Method of Numerical Solution

The numerical solution of the system of eqs (16) is of particular difficulty when a high precision is required. After a number of attempts using previous methods [1] we have chosen to use the predictor-corrector method of Hamming [8] where error and stability can be checked point by point. The important property of the classical predictor-corrector method is that it can be iterated until the required precision in the solution is reached. Hamming's method has the additional advantage of setting limits on the error which is accumulated along the integration. The method is stable in the sense that the difference between the numerical solution and the true solution decreases as the number of points of integration increases.

The predictor-corrector method seems therefore ideal for the calculation of trajectories. It has, however, two disadvantages: (1) It is not "self-starting"; hence, several starting points must be calculated with a different method. (2) It is desirable that at least several points be calculated in each mesh. Since the points are calculated at equal time intervals h it may happen

that when the electron accelerates the stability criteria require the interval h to be reduced by a factor of 2. Then the predictor-corrector method needs, to proceed, points calculated at intervals h/2, half of which do not exist. The trajectory must therefore be reinitiated with a different method.

Whenever required, the trajectory is reinitialized using the Runge-Kutta method. Reinitialization is only required when the electron moves toward the higher potential part of the lens. The effect of the occasional use of the Runge-Kutta method was checked by using the reversibility of electron trajectories. Several trajectories were calculated in both directions and found to coincide to within 0.01 percent.

A negligible error is expected when the trajectory is begun, this process being always performed in a zero-field region.

3.3. Trajectory Initiation by the Runge-Kutta Method

The numerical solution of eqs (16) uses the Runge-Kutta method to calculate the first seven points of the trajectory. Continuation of the solution then proceeds with the predictor-corrector method. Whenever the stability conditions fail to be satisfied at some point along the trajectory, the Runge-Kutta method is again applied to reinitialize the trajectory before continuing with the predictor-corrector method.

The Runge-Kutta formulas utilized are as follows:

$$\left.\begin{aligned} u_{i+1} &= u_i + \frac{1}{6}(m_0 + 2m_1 + 2m_2 + m_3) \\ r_{i+1} &= r_i + \frac{1}{6}(n_0 + 2n_1 + 2n_2 + n_3) \end{aligned}\right\} \quad (18)$$

$$z_{i+1} = z_i + \frac{1}{6}(k_0 + 2k_1 + 2k_2 + k_3)$$

$$v_{i+1} = v_i + \frac{1}{6}(p_0 + 2p_1 + 2p_2 + p_3)$$

where

$$k_0 = hu_i$$
$$n_0 = hv_i$$
$$m_0 = hE_z(r_i, z_i)$$
$$p_0 = hE_r(r_i, z_i)$$
$$k_1 = h \cdot \left(u_i + \frac{1}{2} m_0\right)$$
$$n_1 = h \cdot \left(v_i + \frac{1}{2} p_0\right)$$
$$m_1 = h \cdot E_z\left(r_i + \frac{n_0}{2}, z_i + \frac{k_0}{2}\right)$$
$$p_1 = h \cdot E_r\left(r_i + \frac{n_0}{2}, z_i + \frac{k_0}{2}\right)$$
$$k_2 = h \cdot \left(u_i + \frac{1}{2} m_1\right)$$
$$n_2 = h \cdot \left(v_i + \frac{1}{2} p_1\right)$$
$$m_2 = h \cdot E_z\left(r_i + \frac{n_1}{2}, z_i + \frac{k_1}{2}\right)$$
$$p_2 = h \cdot E_r\left(r_i + \frac{n_1}{2}, z_i + \frac{k_1}{2}\right)$$
$$k_3 = h \cdot (u_i + m_2)$$
$$n_3 = h \cdot (v_i + p_2)$$
$$m_3 = h \cdot E_z(r_i + n_2, z_i + k_2)$$
$$p_3 = h \cdot E_r(r_i + n_2, z_i + k_2)$$

with

$$E_z = -E_z/2$$
$$E_r = -E_r/2$$

E_z and E_r are obtained by differentiating with respect to r and z the Lagrange interpolating polynomial used to determine the potential at a given point from the values of the potentials at surrounding mesh points (see secs. 2.5 and 2.6).

The time interval $h = \Delta\tau$ at the beginning is taken equal to $1/(n\sqrt{V_{max}})$, thus assuring that the trajectory will be calculated for at least n points per mesh. Then h is reduced, if necessary, to satisfy the Hamming stability condition:

$$hk < 0.4$$

$$k = \left|\frac{\partial u}{\partial z}\right| + \left|\frac{\partial v}{\partial r}\right| + \left|\frac{\partial E_z}{\partial u}\right| + \left|\frac{\partial E_r}{\partial v}\right| \quad (19)$$

In this way, after the seventh point is calculated from the Runge-Kutta method, the predictor-corrector method is started with points spaced by an h which satisfies the stability condition.

3.4. Trajectory Continuation by Hamming "Predictor-Corrector" Method

The predictor-corrector formulas, as used in our program, are as follows:

Predictor

$$\left.\begin{aligned} z_{i+1}^{(0)} &= z_{i-3} + \frac{4}{3}h[2u_i - u_{i-1} + 2u_{i-2}] \\ u_{i+1}^{(0)} &= u_{i-3} + \frac{4}{3}h[2E_z(r_i,z_i) - E_z(r_{i-1},z_{i-1}) + 2E_z(z_{i-2},r_{i-2})] \\ r_{i+1}^{(0)} &= r_{i-3} + \frac{4}{3}h[2v_i - v_{i-1} + 2v_{i-2}] \end{aligned}\right\} \quad (20)$$

$$v_{i+1}^{(0)} = v_{i-3} + \frac{4}{3}h[2E_z(r_i,z_i) - E_z(r_{i-1},z_{i-1}) + 2E_z(r_{i-2},z_{i-2})]$$

448-417 O - 72 - 3

Modifier

$$\left.\begin{aligned}
\bar{z}_{i+1}^{(0)} &= z_{i+1}^{(0)} + \frac{112}{121}(z_i - z_i^{(0)}) \\
\bar{u}_{i+1}^{(0)} &= u_{i+1}^{(0)} + \frac{112}{121}(u_i - u_i^{(0)}) \\
\bar{r}_{i+1}^{(0)} &= r_{i+1}^{(0)} + \frac{112}{121}(r_i - r_i^{(0)}) \\
\bar{v}_{i+1}^{(0)} &= v_{i+1}^{(0)} + \frac{112}{121}(v_i - v_i^{(0)})
\end{aligned}\right\} \quad (21)$$

Corrector

$$\left.\begin{aligned}
z_{i+1}^{(j+1)} &= \frac{1}{8}[9z_i - z_{i-2} + 3h(u_{i+1}^{(j)} + 2u_i - u_{i-1})] \\
u_{i+1}^{(j+1)} &= \frac{1}{8}\{9u_i - u_{i-2} + 3h[(E_z^{(j)})_{i+1} + 2(E_z)_i \\
&\qquad - (E_z)_{i-1}]\} \\
r_{i+1}^{(j+1)} &= \frac{1}{8}[9r_i - r_{i-2} + 3h(v_{i+1}^{(j)} + 2v_i - v_{i-1})] \\
v_{i+1}^{(j+1)} &= \frac{1}{8}\{9v_i - v_{i-2} + 3h[(E_r^{(j)})_{i+1} + 2(E_r)_i \\
&\qquad - (E_r)_{i-1}]\}
\end{aligned}\right\} \quad (22)$$

Ultimate Value [superscript f indicates the final values from eqs (22)]

$$\left.\begin{aligned}
z_{i+1} &= z_{i+1}^{(f)} + \frac{9}{121}(z_{i+1}^{(0)} - z_{i+1}^{(f)}) \\
u_{i+1} &= u_{i+1}^{(f)} + \frac{9}{121}(u_{i+1}^{(0)} - u_{i+1}^{(f)}) \\
r_{i+1} &= r_{i+1}^{(f)} + \frac{9}{121}(r_{i+1}^{(0)} - r_{i+1}^{(f)}) \\
v_{i+1} &= v_{i+1}^{(f)} + \frac{9}{121}(v_{i+1}^{(0)} - v_{i+1}^{(f)})
\end{aligned}\right\} \quad (23)$$

The corrector formulae are iterated until the required precision in z, r, u, and v is reached, that is, until the inequalities (24) are satisfied:

$$\left.\begin{aligned}
\frac{h^2 b_{-1}^2 k_1 k_1'}{(1 - h b_{-1} k_1')} &< C_1 \\
\frac{h^2 b_{-1}^2 k_2 k_2'}{(1 - h b_{-1} k_2')} &< C_2
\end{aligned}\right\} \quad (24)$$

where

$$b_{-1} = \frac{3}{8}$$

$$k_1 = |u^{(j)} - u^{(j-1)}|_{i+1} + |v^{(j)} - v^{(j-1)}|_{i+1}$$

$$k_1' = \left|\frac{\partial u}{\partial z}\right|_{i+1} + \left|\frac{\partial v}{\partial r}\right|_{i+1}$$

$$k_2 = |E_z^{(j)} - E_z^{(j-1)}|_{i+1} + |E_r^{(j)} - E_r^{(j-1)}|_{i+1}$$

$$k_2' = \left|\frac{\partial E_z}{\partial u}\right|_{i+1} + \left|\frac{\partial E_r}{\partial v}\right|_{i+1}$$

$$C_1 = g(|z| + |r|)$$

$$C_2 = g(|u| + |v|)$$

g = maximum relative error

Before calculating the ultimate values z_{i+1}, r_{i+1}, u_{i+1}, v_{i+1}, the interval h is checked against the stability criterion (19). If satisfied, the next trajectory point is calculated with the same h. If not, h is divided by two until criterion (19) is satisfied. Starting with z_i, r_i, u_i, v_i seven points are then calculated with the Runge-Kutta method using the new h, and the solution continued.

If the stability criterion (19) can be satisfied with an interval twice as large, h is doubled and the next point with index $i+1$ is calculated from the points of index i, $i-2$, $i-4$, and $i-6$, instead of the usual i, $i-1$, $i-2$, and $i-3$.

3.5. Interpolation of Potentials

Potentials between mesh points are calculated by Lagrange interpolation. Let n be the degree of interpolation. Then

$$f(x) = \sum_{k=0}^{n} C_k(x) f(x_k) \quad (25)$$

where

$$C_k(x) = \frac{(x - x_0)(x - x_1) \ldots (x - x_{k-1})(x - x_{k+1}) \ldots (x - x_n)}{(x_k - x_0)(x_k - x_1) \ldots (x_k - x_{k-1})(x_k - x_{k+1}) \ldots (x_k - x_n)}$$

For the mesh we have used, the absciscae are uniformly spaced with unit interval. Putting $u = x - x_0$ we have

$$C_k(x) = \frac{u(u-1) \ldots (u-k+1)(u-k-1) \ldots (u-n)}{(-1)^{n-k} k!(n-k)!}. \quad (26)$$

For our problem, the most reliable results were obtained with interpolation of order 4.

The potential at point $P(r, z)$ is calculated as follows: (1) The potential at each point indicated in figure 3 with x and 0 is interpolated from the potentials in the corresponding column or row. (2) Two values of the potential at P are then interpolated, one from the potentials at points labeled x and one from those labeled 0. The average of these two values is taken as the potential at P.

3.6. Calculation of Electric Field

To find the two components of electric field, E_z and E_r, at any point, we differentiate the Lagrange interpolating polynomials [eqs (25) and (26)] with respect to z and r respectively. There results:

$$C_k'(x) = \frac{\sum_{i=0;\, i\neq k}^{n} u(u-1)\ldots(u-i+1)(u-i-1)\ldots(u-k+1)(u-k-1)\ldots(u-n)}{(-1)^{n-k}\, k!\,(n-k)!} \tag{27}$$

Here x represents either z or r as appropriate. Again $n=4$ was found to give the smoothest results and was used in the program.

3.7. Accuracy of Results

It is difficult to predict, a priori, the accuracies of the potentials and trajectories obtained from our program. The accuracy of the relaxation technique, using five-point formulas, is usually taken to be of order $1/N$ where N is the number of mesh points. Since we used the more accurate nine-point formulas we believe that the accuracy of the potentials is considerably better than 10^{-4} of the maximum potential.

In the trajectory calculations the parameter g in eq (24) gives the minimum precision with which each point of the trajectory is calculated. Focal lengths obtained from paraxial trajectories calculated with $g=10^{-5}$ satisfy the relationship

$$\frac{f_1}{f_2} = \sqrt{\frac{V_1}{V_2}} \tag{28}$$

to a precision of at least 10^{-5}, demonstrating that the estimate of precision is realistic.

Even higher precision can be obtained by reducing g with a consequent increase in computer time. The use of $g=10^{-5}$ is sufficient to determine accurate first-order focal properties and third-order aberration coefficients for the two-tube lens. Results will be reported in separate papers [9].

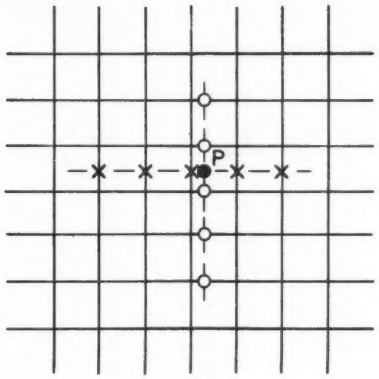

FIGURE 3. *Points* (x *and* 0) *at which potentials are interpolated to calculate the potential at an arbitrary point* P(r,z).

4. References

[1] Boers, J. E., Digital computer analysis of axially symmetric electron guns, IEEE Trans. on Electron Devices **12**, 425 (1965); Kirstein, P. T., and Hornsby, J. S., An Investigation into the use of iteration methods for the analysis of axially symmetric and sheet beam electrode shapes with an emitting surface, ibid **11**, 196 (1964).

[2] Hildebrand, F. B., Introduction to Numerical Analysis (McGraw-Hill, New York, 1956). For a convenient tabulation of numerical differentiation formulas, see McCormick, J. M., and Salvadori, M. G., Numerical Methods in FORTRAN, p. 40 (Prentice-Hall, Englewood Cliffs, New Jersey, 1964).

[3] Carré, B. A., The determination of the optimum accelerating factor for successive over-relaxation, Computer J. **4**, 73 (1963).

[4] Verster, J. L., On the use of gauzes in electron optics, Philips Res. Rpts. **18**, 465 (1963).

[5] El-Kareh, A. B., Design and analysis of symmetrical and asymmetrical electrostatic immersion lenses using a digital computer, Record of 10th Symposium on Electron, Ion, and Laser Beam Technology, p. 393 (Ed. L. Marton, San Francisco Press, 1969); El-Kareh, A. B., and El-Kareh, J. C. J., Electron Beams, Lenses, and Optics, Vol. I (Academic Press, New York, 1970).

[6] Grivet, P., Electron Optics, p. 164 (Pergamon Press, Oxford, 1965).

[7] Read, F. H., Adams, A., and Soto-Montiel, J. R., Electrostatic cylinder lenses. I. Two element lenses, J. Phys. E (Sci. Instr.) **4**, 625 (1971).

[8] Ralston, A., A First Course in Numerical Analysis (McGraw-Hill, New York, 1965).

[9] Natali, S., Di Chio, D., Uva, E., and Kuyatt, C. E., Accurate calculations of properties of the two-tube electrostatic lens. II. First order properties and P-Q curves. III. Aberration coefficients, submitted to Rev. Sci. Instr.; Kuyatt, C. E., Natali, S., and Di Chio, D., Third-order aberration coefficients of electron lenses, Proc. 11th Symp. Electron, Ion, and Laser Beam Technology, 1971, in press.

(Paper 76A1-695)

JOURNAL OF RESEARCH of the National Bureau of Standards—A. Physics and Chemistry
Vol. 76A, No. 1, January–February 1972

Dielectric Constant of Compressed Gaseous and Liquid Oxygen*

B. A. Younglove**

Institute for Basic Standards, National Bureau of Standards, Boulder, Colorado 80302

(August 25, 1971)

The dielectric constants of compressed gaseous and liquid oxygen were measured on ten isotherms at temperatures between 100 and 300 K and on the saturated liquid boundary at temperatures between 55 and 154 K. Densities ranged from 0.06 to 1.30 g/cm³ at pressures up to 33 MN/m². The dielectric constant measurements were combined with accurate density data to compute the Clausius-Mossotti (CM) function, $\left(\frac{\epsilon-1}{\epsilon+2}\right)\frac{1}{\rho}$. The CM function for oxygen decreases with density from a value of 0.1236 cm³/g at the low density limit to 0.1219 cm³/g near the triple point.

Key words: Clausius-Mossotti function; dielectric constant; oxygen.

1. Introduction

Very precise measurements of the dielectric constants of compressed gases and liquids, in principle, can give important information about the nature of molecular interactions. Also, density metering of fluids can be performed accurately and quickly by capacitance measurements when the dielectric constant as a function of density is known. Although such measurements have been reported for a number of simple fluids [1–6],[1] no accurate wide-range measurements of compressed oxygen have yet been reported. This paper presents accurate dielectric constant measurements and derived values of the Clausius-Mossotti function $\left(\frac{\epsilon-1}{\epsilon+2}\right)\frac{1}{\rho}$ for oxygen at pressures from the dilute gas to nearly three times the critical density and at temperatures between the triple point of the fluid (54.35 K) and 300 K.

2. Experimental Method

The dielectric constant was determined from the ratio of the capacitance when the cell was filled with fluid to the capacitance of the evacuated cell. The capacitor is essentially two coaxial cylinders of copper with the ends bearing on a common surface with three point contact in order to obtain high stability. Once assembled, the capacitor reproduced its vacuum capacitance versus temperature curve to within 1 part in 10^5 after temperature cycling to 55 K and pressure cycling to 34 MN/m² (~5000 psi). A detailed description of the capacitor, as used here, is given in reference [7].

The capacitance was measured with a commercial three-terminal a-c bridge, using tapped transformer windings in the ratio arms. The outer cylinder was operated at 10 V and 5 kHz, and the inner cylinder was connected to the detector side of the bridge. The bearing surfaces, sample holder, and outer conductor of the coaxial leads, and the bridge shield were grounded to form the third lead in the usual three-terminal connection for capacitance measurements.

2.1. Cryostat

The cryostat was all-metal construction, using liquid nitrogen as the refrigerant. The design is essentially that of Goodwin [8].

2.2. Sample Holder and Sample

The sample holder was made of electrolytic tough pitch copper. The sample temperature was regulated by nulling the platinum resistance thermometer emf against a fixed setting on a six dial potentiometer. The guard ring temperature was regulated to the sample temperature using a copper versus gold-cobalt thermocouple in a power control loop.

The sample was laboratory grade oxygen whose impurities, according to the supplier's specifications, were 17 ppm argon, 12 ppm hydrocarbon, 11 ppm krypton, 10 ppm nitrogen, and 2 ppm water. This would contribute less than 0.01 percent to the polarizability. Even so, the sample was further purified by passing it through a silica gel trap at 77 K.

* This work was carried out at the National Bureau of Standards under the sponsorship of the National Aeronautics and Space Administration Contract Order Number W-12, 745.
** Cryogenics Division, Properties of Cryogenic Fluids, National Bureau of Standards, Boulder, Colo. 80302.
[1] Figures in brackets indicate the literature references at the end of this paper.

2.3. Temperature, Pressure, and Density Measurements

The temperature was measured with a 25 Ω platinum resistance thermometer calibrated on the NBS–1955 and IPTS 1948 by the NBS Temperature Section. Adjustment to the IPTS 1968 can be made via reference [9]. The difference in CM, which results from neglecting the difference in the 1968 and 1948 scale, is small, usually much less than 0.2 percent. The calibration of the thermometer was checked periodically by measuring the vapor pressures of oxygen. The temperatures calculated from the vapor pressure measurements, using the tables of Weber [10], were within 4 millidegrees of that indicated by the thermometer calibration. Pressure measurements were made with a deadweight gage which communicates with the sample holder through a 0.056 cm i.d. stainless-steel capillary. Sensitivity of the pressure measurements were of the order of 10^{-4} MN/m^2; the accuracy uncertainty was about twice that of the sensitivity.

The fluid densities were determined from temperature and pressure measurements and the PVT surface of Weber [10]. Uncertainties in the densities were believed to be less than 1 part in 1000, except when within a few degrees of the critical temperature. Near the critical point the densities may be in error by as much as 1 or 2 percent.

TABLE 1. *Coefficients of Eqs (1) and (2)*

	Eq. (1)		Eq. (2)	
A	0.12361	(1) cm^3/g	0.12378	(2) cm^3/g
B	.00032	(4) cm^6/g^2	.00029	(3) cm^6/g^2
C	−.00121	(3) cm^9/g^3	−.00126	(2) cm^9/g^3
D			−.00000067	(9) cm^3/g K
σ	.000038	cm^3/g	.000032	cm^3/g

A, B, C, and D, are coefficients for eqs (1) and (2); numbers in parentheses are estimated imprecision in the last digit of the coefficients, σ is the rms deviation.

3. Results and Discussions

Measurements of dielectric constant, ϵ, in the compressed fluid as a function of pressure or density on isotherms, with the corresponding values of CM are listed in table 2.

Experimental values ϵ at saturation (previously reported [14]) are given in table 3.

Table 2. *Dielectric constant measurements and Clausius-Mossotti function of compressed fluid oxygen*

The densities were calculated from reference [10], using pressure and temperature as entries.

ρ g/cm^3	CM cm^3/g	ϵ	T K	P MN/m^2	ρ g/cm^3	CM cm^3/g	ϵ	T K	P MN/m^2
0.11189	0.12359	1.04207	300.0	8.357	.50289	.12343	1.19854	240.0	26.930
.09715	.12359	1.03646	300.0	7.285	.46111	.12346	1.18109	240.0	24.060
.08547	.12361	1.03203	300.0	6.432	.64417	.12333	1.25891	220.0	32.381
.07743	.12361	1.02899	300.0	5.842	.59875	.12334	1.23922	220.0	28.225
.06884	.12361	1.02575	300.0	5.210	.54679	.12343	1.21712	220.0	24.416
.05944	.12362	1.02221	300.0	4.514	.50155	.12347	1.19804	220.0	21.688
.05748	.12362	1.02147	300.0	4.368	.45605	.12350	1.17904	220.0	19.348
.05057	.12363	1.01887	300.0	3.853	.41352	.12353	1.16149	220.0	17.426
.42831	.12344	1.16747	280.0	29.929	.35296	.12359	1.13683	220.0	14.975
.32336	.12352	1.12481	280.0	21.660	.30203	.12360	1.11634	220.0	13.055
					.19101	.12359	1.07253	220.0	8.893
.25453	.12355	1.09740	280.0	16.934					
.19988	.12357	1.07598	280.0	13.367	.16248	.12361	1.06149	220.0	7.760
.47979	.12342	1.18883	260.0	30.045	.14137	.12363	1.05337	220.0	6.889
.44900	.12343	1.17602	260.0	27.557	.12719	.12364	1.04793	220.0	6.287
.39978	.12351	1.15583	260.0	23.972	.10949	.12365	1.04117	220.0	5.512
.35279	.12354	1.13672	260.0	20.885	.73510	.12309	1.29846	200.0	32.977
.31750	.12355	1.12249	260.0	18.720	.69060	.12325	1.27910	200.0	28.096
.25405	.12360	1.09725	260.0	15.041	.58556	.12342	1.23370	200.0	20.355
.20062	.12363	1.07630	260.0	12.042	.52454	.12348	1.20777	200.0	17.436
.13218	.12362	1.04984	260.0	8.173	.47881	.12351	1.18856	200.0	15.704
.12154	.12363	1.04577	260.0	7.558	.42090	.12356	1.16458	200.0	13.864
.10563	.12366	1.03970	260.0	6.628	.37127	.12359	1.14428	200.0	12.473
.07741	.12364	1.02899	260.0	4.943	.31196	.12360	1.12031	200.0	10.906
.05646	.12364	1.02109	260.0	3.656	.26489	.12363	1.10157	200.0	9.662
.54269	.12341	1.21535	240.0	30.066	.23176	.12355	1.08843	200.0	8.753

TABLE 2. *Dielectric constant measurements and Clausius-Mossotti function of compressed fluid oxygen*—Continued

ρ g/cm³	CM cm³/g	ϵ	T k	P MN/m²	ρ g/cm³	CM cm³/g	ϵ	T K	P MN/m²
0.21411	0.12362	1.08156	200.0	8.249	.09240	.12363	1.03467	160.0	3.030
.17476	.12365	1.06626	200.0	7.063	.05678	.12362	1.02121	160.0	2.044
.14312	.12363	1.05404	200.0	6.028	1.00036	.12260	1.41937	140.0	32.781
.15121	.12364	1.05715	200.0	6.301	0.96157	.12274	1.40146	140.0	22.396
.11825	.12366	1.04452	200.0	5.153	.95619	.12276	1.39899	140.0	21.171
.09658	.12369	1.03627	200.0	4.340	.94614	.12280	1.39438	140.0	19.011
.07901	.12370	1.02961	200.0	3.643	.93411	.12284	1.38887	140.0	16.638
.06087	.12371	1.02276	200.0	2.882	.92091	.12289	1.38282	140.0	14.281
.82534	.12298	1.33888	180.0	33.059	.90835	.12292	1.37707	140.0	12.264
.90737	.12281	1.37623	160.0	31.425	.89131	.12297	1.36928	140.0	9.852
.85543	.12300	1.35278	160.0	22.265	.87299	.12302	1.36094	140.0	7.643
.83368	.12306	1.34296	160.0	19.323	.83125	.12307	1.34187	140.0	3.910
.80273	.12313	1.32903	160.0	15.907	1.06595	.12249	1.45052	120.0	26.000
.75569	.12321	1.30800	160.0	12.142	1.03038	.12265	1.43397	120.0	14.194
.70663	.12328	1.28629	160.0	9.608	1.02298	.12267	1.43050	120.0	12.099
.65984	.12336	1.26584	160.0	8.119	1.01174	.12271	1.42523	120.0	9.136
.61350	.12344	1.24582	160.0	7.237	1.00032	.12274	1.41989	120.0	6.393
.55699	.12350	1.22162	160.0	6.644	0.98732	.12277	1.41380	120.0	3.579
.51907	.12351	1.20551	160.0	6.418	1.11997	.12242	1.47670	100.0	11.648
.40624	.12358	1.15857	160.0	6.048	1.10948	.12246	1.47171	100.0	7.287
.33530	.12357	1.12968	160.0	5.835	1.10182	.12249	1.46807	100.0	4.302
.29645	.12364	1.11415	160.0	5.670	1.09418	.12252	1.46443	100.0	1.490
.25265	.12364	1.09673	160.0	5.405					
.19693	.12366	1.07488	160.0	4.884					
.15111	.12368	1.05714	160.0	4.239					

TABLE 3. *Dielectric constant of saturated liquid oxygen*

The densities were calculated from reference [10] using temperature as an entry.

T K	ρ g/cm³	ϵ	CM cm³/g	T K	ρ g/cm³	ϵ	CM cm³/g
54.478	1.3066	1.56848	0.12192	114.000	1.0117	1.42522	.12270
55.000	1.3038	1.56740	.12199	118.000	.9869	1.41356	.12276
56.000	1.2993	1.56510	.12199	120.000	.9740	1.40751	.12279
62.000	1.2728	1.55178	.12206	122.000	.9607	1.40132	.12282
64.000	1.2638	1.54731	.12209	124.000	.9469	1.39488	.12283
68.000	1.2458	1.53835	.12213	126.000	.9327	1.38828	.12286
72.000	1.2276	1.52935	.12218	128.000	.9180	1.38152	.12291
76.000	1.2091	1.52026	.12224	130.000	.9026	1.37440	.12293
80.000	1.1903	1.51108	.12229	134.000	.8698	1.35939	.12300
84.000	1.1712	1.50179	.12235	138.000	.8333	1.34282	.12306
88.000	1.1518	1.49242	.12242	142.000	.7916	1.32400	.12313
92.000	1.1319	1.48272	.12245	146.000	.7416	1.30164	.12320
96.000	1.1116	1.47285	.12249	148.000	.7114	1.28828	.12323
100.000	1.0907	1.46280	.12254	150.000	.6755	1.27244	.12325
102.000	1.0800	1.45769	.12256	152.000	.6291	1.25206	.12320
104.000	1.0691	1.45250	.12259	153.000	.5980	1.23804	.12294
106.000	1.0581	1.44723	.12261	153.500	.5783	1.22904	.12265
108.000	1.0469	1.44188	.12263	154.000	.5533	1.21646	.12163
110.000	1.0354	1.43637	.12264				
112.000	1.0237	1.43089	.12268				

The Clausius-Mossotti function can be empirically represented by a polynomial in density,

$$\mathrm{CM} \equiv \left(\frac{\epsilon-1}{\epsilon+2}\right)\frac{1}{\rho} = A + B\rho + C\rho^2. \qquad (1)$$

The rms deviation of our measurements from eq (1) is 3.8×10^{-5} cm³/g, or about 0.028 percent in CM.

The departures of the compressed liquid isotherms from the saturated liquid curve, although not large, are believed to be a real effect. An addition of a linear term in temperature accounts for them quite well, i.e.,

$$\mathrm{CM} = A + B\rho + C\rho^2 + DT. \qquad (2)$$

The rms deviation of our measurements from eq (2)[2] is then 3.2×10^{-5} cm³/g in CM (0.03 percent).

Equation (1) may be inverted mathematically to give density as a function of the dielectric constant, providing a practical way to determine accurate fluid densities from capacitance measurements.

The low density limit of CM, i.e., the constant A of eq (1), is the polarizability of the isolated oxygen molecule. As yet this quantity has not been calculated theoretically. However, accurate dielectric constant measurements of Dunn [11] at standard temperature and pressure of O_2 (at $\rho=0.0013$ g/cm³) allows a check. His data when converted to CM differ from our measurements by 0.14 percent. This should be the upper limit of the uncertainty in CM, since it occurs at low density where the uncertainty is largest.

The appearance of figure 1 suggests that the second dielectric virial coefficient B might be negative. However, the overall fit of the data to eq (2) indicated that B is positive though small. Negative values for B have been found for He [4] and Ne [5], which have caused difficulties for the theorists. Levine and McQuarrie [12] point out that although the form of the correct theory for B is known, due to lack of knowledge of how the polarizability of a pair of molecules vary as a function of their separation, the usual simplification was to assume a constant polarization which is asymptotically valid in the limit of large separation. The result is that the predicted values of B are always positive. Other words of discouragement have been expressed by Jansen [13]. He attempted to account for the density variations of the dielectric constant from a quantum mechanical basis, starting from the Lorenz microscopic field equations with the concept of a local field. He concludes that such a theory is fundamentally ineffective in accounting for the experimental results within their accuracy, even at low densities.

[2] The coefficients are given in table 1.

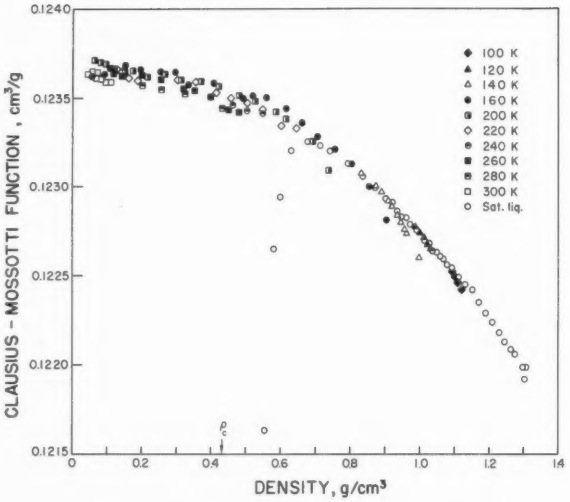

FIGURE 1. *CM function versus density for oxygen.*

The author expresses appreciation and acknowledgement to G. C. Straty for suggestions concerning the capacitor design, and to D. E. Diller and L. A. Weber for their assistance.

4. References

[1] Michels, A., and Kleerekoper, L., Physica **6,** 586 (1939), Michels, A., Lebesque, H. L., and de Groot, S. R., Physica **13,** 337 (1947); Michels, A., and Botzen, L., Physica **15,** 769 (1949).
[2] van Itterbeek, A., and Saepen, J., Physica **10,** 173 (1943).
[3] Jones, G. O., and Smith, B. L., Phil. Mag. **5,** 355 (1960).
[4] Johnson, D. R., Oudemans, G. J., and Cole, R. H., J. Chem. Phys. **33,** 1310 (1960).
[5] Amey, R. L., and Cole, R. H., J. Chem. Phys. **40,** 146 (1964); Orcutt, R. H., and Cole, R. H., Physica **31,** 1779 (1965); Orcutt, R. H., and Cole, R. H., J. Chem. Phys. **46,** 697 (1967).
[6] Stewart, J. W., J. Chem. Phys. **40,** 3297 (1964).
[7] Younglove, B. A., and Straty, G. C., Rev. Sci. Inst. **41,** 1087 (1970).
[8] Goodwin, R. D., J. Res. Nat. Bur. Stand. (U.S.) 65C (Eng. and Instr.) No. 4, 231–243 (1961).
[9] These temperatures may be converted to the IPTS 1968 from tables in Metrologia **35,** 5 (1969); see table on page 44, and Metrologia **47,** 5 (1969), see table on page 48.
[10] Weber, L. A., J. Res. Nat. Bur. Stand. (U.S.) 74A (Phys. and Chem.) No. 1, 93–130 (1970).
[11] Dunn, A. F., Canad. J. Phys. **42,** 53 (1964).
[12] Levine, H. B., and McQuarrie, D. A., J. Chem. Phys. **49,** 4181 (1968).
[13] Jansen, L., Phys. Rev. **112,** 434 (1958).
[14] Younglove, B. A., Advances in Cryogenic Engineering Vol. **15,** (Plenum Press, N.Y., 1970), p. 70.

(Paper 76A1–696)

JOURNAL OF RESEARCH of the National Bureau of Standards—A. Physics and Chemistry
Vol. 76A, No. 1, January–February 1972

Thermal Analysis of Calcium Sulfate Dihydrate and Supposed α and β Forms of Calcium Sulfate Hemihydrate from 25 to 500 °C

James R. Clifton

Institute for Applied Technology, National Bureau of Standards, Washington, D.C. 20234

(September 23, 1971)

Thermal studies were carried out on $CaSO_4 \cdot 2H_2O$ and the supposed α and β forms of $CaSO_4 \cdot 1/2H_2O$ in the region of 25 to 500 °C. using differential thermal analysis, thermogravimetry, and differential scanning calorimetry methods.

Two large endothermic effects and a smaller exothermic effect were found in the differential thermogram of $CaSO_4 \cdot 2H_2O$ while a single endothermic as well as an exothermic effect were found in the thermograms of the supposed α and β forms of $CaSO_4 \cdot 1/2H_2O$. However, the exotherm of α-$CaSO_4 \cdot 1/2H_2O$ had lower peak and first-break temperatures than that of the β-form. The peak and first-break temperatures of the endothermic effects of $CaSO_4 \cdot 2H_2O$ and α and B-$CaSO_4 \cdot 1/2H_2O$ and the exothermic effect of α-$CaSO_4 \cdot 1/2H_2O$ were pressure dependent, shifting to lower temperatures as the gaseous pressure within the DTA cell was decreased. The noted differences in the thermogrms possibly are due to kinetic factors because of the differences in crystallinity of the supposed α- and β-$CaSO_4 \cdot 1/2H_2O$.

No differences in the supposed α and β forms of $CaSO_4 \cdot 1/2H_2O$ were detected by thermogravimetry and differential scanning calorimetry studies. The formulation of a two-step dissociative process in the complete dehydration of $CaSO_4 \cdot 2H_2O$ was supported by the results of the thermogravimetry study.

Key words: α- and β-$CaSO_4 \cdot 1/2H_2O$; $CaSO_4 \cdot 2H_2O$; differential scanning calorimetry; differential thermal analysis; thermogravimetry.

1. Introduction

As a part of the continuing study of gypsum plaster [1][1] the properties of calcium sulfate dihydrate ($CaSO_4 \cdot 2H_2O$) and calcium sulfate hemihydrate ($CaSO_4 \cdot 1/2H_2O$) were studied by differential thermal analysis, thermogravimetry, and differential scanning calorimetric techniques. These investigations were undertaken in order to gain a more complete understanding of the dehydration processes of $CaSO_4 \cdot 2H_2O$ and to attempt to verify the existence of two forms of $CaSO_4 \cdot 1/2H_2O$.

In addition to the calcium sulfate hydrates, two types of anhydrous calcium sulfate exist, hexagonal (γ-$CaSO_4$) and orthorhombic (β-$CaSO_4$) forms [2]. The γ form results from the dehydration of the hydrates and is regarded as the low-temperature species, although it is apparently metastable and even at room temperature very slowly converts to the "high-temperature" species, β-$CaSO_4$ [2].

The main features in the differential thermal analysis previously reported for $CaSO_4 \cdot 2H_2O$ [3–7] are two large endothermic effects occurring below 250 °C. and a smaller exotherm found near 400 °C. Some other smaller effects have been reported [6], which were not observed in the present study. There is a lack of consistency in the values reported by different investigators for the temperatures of the main effects. This perhaps can be traced to uncertainties in the operating parameters of individually constructed instruments used in the past, and probably by using modern instruments of known operational characteristics more consistent results can be obtained. The present differential thermal analysis includes studies at normal atmospheric pressure and has been extended to determine the effects on the thermograms of reduced atmospheric pressures within the differential thermal cell, which has not been previously undertaken. Only brief studies of the thermogravigrams of $CaSO_4 \cdot 2H_2O$ have been reported [8]. Of particular interest in the thermogravimetric studies is the possibility of differentiating between two dehydration reactions when $CaSO_4 \cdot 2H_2O$ is completely dehydrated. Few, if any, differential scanning calorimetry studies on $CaSO_4 \cdot 2H_2O$ have been reported previously.

The existence of two forms of $CaSO_4 \cdot 1/2H_2O$, α and β, has not been firmly established. Apparent slight differences in densities [9, 10], heats of solutions [9], and gauging water requirements [11] have been cited as evidence for two forms of $CaSO_4 \cdot 1/2H_2O$. The

[1] Figures in brackets indicate the literature references at the end of this paper.

results of x-ray structural analysis are not at the present conclusive. Morris [12] found a slight difference in the x-ray powder diffraction patterns between the α and β forms when the value of 2θ was in the range of 48 to 50°. The pattern associated with α-$CaSO_4 \cdot 1/2H_2O$ in this region has triplet character (two slightly resolved small peaks on each side of a larger peak) whereas that of β-$CaSO_4 \cdot 1/2H_2O$ consists of a broad single peak. This difference has been attributed to stacking fault crystal imperfections by Morris [12] and to the intergrowth of a substructure of lower symmetry by Gay [13]. Based upon the results of optical and x-ray studies Flörke [14] suggested that both orthorhombic and triclinic varities of the hemihydrate can exist. Gay, however, recently reported [13] that only a monoclinic structure exists.

Recently, the two forms have been shown [1] to have the same infrared spectra. It has been reported [15] that the exothermic effect in the differential thermograms of α-$CaSO_4 \cdot 1/2H_2O$ occurs at a much lower temperature than in the β form, while other observers have claimed [16] that the thermogram of the α form does not exhibit any exothermic effect. Therefore, it was felt that a detailed thermal analysis study of the postulated α- and β-$CaSO_4 \cdot 1/2H_2O$ was desirable.

The results of differential thermal analysis, thermogravimetry, and differential scanning calorimetry studies of $CaSO_4 \cdot 2H_2O$ and the supposed α and β forms of $CaSO_4 \cdot 1/2H_2O$, carried out in the region of 25 to 500 °C., are presented and interpreted in this paper.

The α and β terminology used in this paper is a qualified notation referring to the supposed forms of $CaSO_4 \cdot 1/2H_2O$ and does not imply that their existence has been verified.

2. Experimental Procedure

2.1. Differential Thermal Analysis (DTA)

The DTA curves were recorded using a DuPont Model 900 DTA instrument [2] equipped with a microsample standard cell. The reference material was anhydrous reagent grade Al_2O_3 heated to 400 °C. for an hour and stored in a vacuum desiccator over phosphorous (V) oxide until used. The reference material treated in this manner gave a flat DTA curve. Gaseous pressures within the DTA cell were measured with the gage accompanying the instrument and may be subject to errors of about ±8 percent. Temperature measurements were made with chromel alumel thermocouples, using a reference junction temperature of 0 °C., and are accurate to within 2 °C. The thermocouples were calibrated using benzoic acid (National Bureau of Standards, Standard Reference Material No. 350). The vacuum system was able to reduce the residual pressure in the DTA cell to about 1 torr. Heating rates between 3 to 20 °C/min were used.

Evaluation of atmospheric conditions within the specimen compartment was complicated by the furnace and sample housing arrangement of the DTA cell. Samples were loaded into small borosilicate glass tubes, which were closed at one end; the thermocouple wires were inserted into the tubes above the sample, with the thermocouple junction being embedded in the sample. The thermocouple wires fitted tightly in the tube, thereby hindering the diffusion of water vapor from samples and increasing the partial pressure of water vapor in the specimen tube above that in the bulk atmosphere.[3] Furthermore, allowing nitrogen gas to flow into the DTA cell probably did not produce dynamic conditions within the specimen tubes, as the nitrogen gas was prevented by the tight fit to be an effective purging agent. For the same reasons, in studies carried out under reduced pressures the water vapor pressures within the sample tubes were probably much greater than the bulk residual pressures.

2.2 Thermogravimetry (TG)

The curves of weight-loss as a function of temperature were recorded using a combination of the DuPont 900 Thermal Analyzer (see footnote 2) and the 950 TGA Module.[4] The furnace atmosphere was either laboratory air or dry nitrogen gas. The weights of samples were 20 to 24 mg and weight suppressions between 16 to 20 mg were instrumentally set so that the full chart range on the ordinate scale would correspond to a weight loss of not more than 6 mg. Heating rates between 3 to 20 °C/min were used.

2.3 Differential Scanning Calorimetry (DSC)

A Perkin-Elmer DSC-1B Differential Scanning Calorimeter (see footnote 2) was used to measure the DSC curves. Both loosely and hermetically sealed sample capsules were used.

In order to determine the ΔH of dissociation for $CaSO_4 \cdot 2H_2O$, the instrument was calibrated using the ΔH of fusion of pure indium and tin as standards. Weights of samples were 3 to 5 mg. Heating rates between 5 to 20 °C/min were used.

2.4. Materials

a. $CaSO_4 \cdot 2H_2O$

Reagent grade $CaSO_4 \cdot 2H_2O$ was used in this study and was found by dehydration at 375 °C to contain the stoichiometric percentage of water (theoretical 20.9%, found 21.0%).

b. α-$CaSO_4 \cdot 1/2H_2O$

α-$CaSO_4 \cdot 1/2H_2O$ was prepared by the method outlined by Weiser and Milligan [17]. In this method an aqueous solution of $Ca(NO_3)_2 \cdot 4H_2O$ was added to a mixture of dilute nitric and dilute sulfuric acid and the

[2] Certain instruments and materials are identified in this paper in order to adequately specify the experimental conditions. In no case does such identification imply recommendation or endorsement by the National Bureau of Standards, nor does it imply that the material or instruments are necessarily the best available for the purpose.

[3] Because of the nonequilibrium conditions the gaseous constituents and pressures within the DTA cell were probably not homogeneous; therefore, the average atmospheric conditions are denoted by the term "bulk atmosphere."

[4] Refer to footnote 2.

resulting precipitate was allowed to age for 14 days at 50 °C. The white product contained the stoichiometric amount of H_2O (theoretical 6.62%, found 6.68%) and gave the differential thermogram [15] and x-ray powder diffraction pattern [12] ascribed to α-$CaSO_4 \cdot 1/2H_2O$.

c. β-$CaSO_4 \cdot 1/2H_2O$

β-$CaSO_4 \cdot 1/2H_2O$ was prepared from $CaSO_4 \cdot 2H_2O$ by two completely different dehydration methods. In one method samples of $CaSO_4 \cdot 2H_2O$ were dehydrated in an air oven at 150 to 175 °C. for three to twelve hours, to give γ-$CaSO_4$. This γ-$CaSO_4$ was allowed to equilibrate with laboratory air of 50 percent relative humidity at 22 °C. This resulted in the uptake of water with the final product having slightly more than the stoichiometric amount of H_2O, ranging from 0.54 to 0.57 moles of H_2O per mole of $CaSO_4$. The extra quantity of H_2O possibly has zeolitic character since Saito has reported [18] that NMR studies suggest the existence of two forms of water in $CaSO_4 \cdot 1/2H_2O$, one of which is zeolitic.

An alternate method was the removal of 1 1/2 molecules of H_2O from $CaSO_4 \cdot 2H_2O$ by vacuum line techniques at 100 °C. It was necessary to anneal the product at 100 °C. for 60 hours as otherwise an impure material was obtained which consisted largely of β-$CaSO_4 \cdot 1/2H_2O$ and about 5 percent of $CaSO_4 \cdot 2H_2O$ and γ-$CaSO_4$.

The x-ray powder diffraction patterns and differential thermograms of products from both preparative methods were identical to those reported for authentic β-$CaSO_4 \cdot 1/2H_2O$ [12, 15].

3. Results

3.1. Differential Thermal Analysis

Several of the differential thermograms of $CaSO_4 \cdot 2H_2O$, measured under different bulk atmospheric conditions in the DTA cell, are reproduced in figures 1 and 2. Decreases in the peak temperatures,[5] T_{peak}, and the first-break temperatures (see footnote 5), T_{fb}, of the two endothermic effects were observed when the gaseous pressure in the cell was reduced and when the residual pressure approached 1 torr the second endothermic curve had either merged with the first curve or had vanished. The peak temperatures and, when measurable, the first break temperatures are listed in table 1. The T_{peak} and T_{fb} of the exothermic effect observed in the differential thermograms of $CaSO_4 \cdot 2H_2O$ were not sensitive to changes in the gaseous pressures.

A phase diagram constructed by plotting peak temperatures of the endothermic and exothermic effects versus the atmospheric pressures within the DTA cell is shown in figure 3 for $CaSO_4 \cdot 2H_2O$. DTA curves obtained under a static nitrogen atmosphere were similar to those observed with supposed dynamic nitrogen flow.

[5] The peak temperature is the temperature of the apex of an endothermic or exothermic effect. The first break temperature denotes the temperature at which the curve first deviates from the base line due to either an endothermic or an exothermic effect.

TABLE 1. *Peak and first-break temperatures of endothermic DTA curves of* $CaSO_4 \cdot 2H_2O$

Bulk pressure (torr)	First curve		Second curve
	T_{peak} [a] (°C)	T_{fb} [b] (°C)	T_{peak} [c] (°C)
760	150	126	197
590	147	123	179
380	144	121	162
138	133	112	147
74	130	109	130
1	123	99	[d]

[a] T_{peak} is the peak temperature.
[b] T_{fb} is the first-break temperature.
[c] Because of overlapping curves not possible to determine T_{fb} for the second curve.
[d] Second curve had detected at 1 torr.

In figures 4 and 5 are shown the DTA curves of β-$CaSO_4 \cdot 1/2H_2O$ recorded, respectively, with a dynamic N_2 atmosphere of ca. 760 torr and with a small residual pressure (ca. 1 torr) in the DTA cell. The heating rate was 12 °C/min. The endothermic peak has the same temperature-pressure behavior (table 2) as previously noted for the second endothermic curve of $CaSO_4 \cdot 2H_2O$. The position and shape of the small exothermic peak, $T_{peak} = 375$ °C and $T_{fb} = 322$ °C, were not significantly affected by changes in atmospheric pressures in the DTA cell.

The DTA curve of α-$CaSO_4 \cdot 1/2H_2O$, recorded with an N_2 atmosphere of ca. 760 torr in the DTA cell and a heating rate of 12 °C/min is shown in figure 6. Results of pressure dependence studies on the shape and position of the endothermic peaks are reproduced in figure 7 and the values of T_{peak} and T_{fb} are listed in table 2. The position of the endothermic effect of α-$CaSO_4 \cdot 1/2H_2O$ shifts to lower temperatures with reductions in the gaseous pressure in the DTA cell. The small exothermic effect also has a similar temperature-pressure behavior.

The differential thermogram of an equal molar mixture of α and β-$CaSO_4 \cdot 1/2H_2O$ includes the small

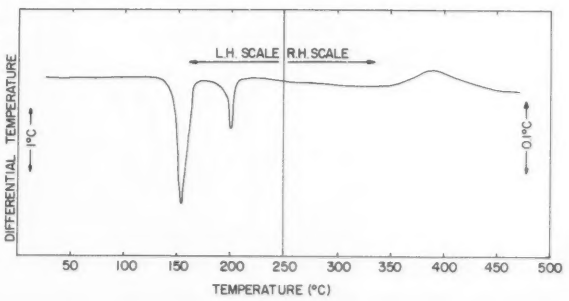

FIGURE 1. *DTA curve of* $CaSO_4 \cdot 2H_2O$ *with atmosphere of* N_2 *at 760 torr in the DTA cell.*

exothermic effects of the respective components (fig. 8), which indicates that this method can be used to identify the two forms in the presence of each other.

TABLE 2. *Peak and first-break temperatures of DTA curves of* α *and* β-$CaSO_4 \cdot 1/2H_2O$

Bulk pressure (torr)	Endotherm		Exotherm	
	T_{peak} [a] (°C)	T_{fb} [b] (°C)	T_{peak} [a] (°C)	T_{fb} [b] (°C)
α-$CaSO_4 \cdot 1/2H_2O$				
760	198	158	217	[c]
380	182	146	200	[c]
1	132	97	163	[c]
β-$CaSO_4 \cdot 1/2H_2O$				
760	195	155	375	322
1	132	94	375	324

[a] T_{peak} is the peak temperature.
[b] T_{fb} is the first-break temperature.
[c] Because the endothermic and exothermic curves overlap not possible to determine T_{fb} for exothermic curve.

3.2. Thermogravimetry

The thermogravigram of $CaSO_4 \cdot 2H_2O$ recorded using a heating rate of 3 °C/min and a temperature scale of 10 °C/inch is reproduced in figure 9. Although a two-step dehydration process was suggested by an apparent change in slope of the weight loss curve, indicated by the tangent lines in figure 9, a well defined inflection point attributed to the completion of the first dehydration process and the commencing of the second was not found (there was no indication of any plateau between the two reactions thus making it appear that they took place consecutively). The location of this point in the weight-loss curve was estimated by dropping a tangent line to the most straight portions of the segments associated with the two dehydration reactions and taking as the inflection point the intersection of the two lines, as shown in figure 9. The estimated inflection point corresponds to the removal of 65 percent of the water content of $CaSO_4 \cdot 2H_2O$ compared to the theoretical value of 75 percent (assuming that $CaSO_4 \cdot 1/2H_2O$ is formed).

One TG run was terminated at a weight-loss value equalling the removal of 1 1/2 molecules of H_2O from $CaSO_4 \cdot 2H_2O$, thus, theoretically producing either pure α- or β-$CaSO_4 \cdot 1/2H_2O$. The DTA curves of the product, however, indicated that together with β-$CaSO_4 \cdot 1/2H_2O$ about 5 percent of unchanged $CaSO_4 \cdot 2H_2O$ and γ-$CaSO_4$ was present. These results were confirmed by x-ray powder diffraction analysis.

The TG curves of α- and β-$CaSO_4 \cdot 1/2H_2O$ were identical when using the same heating rates and the curve of the β-form, recorded using a heating rate of

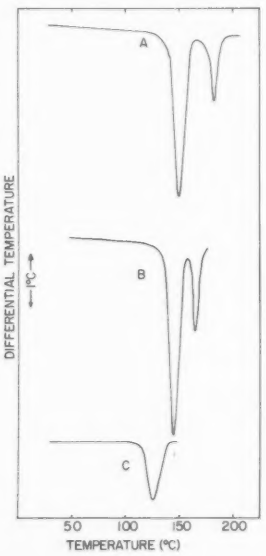

FIGURE 2. *Differential thermograms of* $CaSO_4 \cdot 2H_2O$ *at reduced pressures in the DTA cell.*

The pressures with thermograms A, B, and C were 590, 380, and ca. 1 torr, respectively.

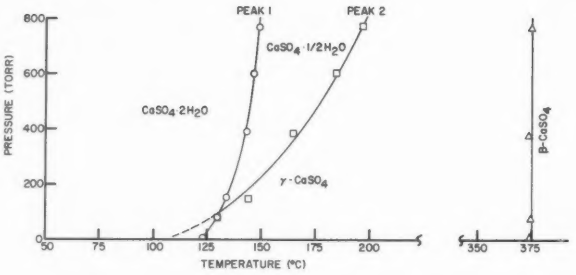

FIGURE 3. *Phase diagram for* $CaSO_4 \cdot 2H_2O$.

Gaseous pressure in the DTA cell plotted versus the peak temperatures of the endothermic and exothermic effects.

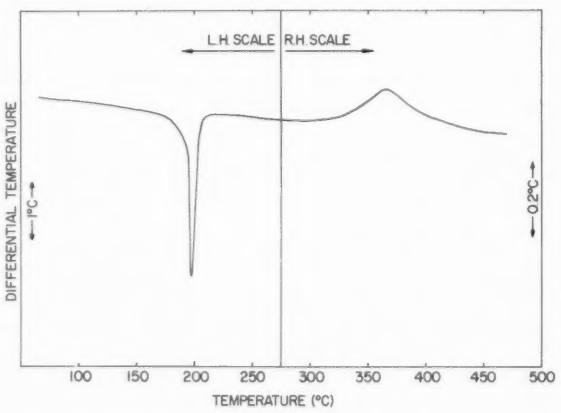

FIGURE 4. *DTA curve of* β-$CaSO_4 \cdot 1/2H_2O$ *with* N_2 *at 760 torr in the DTA cell.*

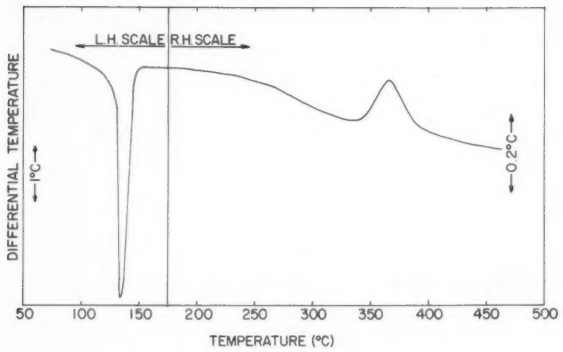

FIGURE 5. *DTA curve of β-$CaSO_4 \cdot 1/2H_2O$ with a residual pressure of ca. 1 torr in the DTA cell.*

12 °C/min and a temperature scale of 50 °C/in, is shown in figure 10. Well-defined incipient temperatures were not observed, i.e., the dehydration processes appeared to have commenced at the start of the runs, which was at 22 °C.

The endothermic effects in the differential thermograms of $CaSO_4 \cdot 2H_2O$ and the $CaSO_4 \cdot 1/2H_2O$ set, at 760 torr, were found at higher temperatures than the weight-loss processes observed in their respective thermogravigrams (compare figs 1 and 9 and figs. 4 and 10), although these two phenomena are associated with the same dehydration reactions. These apparent discrepancies are probably due to both differences in the heating rates used in the respective studies and to physical differences in the TG and DTA cells in such components as sample holders, heating units and location of thermocouples. The size and shape of the sample holders can have a pronounced effect on the temperature location of weight-loss curves and the endothermic peaks because of their differences in heat capacities.

3.3 Differential Scanning Calorimetry

The DSC curve of $CaSO_4 \cdot 2H_2O$ is reproduced in figure 11. A heating rate of 5 °C/min was used. Only

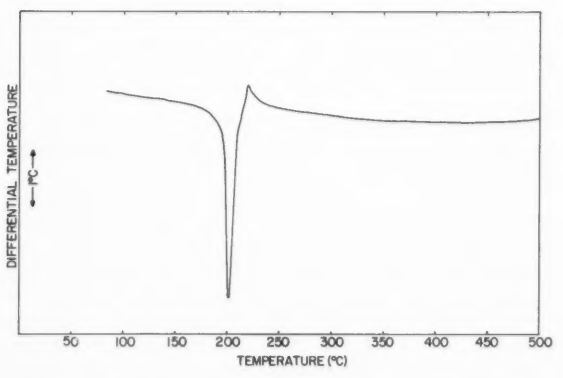

FIGURE 6. *DTA curve of α-$CaSO_4 \cdot 1/2H_2O$ with N_2 at 760 torr in the DTA cell.*

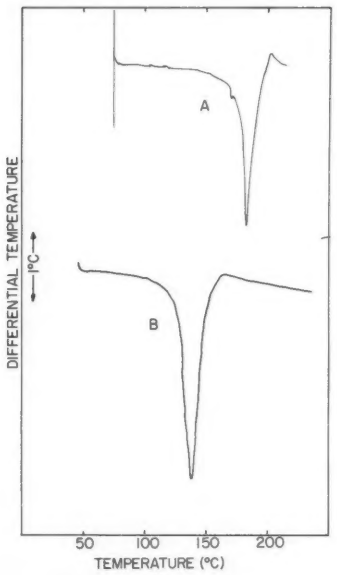

FIGURE 7. *Differential thermograms of α-$CaSO_4 \cdot 1/2H_2O$ with reduced pressures in the DTA cell.*

Pressures were 380 and ca. 1 torr, respectively, for thermograms A and B.

a single endothermic effect was measured because thermal equilibrium was not attained between the reference and sample cells after the first dehydration step was complete and before the second dehydration step had commenced. When normal sample crucibles, which had loosely fitting covers, were used, the resulting curves were very broad, virtually merging into the base line. Sharper curves (fig. 11) were obtained using hermetically sealed crucibles. The change in the base line before and after the observed dehydration reaction is attributed to a difference in the heat capacities between $CaSO_4 \cdot 2H_2O$ and the decomposition products.

The DSC curves of α- and β-$CaSO_4 \cdot 1/2H_2O$ were

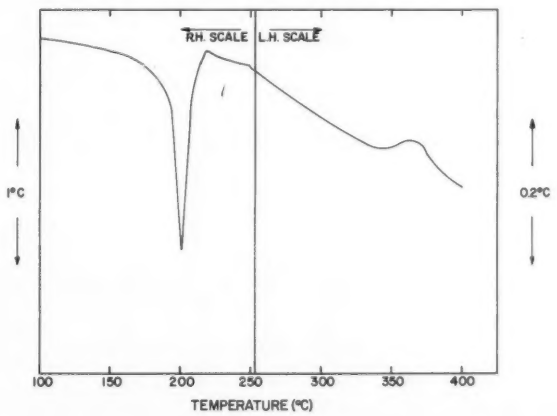

FIGURE 8. *DTA curve of an equal molar mixture of α and β-$CaSO_4 \cdot 1/2H_2O$ at 760 torr.*

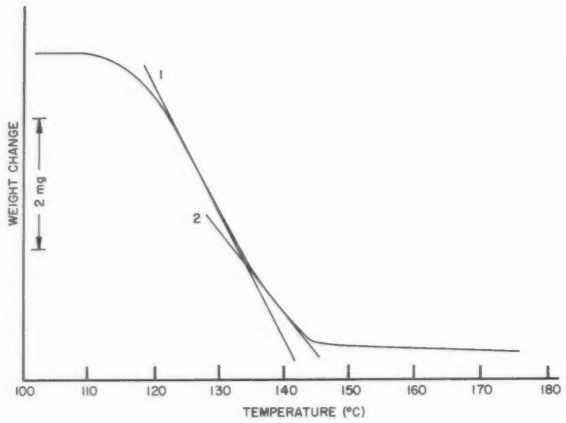

FIGURE 9. *TG curve of* $CaSO_4 \cdot 2H_2O$.

Line 1 is drawn tangent to the portion of the curve corresponding to the dehydration of $CaSO_4 \cdot 2H_2O$ to β-$CaSO_4 \cdot 1/2H_2O$ while tangent line 2 indicates the dehydration of β-$CaSO_4 \cdot 1/2H_2O$ to γ-$CaSO_4$.

essentially identical as both were very broad even when hermetically sealed crucibles were used.

4. Discussion

4.1. Thermal Dissociation of $CaSO_4 \cdot 2H_2O$

The thermal dissociation of $CaSO_4 \cdot 2H_2O$ in the region of 25 to 500 °C was monitored by both differential thermal analysis and thermal gravimetric analysis techniques and the pertinent features of the thermograms will be discussed in this section.

The differential thermogram of $CaSO_4 \cdot 2H_2O$ under a nitrogen atmosphere of 760 torr, fig. 1, is similar to thermograms observed by other investigators [3–7]. In the present study, however, the extent of overlapping of the first and second endothermic curves is smaller than previously reported, possibly because of our use

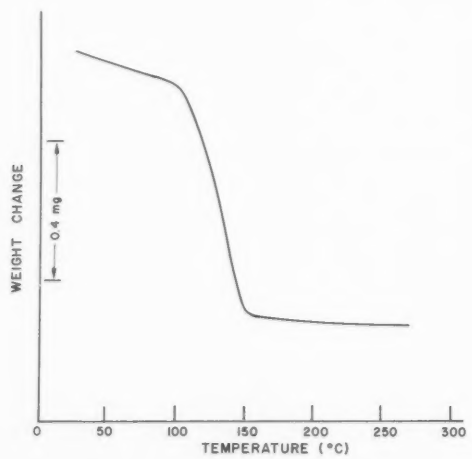

FIGURE 10. *The TG curve of* β-$CaSO_4 \cdot 1/2H_2O$.

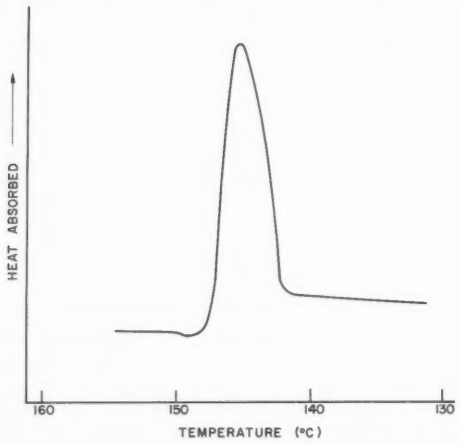

FIGURE 11. *The DSC curve of* $CaSO_4 \cdot 2H_2O$.

of micro samples. Furthermore, a small endothermic dent reported by some investigators, [19], to be located just after the second endothermic effect was not observed in the present study. This small effect has been attributed to the expulsion of small amounts of residual water from the hemihydrate [19]; alternatively, this endothermic peak could denote the presence of a small impurity.

The differential thermogram of $CaSO_4 \cdot 2H_2O$, reproduced in figure 1, can be understood on the basis of three transformations have peak temperatures of 150, 197, and 375 °C at 760 torr:

$$(1)\ CaSO_4 \cdot 2H_2O_{(s)} \underset{\longleftarrow}{\overset{150\ °C}{\longrightarrow}} \beta\text{-}CaSO_4 \cdot 1/2H_2O_{(s)} + 3/2H_2O_{(v)}$$

$$(2)\ \beta\text{-}CaSO_4 \cdot 1/2H_2O_{(s)} \underset{\longleftarrow}{\overset{197\ °C}{\longrightarrow}} \gamma\text{-}CaSO_{4(s)} + 1/2H_2O_{(v)}$$

$$(3)\ \gamma\text{-}CaSO_{4(s)} \xrightarrow{375\ °C} \beta\text{-}CaSO_{4(s)}$$

T_{fb} of reactions (1) and (3) were 126 and 325 °C, respectively. However, T_{fb} of reaction (2) could not be determined because the two endothermic effects overlapped. This phenomenon will later be discussed in more detail.

According to this scheme, reactions (1) and (2) are dehydration processes and, consequently, give rise to endothermic curves, while reaction (3) is attributed to a lattice modification from a hexagonal to an orthorhombic unit cell [2] and gives rise to an exotherm. It is felt that the formulation of a two-step dehydration process, reactions (1) and (2), was supported by the apparent change in the slope of the weight-loss curve of $CaSO_4 \cdot 2H_2O$ (fig. 9). As previously mentioned, the endothermic effects in the differential thermograms takes place at higher temperatures than the corresponding weight-loss curves because of differences in the DTA and TG modules and the use of different

heating rates in the respective studies.

The solid product formed in reaction (1) is presumed to be β-$CaSO_4 \cdot 1/2H_2O$ since the DTA curves associated with reactions (2) and (3) are identical to those observed for authentic β-$CaSO_4 \cdot 1/2H_2O$ (fig. 4).

The proposed scheme for the dehydration of $CaSO_4 \cdot 2H_2O$ assumes reaction (1) is completed as reaction (2) commences. This assumption cannot be substantiated by the DTA study alone because the two endothermic effects overlap and it is not possible to ascertain when the reaction responsible for the first effect terminates and the next reaction commences. The temperature at the end of an endothermic of exothermic effect does not necessarily coincide with the completion of the chemical reaction due to such factors as heat transfer and differences in the heat capacities of the reactant and products. In this matter, the TG studies are of assistance. As reported in Section 3.2, a TG run was terminated at a weight-loss value equalling the removal of 1 1/2 molecules of H_2O from $CaSO_4 \cdot 2H_2O$. The product was largely β-$CaSO_4 \cdot 1/2H_2O$ but did contain some 5 percent of unchanged $CaSO_4 \cdot 2H_2O$ and γ-$CaSO_4$. The phase types present were determined by DTA and x-ray powder diffraction techniques. A similar impure product was obtained when the stoichiometric amount of H_2O was removed, *in vacuo*, from $CaSO_4 \cdot 2H_2O$ to form β-$CaSO_4 \cdot 1/2H_2O$. Therefore, it is likely that with the nonuniformity fo heating conditions of DTA, reactions (1) and (2) can proceed to a small extent concurrently within a sample, especially, when the supply of $CaSO_4 \cdot 2H_2O$ is nearly depleted, and that the proposed reaction scheme is somewhat over simplified.

Further evidence for the overlapping of the two endothermic reactions is provided by the thermogravigram of $CaSO_4 \cdot 2H_2O$ reproduced in figure 9. Neither a well-defined inflection point denoting the completion of one reaction and the start of the other dehydration process nor a plateau in the weight-loss curve signifying a separation of the two reactions was observed in the thermogravigram. Furthermore, the change in slope between the two segments of the weight-loss curve associated with the two dehydration reactions was small. In the following, an interpretation to account for the observations is proposed. Possibly very little lattice rearrangement takes place when passing from $CaSO_4 \cdot 2H_2O$ to β-$CaSO_4 \cdot 1/2H_2O$ as only lattice water is being removed and the layer structure [20] of the Ca^{2+} and SO_4^{2-} grouping should retain its integrity. If this describes the actual situation, then it is reasonable to expect similar dehydration mechanisms for both $CaSO_4 \cdot 2H_2O$ and β-$CaSO_4 \cdot 1/2H_2O$.

The following will focus upon the interesting perturbations noted in the differential thermograms of $CaSO_4 \cdot 2H_2O$ when they were measured with reduced pressures in the DTA cell.

The influence of bulk atmospheric pressures on the values of T_{peak} and T_{fb} is given in table 1 and figure 2. T_{peak} of the first endothermic curve was decreased from 150 to 123 °C while T_{fb} decreased from 126 to 99 °C when the pressure was reduced from 760 torr to ca. 1 torr. T_{peak} of the second endothermic curve was decreased even more, being 197 °C at 760 torr and either merged into the first curve or vanished when the residual pressure was reduced to ca. 1 torr. The position of the small exothermic curve was not pressure dependent. Of particular interest to the present study is the mechanism proposed by several investigators [21, 22], based on other types of dehydration experiments on $CaSO_4 \cdot 2H_2O$. According to their mechanism, two dehydration reactions do take place if $CaSO_4 \cdot 2H_2O$ is in contact with appreciable amounts of water vapor. Dehydration *in vacuo*, however, leads directly to the formation of γ-$CaSO_4$ without β-$CaSO_4 \cdot 1/2H_2O$ being an intermediate specie. Removal of 1 1/2 molecules of H_2O from $CaSO_4 \cdot 2H_2O$ *in vacuo*, therefore, should result in a product which is a mixture of $CaSO_4 \cdot 2H_2O$ and γ-$CaSO_4$ and possibly containing a trace of β-$CaSO_4 \cdot 1/2H_2O$. The above views are untenable, however, for in the present study it was found that β-$CaSO_4 \cdot 1/2H_2O$ was the main product formed by the removal of H_2O *in vacuo* and only about 5 percent of $CaSO_4 \cdot 2H_2O$ and γ-$CaSO_4$ was found.

A reasonable explanation of the formation of β-$CaSO_4 \cdot 1/2H_2O$ by dehydration *in vacuo* of $CaSO_4 \cdot 2H_2O$ is embodied in the phase diagram shown in figure 3. The gaseous pressures within the DTA cell were plotted versus the peak temperatures for the dehydration reactions of $CaSO_4 \cdot 2H_2O$ and the subsequent transformation of γ-$CaSO_4$ to β-$CaSO_4$. According to this scheme the second endothermic curve does vanish rather than merging with the first endothermic curve. The formation of β-$CaSO_4 \cdot 1/2H_2O$ by the dehydration *in vacuo* of $CaSO_4 \cdot 2H_2O$ is accounted for by the metastable prolongation (indicated by the dot-dash line) of the univariant curve.

The merging tendency of the two endothermic curves can be explained on the basis of the van't Hoff equation:

$$\frac{d \ln K_p}{dT} = \frac{\Delta H}{RT^2}.$$

The gaseous pressures are low in the present case and ideal gas behavior is assumed.

In the above equation ΔH is the heat of reaction at temperature T, and therefore is not a constant. The standard heat of reaction, ΔH_0, at T_0 is introduced by using the Kirchoff equation:

$$\left(\frac{\partial(\Delta H)}{\partial T}\right)_p = \Delta C_p$$

$$\text{thus } \Delta H = \Delta H_0 + \int_{T_0}^{T} \Delta C_p dT \approx \Delta H_0 + \Delta \bar{C}_p (T - T_0),$$

$$\text{therefore } \frac{d \ln K_p}{dT} = \frac{\Delta H_0 + \Delta \bar{C}_p (T - T_0)}{RT^2}$$

$$= \frac{\Delta H_0}{RT^2} + \frac{\Delta \bar{C}_p}{RT} - \frac{\Delta \bar{C}_p T_0}{RT^2}.$$

The integrated form of the above equation, when considering the interval between T_1 and T_2, becomes

$$\ln \frac{K_{p_2}}{K_{p_1}} = -\frac{\Delta H_0}{R}\left(\frac{1}{T_2}-\frac{1}{T_1}\right)+\frac{\Delta \bar{C}_p}{R}\ln\frac{T_2}{T_1} + \frac{\Delta \bar{C}_p T_0}{R}\left(\frac{1}{T_2}-\frac{1}{T_1}\right).$$

The last term vanishes at $T_0 = 0$ K, resulting in the following equation:

$$\ln \frac{K_{p_2}}{K_{p_1}} = -\frac{\Delta H_0}{R}\left(\frac{1}{T_2}-\frac{1}{T_1}\right)+\frac{\Delta \bar{C}_p}{R}\ln\frac{T_2}{T_1}.$$

The pressure decrease necessary to shift T_{peak} of the second endothermic curve in the thermogram of $CaSO_4 \cdot 2H_2O$ from 197 to 123 °C can now be estimated by setting $T = T_{peak}$ and $K_p = p^{1/2}$ and using the values of ΔH_0 and ΔC_p reported by Kelly, Southard, and Anderson [9] for the reaction β-$CaSO_4 \cdot 1/2H_2O_{(s)} \leftrightarrows \gamma$-$CaSO_{4(s)} + 1/2H_2O_{(v)}$. The calculated value $P_2/P_1 = 0.06$ suggests that a 16 fold decrease in the partial pressure of water vapor within the specimen tube can account for the shift in T_{peak} observed when the bulk atmospheric pressure is decreased from 760 torr to ca. 1 torr. By a similar method, with $K_p = P^{3/2}$, a value of $P_2/P_1 = 0.36$ was calculated for the case when T_{peak} of the first endothermic effect was decreased from 150 to 123 °C. These values can be only considered as approximations to the actual situations because of the nonrigorous treatment.

4.2. Thermal Analysis of α- and β-$CaSO_4 \cdot 1/2H_2O$

In the following discussion, the differential thermograms and the thermogravigrams of α- and β-$CaSO_4 \cdot 1/2H_2O$, measured from 25 to 500 °C, will be analyzed

The differential thermograms will be discussed in detail since it has been reported [15] that the two forms of $CaSO_4 \cdot 1/2H_2O$ can be identified by their thermograms. The thermograms of the α and β forms measured under an atmospheric pressure of 760 torr are shown in figures 6 and 4, respectively. Each thermogram consisted of a single endothermic and a smaller exothermic curve. Budnikov and Kosyreva have reported [16] that a difference of about 20 °C was found between the T_{peak} of the endothermic effects in α- and β-$CaSO_4 \cdot 1/2H_2O$. A difference of only 3 °C (table 2) between the respective values of T_{peak} as well as T_{fb}, however, was measured in the present study. This small ΔT can possibly be attributed to porosity differences in the α and β forms. The only essential difference between the thermograms are in the exothermic effects. The exothermic effect of α-$CaSO_4 \cdot 1/2H_2O$ closely follows the endothermic effect and has a T_{peak} of 217 °C, while the exothermic effect of β-$CaSO_4 \cdot 1/2H_2O$ is much broader and has a T_{peak} of 375 °C and T_{fb} of 322 °C. Both exothermic effects have been attributed to phase changes [15].

The values of T_{peak} and T_{fb} for the endothermic effects of α and β-$CaSO_4 \cdot 1/2H_2O$ have a similar pressure dependence (table 2 and fig. 5 and 7) as the second endothermic effect of $CaSO_4 \cdot 2H_2O$ and can be interpreted in the same manner.

The location of the exothermic effect observed in the thermogram of α-$CaSO_4 \cdot 1/2H_2O$ was pressure sensitive in the same manner as the preceding endothermic effect (table 2 and fig. 7). Possibly this exothermic effect can be attributed to the formation of a new phase, the conversion being triggered by the removal of the lattice water. Because this apparent phase conversion took place immediately after the dehydration reaction, it is reasonable to expect the location of the exothermic effect would shift in the same direction as the endothermic effect. In contrast, the location of the exothermic effect of β-$CaSO_4 \cdot 1/2H_2O$ was not significantly pressure dependent.

The difference observed in the exothermic effects of the thermograms of α and β-$CaSO_4 \cdot 1/2H_2O$ do not necessarily indicate a structural difference between the two forms, but possibly are associated with the dehydration kinetics. The kinetics can depend upon such factors as the surface area, porosity and crystallinity. The β form is produced by dry decomposition which should yield a poorly crystalline and porous material with a larger surface area than the α form, which was a precipitated material and, therefore, should consist of well-formed crystals.

The thermogravigrams of α- and β-$CaSO_4 \cdot 1/2H_2O$ were so similar that it was impossible to differentiate between the two forms on the basis of TG studies. The thermogravigram of β-$CaSO_4 \cdot 1/2H_2O$ is reproduced in figure 10. Note that the dehydration reaction appeared to be initiated at room temperature. Probably, the loosely held zeolitic water of β-$CaSO_4 \cdot 1/2H_2O$ [18] is first removed then followed by dissociation of the lattice water. The removal of lattice water is indicated by the more pronounced sloping segment of the weight-loss curve.

4.3. Calorimetry Studies

On the assumption that the endothermic effect measured in the DSC curve of $CaSO_4 \cdot 2H_2O$ (fig 11) could be entirely attributed to the first dehydration step of $CaSO_4 \cdot 2H_2O$, the heat of reaction of

$$CaSO_4 \cdot 2H_2O_{(s)} \rightleftarrows CaSO_4 \cdot 1/2H_2O_{(s)} + 3/2H_2O_{(v)}$$

was estimated to be 23.8 kcal (9.96×10^4 J) per gram mol. wt. This value is substantially higher than the calculated value of 19.9 kcal (8.33×10^4 J) per gram mol. wt., obtained using the equation given by Kelly, Southard, and Anderson [9]. A reasonable explanation for this discrepancy has previously been discussed in section 4.1 for the cases of the thermogravigram and the differential thermogram of $CaSO_4 \cdot 2H_2O$, i.e., the two dehydration steps involved in the complete dehydration of $CaSO_4 \cdot 2H_2O$ are to some extent taking place concurrently during the DSC measurements.

The endothermic curves for α- and β-$CaSO_4 \cdot 1/2H_2O$ were too broad to permit the calculation of the heat of reactions.

5. Summary and Conclusions

The dehydration of $CaSO_4 \cdot 2H_2O$ to γ-$CaSO_4$ is a two-step dissociative process, with β-$CaSO_4 \cdot 1/2H_2O$ being the intermediate product, irrespective of the dehydration methods.

The differential thermogram of $CaSO_4 \cdot 2H_2O$, measured under gaseous pressures of a 760 torr, has two large endothermic effects with peak temperatures of 150(T_{fb} of 126 °C) and 197 °C and a smaller exotherm with peak temperature of 375 °C (T_{fb} of 325 °C) The endothermic effects were associated with dehydration processes whereas the exothermic effect indicated phase transformation of γ-$CaSO_4$ to β-$CaSO_4$. When the dissociative reactions were carried out under reduced pressure the endothermic effects shifted to lower temperatures and tended to merge. With residual pressures of about 1 torr, a single endothermic effect was observed. These phenomena can be explained from the application of the van't Hoff equation and on the basis of a phase diagram constructed by plotting gaseous pressures in the DTA cell versus peak temperatures. Location of the exothermic effect was not significantly pressure dependent.

The small change in slope observed between the two segments of the weight-loss curve of $CaSO_4 \cdot 2H_2O$ indicates that there is little difference in the dissociative mechanisms of the two dehydration reactions.

While it was not possible to differentiate between the supposed α and β forms of $CaSO_4 \cdot 1/2H_2O$ on the basis of TG and DSC studies, the differential thermograms of the two forms were somewhat dissimilar. An endothermic effect with a peak temperature of ca. 197 °C and T_{fb} of ca. 158 °C, was found in the differential thermograms of both forms of $CaSO_4 \cdot 1/2H_2O$. The α form had a single exothermic effect with a peak temperature of 217 °C, while the exotherm of the β form had a peak temperature of 375 °C, T_{fb} of 322 °C, under bulk pressures of 760 torr. The peak temperature of the exothermic effect of α-$CaSO_4 \cdot 1/2H_2O$ was pressure dependent, whereas, the exothermic effect of β-$CaSO_4 \cdot 1/2H_2O$ was not influenced by changes in the atmospheric pressure within the DTA cell. The differences in the thermograms could possibly be associated with the dehydration kinetics, because the α form should have a more perfect crystalline structure than the β form. Therefore, while slight differences have been observed between the properties of α- and β-$CaSO_4 \cdot 1/2H_2O$, at the present it cannot be conclusively determined if these differences are sufficiently significant to consider the supposed α and β forms as separate entities.

The author thanks Max Tryon, I. Flynn, and E. Parks for experimental assistance.

6. References

[1] Clifton, J. R., Nature, **232**, 125 (1971).
[2] Gay, P., Min. Mag. **35**, 270 (1965).
[3] Volzhenskii, A. V., Keramiba **11**, 64, (1939).
[4] Gruver, R. M., J. Am. Ceram. Soc. **34**, 353, (1951).
[5] West, R. R., and Sutton, W. J., J. Am. Ceram. Soc. **37**, 221, (1954).
[6] Fleck, W. E. P., Jones, M. H., Kuntze, R. A., and McAdie, H. G., Can. J. Chem. **38**, 936, (1960).
[7] Holdridge, D. A., and Walker, E. G., Trans. British Ceramic Soc., **66**, 485, (1967).
[8] Richards, K. J., Ph.D. Thesis, University of Utah, 1962. Microfilm 63–1387, University Microfilms, Ann Arbor, Michigan.
[9] Kelley, K. K., Southard, J. C., and Anderson, C. T., U.S. Bureau of Mines, Tech. Paper No. 625, (1941).
[10] Eipeltauer, E., Zement-Kalk Gips **11**, 264, (1958).
[11] Lambe, C. M., and Offutt, J. S., Am. Ceram. Soc. Bull. **33**, 272, (1954).
[12] Morris, R. J., Nature **198**, 1298, (1963).
[13] Gay, P., Min. Mag. **35**, 354, (1965).
[14] Flörke, O. W., Neues Jb. Miner. Mh. **84**, 198 (1952).
[15] Powell, D. A., Nature **182**, 792, (1958).
[16] Budnikov, P. O., and Kosyreva, Z. S., Voprosy Petrograf. i Minera Akad. Nauk S.S.S.R. **2**, 342, (1953) (Chem. Abstr. **48**, 13314a, (1954)).
[17] Weiser, H. B., and Milligan, W. O., J. Am. Chem. Soc. **59**, 1456, (1937).
[18] Saito, T., Bull. Chem. Soc. (Japan), **34**, 1454, (1961).
[19] Ramachandron, V. S., Applications of Differential Thermal Analysis in Cement Chemistry (Chemical Publishing Company, New York, New York, 1969).
[20] Wooster, W. A., Krist, Z., **94**, 375, (1936).
[21] van't Hoff, J. H., Hinrichsen, W., and Wegert, F., Sitzber. Akad. (Berlin) 570, (1901).
[22] Razouk, R. I., Salem, A. Sh., and Mikhai, R. Sh., J. Phys. Chem., **64**, 1350, (1960).

(Paper 76A1–697)

448-417 O - 72 - 4

JOURNAL OF RESEARCH of the National Bureau of Standards—A. Physics and Chemistry
Vol. 76A, No. 1, January–February 1972

Modulus of Natural Rubber Cross-Linked by Dicumyl Peroxide. I. Experimental Observations

Lawrence A. Wood

Institute for Materials Research, National Bureau of Standards, Washington, D.C. 20234

and

George W. Bullman and George E. Decker

Institute for Applied Technology, National Bureau of Standards, Washington, D.C. 20234

(October 6, 1971)

Natural rubber mixed with varying amounts of dicumyl peroxide was cross-linked by heating 120 min at 149 °C. The quantitative measure of cross-linking was taken as the amount *fp* of decomposed dicumyl peroxide, the product of *p*, the number of parts added per hundred of rubber and *f* the fraction decomposed during the time of cure. The shear creep modulus *G* was calculated from measurements of the indentation of a flat rubber sheet by a rigid sphere. The glass transition temperature T_g, was raised about 1.2 °C for each part of decomposed dicumyl peroxide. Above $(T_g + 12)$ the modulus-temperature relations were linear with a slope that increased with increasing cross-linking. The creep rate was negligible except near the glass transition and at low values of *fp*. Values of *G*, read from these plots at seven temperatures, were plotted as a function of *fp*. The linearity of the two plots permits the derivation of the general relation: $G = S(fp + B)T + H(fp + B) + A$ where *A*, *B*, *H*, and *S* are constants. The lines representing *G* as a function of *fp* at each temperature all intersected near the point, $fp = 0.45$ phr, $G = 2.70$ Mdyn cm^{-2} (0.270 MN m^{-2}). The constants were evaluated as $A = 2.70$ Mdyn cm^{-2}, $B = -0.45$ phr, $S = 5.925 \times 10^{-3}$ Mdyn cm^{-2}(phr)$^{-1}$K^{-1} and $H = 0.0684$ (Mdyn cm^{-2}) (phr)$^{-1}$. This equation represented satisfactorily all the data obtained at temperatures from −50 to +100 °C for values of *fp* from about 1 to 24 phr.

Key words: Creep; cross-linking; dicumyl peroxide; glass transition; indentation measurements; rubber, natural.

1. Introduction

Studies of the modulus of natural rubber are conveniently made by observing the indentation of a flat rubber sheet by a rigid sphere. In previous investigations [1, 2][1] in our laboratory we have studied the compliance (reciprocal of the modulus) as a function of time and temperature for pure-gum vulcanizates of natural and synthetic rubbers cross-linked by conventional sulfur-accelerator curing systems. In the present work similar studies were made for natural rubber which had been cross-linked by varying amounts of dicumyl peroxide. The results obtained with this system should be of fundamental significance, since the amount of cross-linking can be evaluated quantitatively and the cross-links are considered to be direct carbon-carbon bonds. Time effects have been found to be negligible over much of the ranges of temperature and cross-linking investigated [3, 4].

[1] Figures in brackets indicate the literature references at the end of this paper.

2. Decomposition of Dicumyl Peroxide

Peroxides have been recognized as cross-linking agents for rubber for more than fifty years. Recent work has been concentrated on dicumyl peroxide, which is particularly suitable because of favorable values of volatility and reaction rate at various temperatures. Used without any auxiliary materials it is especially convenient for fundamental studies.

The mechanism of cross-linking of elastomers by dicumyl peroxide has been extensively studied in recent years. The results are outlined in a comprehensive review by Loan [5]. The basic mechanism is particularly simple in the case of natural rubber. At elevated temperatures the peroxide splits, by a first-order reaction, into two free radicals each of which is neutralized by the removal of a hydrogen atom from the rubber. Carbon-carbon primary valence bonds between different rubber molecules are then formed at the sites from which the hydrogen atoms have been removed. In the absence of side reactions,

each peroxide molecule decomposed thus is responsible for the formation of one cross-link. The rate of the reaction is controlled by the rate of decomposition of the peroxide. The reaction products (other than the cross-linked rubber, of course) are α-α'-dimethyl benzyl alcohol, acetophenone, and methane. The methane would be expected to pass through the rubber and be lost at the temperature of vulcanization. Although this temperature is below the boiling points of the other two products, their vapor pressures at this temperature are quite high. Consequently it is expected that a considerable portion of them will be evaporated, with the residue remaining in the rubber. Since they are an alcohol and a ketone they would not be expected to swell the rubber or to dissolve in it to any appreciable extent.

The fraction f of molecules decomposed in a first-order reaction in a given time t can be shown to be such that

$$\log_{10}(1-f) = -0.3010(t/t_{1/2}) \qquad (1.1)$$

where $t_{1/2}$ is the half-life, the time required for half of the molecules to decompose. The equation shows that for increasing values of t, f is an increasing function of decreasing slope, rising from zero to reach a value of 0.95 at $t/t_{1/2}=4.3$. It approaches a value of unity at infinite time, of course.

The variation of a first-order reaction rate with temperature is most conveniently represented by a plot of log $t_{1/2}$ against $-T^{-1}$, the reciprocal of the temperature in kelvins, as in figure 1. This plot yields a straight line represented by

$$\log t_{1/2} = (\Delta H/2.30R)(T^{-1} - T_1^{-1}) \qquad (1.2)$$

where ΔH is the activation energy of the reaction, R the gas constant, and T_1 the value of the temperature at which $t_{1/2}=1$ min.

The observations represented in figure 1 were obtained by Hummel and co-workers [6], who measured the amount of unreacted dicumyl peroxide in natural rubber by chemical means after varying times at elevated temperatures. The results are well represented by the straight line shown, which has the equation

$$\log t_{1/2} = 7800\,T^{-1} - 17.040. \qquad (1.3)$$

This equation has a slope corresponding to an activation energy of 35.7 kcal mol^{-1} (149.4 kJ mol^{-1}), a reasonable value for the decomposition of a peroxide. The half-life calculated from eq (1.3) is several thousand years at 25°, about 5 days at 100°, and about 27.4 min at 149°. The reaction rate is influenced relatively little by the medium in which the decomposition takes place, unless the medium is acidic.

3. Experimental Arrangements

In the present work pale crepe natural rubber [2] was mixed with varying amounts of "recrystallized" dicumyl peroxide and cured for 120 min at 149 °C to form disk specimens about 35 mm in diameter and 9 mm in thickness. The amounts, p, of dicumyl peroxide added to each 100 parts by weight of rubber were 0, 0.5, 1, 2, 3, 4, 5, 7, 8, 10, 15, 20, and 25 parts respectively. Larger amounts of dicumyl peroxide yielded specimens which were too brittle for satisfactory handling. The results discussed in the preceding section would indicate that at 149 °C the half-life $t_{1/2}$ is about 27.4 min, as already stated. Consequently, from eq (1.1), at 120 min ($=4.38\ t_{1/2}$) about 95.2 percent of the dicumyl peroxide should have been decomposed, ($f=0.952$). The amounts of decomposed dicumyl peroxide fp are therefore calculated as 0, 0.48, 0.95, 1.90, 2.86, 3.81, 4.76, 6.66, 7.62, 9.52, 14.28, 19.0 and 23.8 phr respectively.

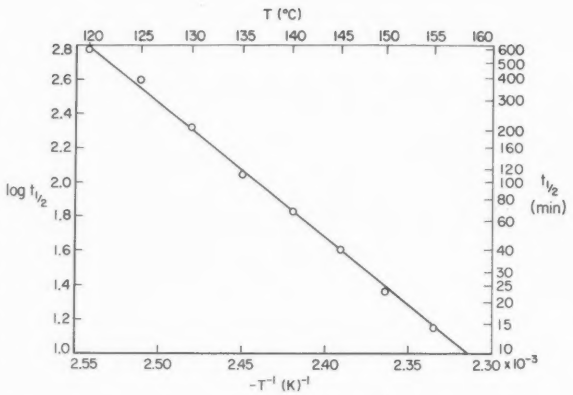

FIGURE 1. *Logarithm of the half-life of dicumyl peroxide (in minutes) as a function of the reciprocal of the temperature (in kelvins).*

Experimental points from data of Hummel, Scheele, and Hillmer [6] table 3, column 2. The slope of the straight line corresponds to a constant activation energy ΔH of 35.7 kcal (mol)$^{-1}$ (149.4 kJ (mol)$^{-1}$).

The shear creep modulus G (limit of the ratio of shear stress to strain at zero deformation) was calculated for each specimen from observations of the indentation of the flat rubber surface by a rigid sphere under constant load. Details of the operation of the instrument are given in two previous papers [1,2].

A linear transducer was used to measure the displacement of a ball indentor 2.50 mm in diameter as the load was increased from 30 to 580 g, in most of the present work, in accordance with the procedures described in ASTM Method D 1415–56T—International Hardness of Vulcanized Natural and Synethic Rubbers. For rubbers with a low modulus, measurements were made as the load was increased from 30 to 130 g. The indention values were never greater than the radius of the ball (1.25 mm).

A chamber surrounding the specimens was used to maintain any constant temperature in the range from −100 to +100 °C by the evaporation of liquid nitrogen. In order to avoid modulus changes arising from possible changes in crystallinity of the rubber, no observations (with two exceptions) were made between −30 and +20 °C, the region most favorable for crystalliza-

[2] NBS Standard Reference Material 385b Specific volume at 25°, 1.1074 cm^{3}g^{-1}.

tion. Observations were normally made over the range from 5 to 600 s after the application of the load.

4. Calculation of Compliance and Modulus

The penetration P of a rigid ball of radius R in contact with a plane rubber specimen of shear compliance J, when a force F is applied, is given by the Hertz equation [7, 8],

$$\frac{P}{R}=\left(\frac{3J}{16R^2}\right)^{2/3}F^{2/3} \tag{3.1}$$

when the ratio $\frac{P}{R}$ is sufficiently small (normally less than unity). When the load is increased from a value F_1 to a value F_2 the displacement ΔP of the indentor is

$$\left(\frac{\Delta P}{R}\right)=\left(\frac{3J}{16R^2}\right)^{2/3}(F_2^{2/3}-F_1^{2/3}). \tag{3.2}$$

This in turn gives

$$J=\frac{16R^2}{3[F_2^{2/3}-F_1^{2/3}]^{3/2}}\left(\frac{\Delta P}{R}\right)^{3/2}. \tag{3.3}$$

The shear modulus G can be calculated as equal to J^{-1}, since the creep rate is low or zero in all the significant portions of the present study.

For a load increase from 30 to 580 g on a 2.50 mm ball, the values of the compliance J in Mdyn^{-1} cm^2 (10 MN^{-1} m^2) and the modulus G in Mdyn cm^{-2} (0.1 MN m^{-2}) are:

$$J=0.1833(\Delta P/R)^{3/2} \tag{3.4a}$$

and

$$G=5.455(\Delta P/R)^{-3/2}. \tag{3.4b}$$

For a load increase from 30 to 130 g on a 2.50 mm ball the values of J in Mdyn^{-1} cm^2 and the modulus G in Mdyn cm^{-2} are:

$$J=1.327(\Delta P/R)^{3/2} \tag{3.5a}$$

and

$$G=0.7536(\Delta P/R)^{-3/2}. \tag{3.5b}$$

In the derivation of the Hertz equation an expansion in terms of a series of powers of P/R is followed by the neglect of all terms higher than the first. Consequently the validity of the equation is impaired when the penetration is large. Deviations can be detected experimentally when the ratio P/R is greater than 0.5[1, 9, 10], but were not considered large enough to be disturbing in the present work until P/R exceeded unity, near which point there is a significant change in the geometry of the system.

Equation (3.1) shows that if this condition is to be fulfilled, the 130 g load should not be used for specimens with J greater than about 0.66 Mdyn^{-1} cm^2, i.e., a modulus G less than 1.53 Mdyn cm^{-2}. Correspondingly the 580 g load should not be used for specimens with J greater than 0.147 Mdyn^{-1} cm^2, i.e., a modulus less than 6.83 Mdyn cm^{-2}. In the present work there were no specimens with a modulus less than 1.53 Mdyn cm^{-2}. The 130 g load was used for specimens with a modulus above this value. In view of the decreased sensitivity of the measurement with this load for specimens with a modulus above 6.83 Mdyn cm^{-2}, most of the work at all higher values utilized the 580 g load. Where both loads were used on the same specimen the values of the calculated modulus showed good agreement.

An empirical equation with slightly different values of the constant and the exponents has been developed by Scott [11] and used in connection with hardness measurements at higher penetrations. In common with other observers [10] we find that the difference between values obtained with the two equations is not sufficient to justify the use of Scott's equation over the range of penetrations we employed.

In our work it was found convenient to draw up a table showing values of $(\Delta P/R)^{3/2}$ for $\Delta P/R$ between 0 and 1. This facilitated the use of eq (3.4) and (3.5) to obtain values of J or G from experimental observations of the displacement ΔP.

When the ball is pressed against the rubber sheet, some portions of the rubber are stretched, while other portions are compressed. We assume that the deformations in both cases are less than 5 percent and therefore fall within the limits of an almost linear stress-strain relation. In other words the ratio of stress to strain over this range is constant within the limits of precision of the experiment. Thus the values calculated require no further extrapolation to the limit of zero deformation as required by the definitions of compliance and modulus.

The thickness of the specimens (9 mm) was sufficiently large so that corrections of the type described by Waters [12, 13] were not required.

5. Observations

The isochronal shear modulus G, measured 10 min after the application of the load, is plotted as a function of temperature T in figure 2 for the lower values of fp, and straight lines are drawn to represent these values. Near the lowest temperatures a decrease of temperature causes a drastic increase of modulus. This effect is caused by an approach to the glass transition temperature and will be discussed in a later section of this paper. With the exception of that section, the present paper will concentrate attention on the modulus above these temperatures.

Where the values of G at 5 s differ from those found at 10 min, they are plotted as separate points (downward-pointing V's), except for temperatures below −50° (where the 5 s values are omitted to avoid confusion). It is seen that creep can be observed at the lowest temperatures in all cases, and at all temperatures when fp is small. The reliability of the observations for the specimens containing no dicumyl peroxide ($fp=0$) was somewhat doubtful. Consequently in this case only the observations at the lowest temperatures

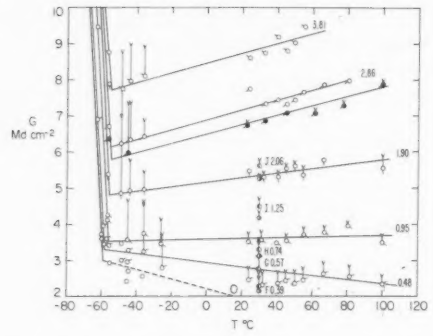

FIGURE 2. *Shear modulus (Mdyn cm⁻² or 0.1 MNm⁻²) as a function of temperature.*

Numbers on graphs give numbers of parts of decomposed dicumyl peroxide per hundred of rubber.
○ Open circles, 10-min moduli.
● Dark circles, 10-min moduli. Second cure.
◐ Left-shaded circles, 10-min moduli obtained from observations of Chasset and Thirion [17]. Specimens F, G, H, I, and J.
◑ Right-shaded circles, 10-min moduli obtained from observations of Plazek [20]. Specimens F, H, I, and J.
V Downward-pointing V's indicate 5-s moduli where different from 10-min values.

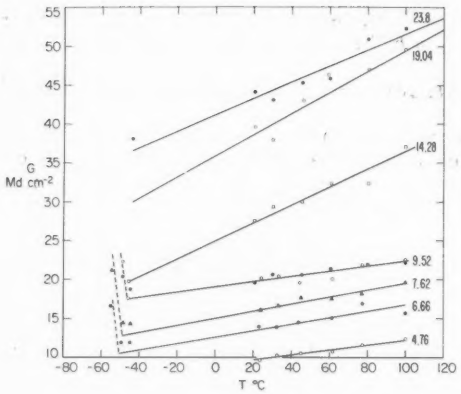

FIGURE 3. *Shear modulus (Mdyn cm⁻² or 0.1 MNm⁻²) as a function of temperature.*

Numbers on graphs give numbers of parts of decomposed dicumyl peroxide per hundred of rubber.

are plotted. The straight line for $fp = 0$ has been drawn to pass through the value 1.88 Mdyn cm^{-2} at 25 °C in conformity with an extrapolation mentioned later in this paper.

The observations shown in figure 2 have already been reported at the 1968 Kuala Lumpur International Rubber Conference in a paper [3] devoted to a discussion of the creep of natural rubber vulcanizates. The conclusion of the paper was that, for temperatures 40° or more above the glass transition temperature, the creep rate at times greater than 5 s decreased with increasing cross-linking, reaching a value of the order of 0.5 percent per decade for vulcanizates cured with 2.86 parts of decomposed dicumyl peroxide.

The sensitivity of the present experimental arrangement was not sufficient to permit measurement of lower values of creep over a 2-decade range of time. For vulcanizates cured with larger amounts—from 3.81 to 23.8 parts—the indentation at 10 min was the same as that at 5 s, except near the glass transition.

In later work [4] involving strips of rubber stretched to an elongation of 25-100 percent, observations extending over 4 decades of time beyond 30 s showed that the creep rate at room temperature was about 0.5 percent per decade for rubber cross-linked with 2.86 phr of decomposed dicumyl peroxide, decreased to about 0.2 percent per decade for 3.81 phr, and became less than 0.03 percent per decade for 4.76 phr or larger amounts.

In the remainder of the present paper little weight will be given to observations where the creep was appreciable, and the remaining conclusions will be based on observations where the creep between 5 s and 10 min was less than the uncertainty of measurement.

Figure 3 shows the shear modulus G as a function of temperature for the higher values of fp. For all the observations in figure 3, there was no measurable creep.

It will be noted that the data in figure 3 show much greater scatter for the three values of fp greater than 10. However, in figure 3 and in figures shown later there is no systematic trend differing from the behavior shown for lower values of fp. It might well be desirable in future work to investigate this region more carefully.

In the remainder of the present paper it will be assumed that the straight lines in figures 2 and 3 give an adequate representation of the modulus data, and the conclusions will be based on the lines themselves, rather than on the individual points determining the lines.

6. Glass Transition Temperatures

At low temperatures, figures 2 and 3 show a sudden change of the usually positive slope of the isochronal G, T curves to large negative values. The temperature at which this discontinuity of slope occurs is about −58° for the rubber containing no dicumyl peroxide and increases with increasing values of fp.

This effect, first noted in the stress-temperature relations by Meyer and Ferri [14], and later studied by Witte and Anthony [15] is related to the glass transition. Its exact location depends on the duration of application of the stress, lower values being obtained for longer times. For the 10-min moduli measured here T_d the temperature of the discontinuity is about 12° above the glass transition temperature T_g, as normally measured by volume-temperature relations.

Figure 4 shows a plot of the glass transition temperature T_g (calculated as 12° lower than the temperature of the discontinuity) for comparison with values determined directly from volume-temperature relations as reported by Mason [16]. Comparison is also made with values of T_g calculated as 2° lower than T_a, the temperature at which the product of the 1-minute compliance and the temperature T (in kelvins) first reaches the value 0.5 Mdyn^{-1} cm^2 (K) as the temperature is increased from very low values. The latter quantity has

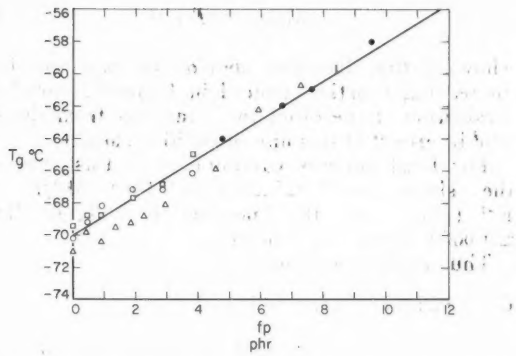

FIGURE 4. *Glass transition temperature as a function of decomposed dicumyl peroxide content.*

○ Read from figure 2 on assumption that $T_g = T_d - 12$ where T_d is the temperature of the quasi-discontinuity in the modulus-temperature relation.
● Read from a plot similar to figures 2 and 3 on assumption that $T_g = T_d - 12$.
□ Calculated as $T_g = T_a - 2$ where T_a is the temperature at which the product of the 1-min compliance J and the temperature T in kelvins first reaches the value 0.5 $Mdyn^{-1}$ cm^2 (K) as the temperature is increased from very low values.
△ Values reported by Mason [16] from direct observations of the volume-temperature relation.

The straight line represents the equation $T_g = -70 + 1.2fp$.

been used to obtain an approximation of T_g in previous work [3, 4]. The values of T_g appear to be in satisfactory agreement and show a linear increase with cross-linking as measured by fp, the amount of decomposed dicumyl peroxide. The glass transition temperature increases at the rate of about 1.2° for each part of dicumyl peroxide decomposed per 100 parts of rubber. The value of f, the fraction decomposed, was calculated from eqs (1.1) and (1.2). In the present work its value, as already indicated, was 0.952, while in the work of Mason, whose vulcanizates were cured 1 h at 140 °C, the value was calculated as 0.455.

7. Calculated Results

In order to determine how the modulus at a given temperature varies with cross-linking, the values of the 10-min modulus G were read from the straight lines in figures 2 and 3 at 7 temperatures: −50, −25, 0, 25, 50, 75, and 100 °C. The values found are given in table 1.

Figure 5 shows a plot for the 25° modulus as a function of the quantity fp. The experimental points are well represented by a linear relation. The slope $\partial G/\partial fp$ and intercept G_0 were determined by the method of least squares, without using any values obtained from the specimen containing no dicumyl peroxide ($fp = 0$). Similar plots were also made for the other temperatures. The results are given in table 2, together with the standard deviations of each quantity as obtained from the least squares computation.

Figure 6 shows a plot of the slope $\partial G/\partial fp$ as a function of T. The experimental points are those given for $\partial G/\partial fp$ in table 2, and the straight line in figure 6 represents a least squares fit to the points of figure 6. The relationship appears to be linear within the precision of the observations.

The linearity of the relationships plotted in figures 2, 3, 5, and 6 permits one to derive by integration a simple expression representing G as a function of T and fp. It is

$$G = S(fp + B)T + H(fp + B) + A \qquad (6.1)$$

where A, B, H, and S are constants and T is expressed in kelvins. We shall find it more convenient to deal with temperatures in kelvins in the remainder of this paper. One can readily note from an examination of this equation that it predicts linearity in the relationships plotted in figures 2, 3, 5, and 6.

The lines represented by the observed slopes and intercepts given in table 2 for the 7 temperatures were now plotted on a graph (not reproduced here) showing G as a function of fp on a greatly expanded scale in the region from $fp = 0$ to $fp = 1$. It was found that they all intersected near the point where $fp = 0.45$ and $G = 2.70$ Mdyn cm^{-2}. This was verified by using the slopes and intercepts in table 1 to calculate at each temperature the value of G at $fp = 0.45$. The results,

TABLE 1. *Modulus as a function of cross-linking and temperature*

	Temperature °C						
fp phr	−50	−25	0	25	50	75	100
0	(2.87)	(2.54)	(2.21)	(1.88)	.....	.....	.....
0.48	3.20	3.06	2.92	2.77	2.63	2.49	2.35
.95	3.54	3.57	3.59	3.62	3.65	3.67	3.70
1.90	4.85	5.01	5.16	5.32	5.47	5.63	5.78
2.86	6.24	6.57	6.91	7.24	7.57	7.91	8.24
3.81	7.80	8.14	8.47	8.81	9.15	9.49	9.82
4.76	7.60	8.37	9.14	9.91	10.68	11.45	12.22
6.66	10.60	11.61	12.62	13.62	14.63	15.64	16.65
7.62	12.80	13.92	15.04	16.17	17.29	18.41	19.53
9.52	17.30	18.20	19.00	19.90	20.80	21.60	22.50
14.3	19.20	22.09	24.97	27.86	30.75	33.64	36.52
19.0	29.15	32.53	35.91	39.30	42.68	46.06	49.45
23.8	35.90	38.50	41.10	43.70	46.30	48.90	51.50

Modulus values are given in Megadynes per square centimeter (1 Mdyn $cm^{-2} = 0.1$ MN m^{-2}).

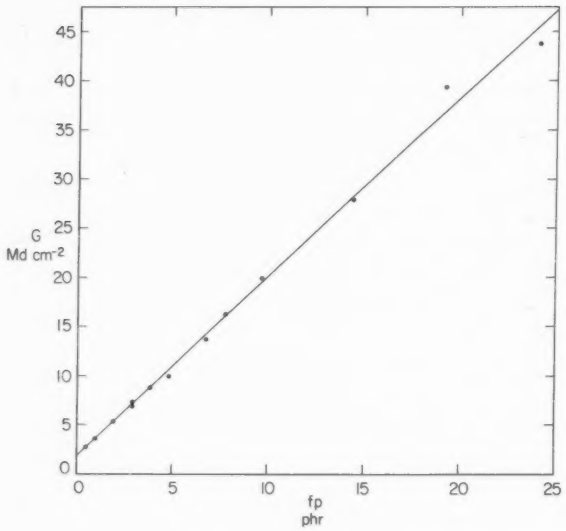

FIGURE 5. *Modulus at 25° C as a function of decomposed dicumyl peroxide content.*

Experimental points show values read from the straight lines in figures 2 and 3 at 25 °C. The straight line represents the function $G = 1.836\ fp + 1.88$ obtained from eq (6.3) at 25 °C.

which are given in the sixth column of table 2 approximate 2.70 Mdyn cm^{-2} and show no systematic variation with temperature.

This observation that all 7 of the lines like the one in figure 5, but for different temperatures, pass through a single point permits the evaluation of two of the constants. If the coordinates found for this point are inserted in eq (6.1) we have:

$$(0.45+B)ST+(0.45+B)H+A=2.70.$$

This equation can be valid at all temperatures if and only if

$$B=-0.45 \text{ phr and } A=2.70 \text{ Mdyn cm}^{-2}.$$

The derivative of eq (6.1)

$$\partial G/\partial fp = ST + H \qquad (6.2)$$

showing that linearity should be expected in the increasing function plotted in figure 6, permits the evaluation of the other two constants from the slope and intercept of this line of positive slope.

The least squares computation in this case gives the slope $S=(5.925\pm0.018)\times10^{-3}$ Mdyn cm^{-2} K^{-1} (phr)$^{-1}$ and the intercept at 0 K, $H=0.0684\pm0.0055$ Mdyn cm^{-2} (phr)$^{-1}$.

Thus eq (6.1) becomes

$$G=5.925\times10^{-3}\ (fp-0.45)T + 0.0684\ (fp-0.45)+2.70 \qquad (6.3)$$

where G is in Mdyn cm^{-2}, T in kelvins, and fp in phr. This single equation with its four constants empirically determined represents satisfactorily all the data for modulus obtained in the present work. The lower limit of the temperature range covered was set by the occurrence of phenomena related to the glass transition and the upper limit was set at 373.15 K (100 °C) because of possible degradation at higher temperatures.

The data at low values of fp, where there was appreciable creep, were somewhat less reliable than those where there was no creep, but did not deviate systematically from the expected values obtained by extrapolation downward from the region where fp was large. The dashed straight line shown in figure 2 corresponding to $fp=0$ was drawn to pass through the extrapolated value of $G=1.88$ Mdyn cm^{-2} at 25 °, as already stated, but was not used in determining any of the constants.

G_0 the intercept at $fp=0$, is obtained from eq (6.1) as

$$G_0=SBT+HB+A=-2.63\times10^{-3}T+2.67. \qquad (6.4)$$

Figure 6 shows a line of negative slope corresponding to this equation for comparison with the experimental values of G_0 taken from table 2 (fourth column), obtained by least squares from data like that of figure 5. If eq (6.1) is differentiated with respect to temperature one obtains

$$\partial G/\partial T = Sfp + SB = 5.925\times10^{-3}fp - 2.67\times10^{-3}. \qquad (6.5)$$

This relationship is shown in figure 7 where the line corresponding to the equation can be compared with the experimental points taken directly as the slopes of the straight lines in figures 2 and 3.

TABLE 2

T °C	$\frac{\partial G}{\partial fp}$ Mdyn cm^{-2} phr^{-1}	Std. Dev. Mdyn cm^{-2} phr^{-1}	G_0 Mdyn cm^{-2}	Std. Dev. Mdyn cm^{-2}	G at $fp=0.45$ Mdyn cm^{-2}
−50	1.393	0.048	2.07	0.52	2.70
−25	1.535	.038	2.06	.41	2.75
0	1.686	.035	1.96	.38	2.72
25	1.836	.042	1.88	.44	2.71
50	1.986	.054	1.80	.58	2.69
75	2.131	.066	1.75	.71	2.71
100	2.278	.085	1.70	.92	2.72

NOTE: 1 Mdyn cm^{-2} = 0.1 MN m^{-2}.

8. Comparison With Results of Other Observers

The values of modulus previously found over more limited ranges of variables by other methods of measurement are in general agreement with those reported here. Figure 8 shows a graph of the 10-min modulus at

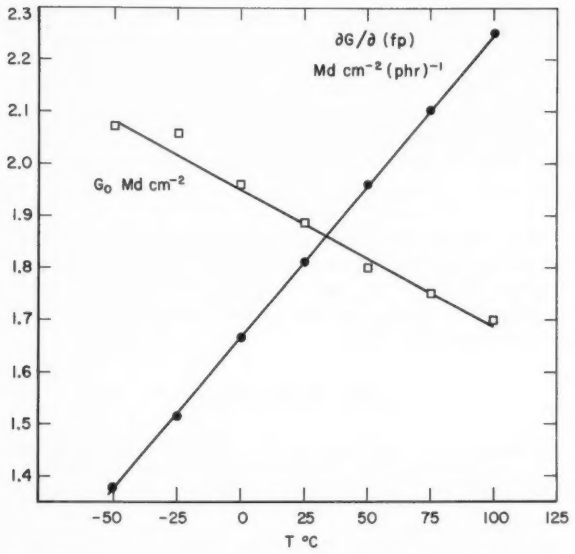

FIGURE 6. *Rate of increase of modulus with increase of decomposed dicumyl peroxide content as a function of temperature.*

● Data from table 2, column 2.

Modulus for no added dicumyl peroxide as a function of temperature.
□ Data from table 2, column 4.

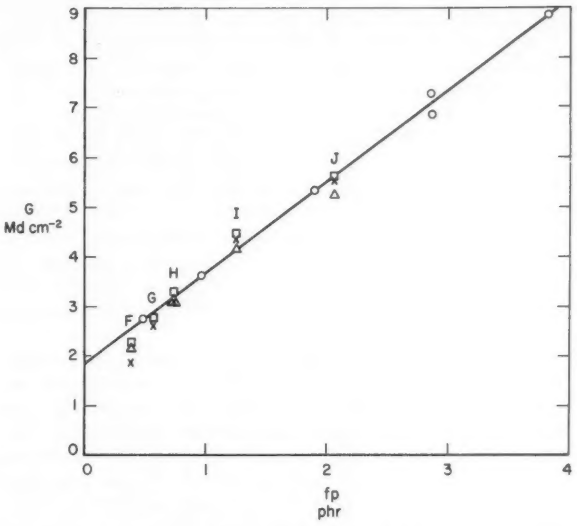

FIGURE 8. *Modulus at 30 °C as a function of decomposed dicumyl peroxide content.*

○ Present work.
□ Chasset and Thirion [17].
× Equilibrium value, Chasset and Thirion [17].
△ Plazek [20].

The straight line represents the function $G = 1.864\ fp + 1.86$ obtained from eq (6.3) at 30 °C.

30° over the lower range of values of *fp*. The straight line shown has the slope 1.864 Mdyn cm^{-2} per unit of *fp* and the intercept $G_0 = 1.86$ Mdyn cm^{-2}, as calculated from eq (6.3) at 30 °C (303.15 K). The experimental points from the present work were read directly from the straight lines of figure 2 at 30°.

Figure 8 also shows the results obtained by Chasset and Thirion [17] of the Institut Français du Caoutchouc who measured the stress at 30° in samples elongated 50 percent. The numerical values plotted here are given in tabular form in our earlier paper [3] devoted to creep. In their work specimens of natural rubber containing 3.5 parts of dicumyl peroxide per hundred of rubber were cured 20, 30, 40, 75, and 150 min at 135 °C and designated as F, G, H, I, and J respectively. The half-life at this temperature according to eq (1.3) using Hummel's constants, is 117.5 min. The value of f obtained from eq (1.1) for each specimen was multiplied by 3.5 and used as the abscissa in figure 8. The ordinates were computed from the stress at 50 percent elongation after 10 min of stress relaxation at 30° as reported by Chasset and Thirion. The ratio of F_{50}, the stress at 50 percent elongation to M, Young's Modulus, was taken from the empirical equation of Martin, Roth, and Stiehler [18] as $F_{50}/M = 0.3050$. Thus the shear modulus G was computed as 1.093 times the stress reported.

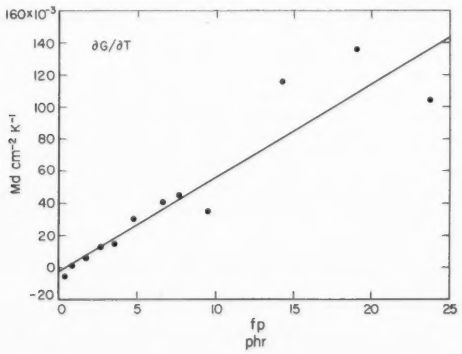

FIGURE 7. *Rate of increase of modulus with increase of temperature as a function of decomposed dicumyl peroxide content.*

● Slopes of the lines in figures 2 and 3.

The straight line represents eq (6.5), $\partial G/\partial T = 5.925 \times 10^{-3}\ fp - 2.67 \times 10^{-3}$.

$$\text{The value of } F_{50}/M = \frac{1}{3}(L_{50} - L_{50}^{-2}) = 0.3519$$

(where $L_{50} = 1.50$, the ratio of stressed length to unstressed length), given by the simple statistical theory of rubber elasticity was not used, since it gives, at 50 percent elongation, modulus values about 15.5 percent lower than those actually observed [19].

Chasset and Thirion [17] developed a relationship for calculating an equilibrium stress obtained by extrapolation to infinite time. Values of the transient term given by this relationship at 10 min can be read from figure 4 of their paper. The difference between the 10-min modulus and the equilibrium modulus is thus found to be 18, 9.6, 5.4, 2.5 and 1.2 percent of

448-417 O - 72 - 5

the equilibrium modulus for the Specimens F, G, H, I, and J respectively. Equilibrium modulus values and 10-min modulus values are both plotted in our figure 8. The difference between the two is considered to be negligible for values of fp greater than 2 phr.

Duplicates of specimens F, H, I, and J were furnished by Thirion to D. J. Plazek of Mellon Institute who measured [20] the shear modulus with a torsion pendulum at very low deformations. The 10-min moduli at 30° (as read from the compliances shown in figure 2 of Plazek's paper) are also plotted as ordinates in our figure 8. The values of Chasset and Thirion together with those of Plazek are likewise plotted at 30° in our figure 2.

All three sets of observations, in which the moduli were measured by widely different techniques on specimens prepared under different conditions are represented in a highly satisfactory fashion by the line shown. The creep calculated from the observations of Chasset and Thirion and of Plazek was also in good agreement with the present studies at comparable degrees of cross-linking [3, 4].

The data of Chasset and Thirion and of Plazek, just discussed, were confirmed by similar results on duplicates of these specimens investigated in Ferry's laboratory at the University of Wisconsin [21, 22]. On the whole, these results appear to be better suited than other literature studies to be subjected to a direct comparison with those of the present work. An examination of several other investigations also permits the calculation of values of G in general agreement with our own.

9. Summary and Conclusions

The modulus G of natural rubber cross-linked with varying amounts of dicumyl peroxide has been calculated from indentation measurements. A fraction f, of the number of parts p, of dicumyl peroxide added per hundred parts of rubber is decomposed during the time of cure and thereby rendered effective for cross-linking. The results obtained are represented by the general relation.

$$G = S(fp + B)T + H(fp + B) + A \qquad (6.1)$$

where T is the temperature in kelvins and A, B, H, and S are constants with the following values:

$A = 2.70$ Mdyn cm^{-2}
$B = -0.45$ phr
$S = 5.925 \times 10^{-3}$ Mdyn cm^{-2} (phr)$^{-1}$ K^{-1} and
$H = 0.0684$ Mdyn cm^{-2} (phr)$^{-1}$.

The equation represents the data obtained in the range of temperature from -50 to $+100$ °C for values of fp from about 1 to 24 phr. It can be readily noted that the modulus is 2.70 Mdyn cm^{-2} when $fp = 0.45$ for all values of temperature.

The glass transition, manifesting itself as a discontinuity in the slope of the modulus-temperature relation, was found to be raised by about 1.2° for each part fp of decomposed dicumyl peroxide.

The thermodynamic consequences and molecular interpretation of these experimental results together with a comparison with the predictions of the simplest form of statistical theory of rubber elasticity, will be the subject of a second paper in this series.

The authors acknowledge with thanks the assistance of Albert M. Brown of the Product Evaluation Technology Division of the Institute of Applied Technology, who made several of the experimental observations reported here.

10. References

[1] Wood, L. A., and Roth, F. L., Creep of pure-gum rubber vulcanizates from indentation-time measurements, Proc. 4th Rubber Technol. Conf., London 1962, p. 328; Institution of Rubber Industry, London, 1963, Rubber Chem. Technol. **36,** 611 (1963).

[2] Roth, F. L., Bullman, G. W., and Wood, L. A., Compliance-time-temperature relationships from indentation measurements on a pure-gum rubber vulcanizate, J. Res. Nat. Bur. Stand. **69A,** 347 (1965); Rubber Chem. Technol. **39,** 397 (1966).

[3] Wood, Lawrence A., Creep of pure-gum vulcanizates of natural rubber, J. Rubber Res. Inst. Malaya **22,** (3), 309 (1969); Rubber Chem. Technol. **43,** 1482 (1970).

[4] Wood, Lawrence A. and Bullman, George W., Creep and other tensile properties of rubber cross-linked by dicumyl peroxide, J. Polymer Sci. A-2, **10,** (1972).

[5] Loan, L. D., Mechanism of the peroxide vulcanization of elastomers, Rubber Chem. Technol. **40,** 149 (1967).

[6] Hummel, K., Scheele, W., and Hillmer, K. H., Vulcanization of natural rubber by dicumyl peroxide in the absence of additives, Kautschuk Gummi **14,** (6), WT 171 (1961).

[7] Hertz, H., J. Math. (Crelle's J.) **92,** 156 (1881), Gesammelte Werke, Vol. **1,** p. 155 and 174, Barth. Leipzig 1895; Miscellaneous Papers, Translated into English by D. E. Jones and G. A. Schott, p. 146 and 163, MacMillan, London, 1896.

[8] Timoshenko, S. and Goodier, F. N., Theory of Elasticity, 3rd Edition, p. 412 (McGraw Hill, New York, 1970).

[9] Larrick, L., The hardness of rubber and other highly elastic materials, Abstract, Phys. Rev. **57,** 358 (1940); The standardization of durometers, Rubber Chem. Technol. **13,** 969 (1940).

[10] Gent, A. N., On the relation between indentation hardness and Young's Modulus, Trans. Inst. Rubber Ind. **34,** 46 (1958); Rubber Chem. Technol. **31,** 896 (1958).

[11] Scott, J. R., Rubber hardness testing, Rubber Age (N.Y.) **77,** 543 (1955); Rubber Chem. Technol. **28,** 1071 (1955).

[12] Waters, N. E., The indentation of thin rubber sheets by spherical indentors, Brit. J. Applied Phys. **16,** 557 (1966).

[13] Waters, N. E., Variation of indentation hardness with sample thickness, J. Inst. Rubber Ind. **43,** 51 (1967).

[14] Meyer, Kurt H. and Ferri, Cesare, The elasticity of rubber, Helvetica Chim. Acta **18,** 570 (1935); Rubber Chem. Technol. **8,** 319 (1935).

[15] Witte, Robert S. and Anthony, Robert L., Stress-temperature studies of transitions in rubbers, J. Applied Phys. **22,** 689 (1951); Rubber Chem. Technol. **25,** 468 (1952).

[16] Mason, P., Thermal expansion and viscoelasticity of rubber in relation to cross-linking and molecular packing, Polymer **5,** 625 (1964); Rubber Chem. Technol. **39,** 408 (1966).

[17] Chasset, R. and Thirion, P., Viscoelastic relaxation of rubber vulcanizates between the glass transition and equilibrium, Proc. Int. Conf. Non-Crystalline Solids, Delft 1964, J. A. Prins, Ed., p. 345, North-Holland Publishing Co., Amsterdam, Interscience Publishers, New York; Rubber Chem. Technol. **39,** 870 (1966); Rev. Gen. Caoutchouc **44,** 1041 (1967).

[18] Martin, G. M., Roth, F. L., and Stiehler, R. D., Behavior of pure-gum rubber vulcanizates in tension, Trans. Inst. Rubber Industry **32,** (6), 189 (1956); Rubber Chem. Technol. **30,** 876 (1957).

[19] Wood, Lawrence A., Stress-strain relation of pure-gum rubber vulcanizates in compression and tension, J. Research Nat. Bur. Standards **60,** 193 (1958); Rubber Chem. Technol. **32,** 1 (1959).

[20] Plazek, D. J., Effect of cross-link density on the creep behavior of natural rubber vulcanizates, J. Polymer Sci. A-2, **4,** 745 (1966).

[21] Ferry, John D., Mancke, Ralph G., Maekawa, Etsuji, Oyanagi, Yasuji, and Dickie, Ralph A. Dynamic mechanical properties of cross-linked rubber. I. Effects of cross-link spacing in natural rubber. J. Phys. Chem. **63,** 3414 (1964) Rubber Chem. Technol. **39,** 897 (1966).

[22] Dickie, R. A., and Ferry, John D. Mechanical properties of substances of high molecular weight. L. Dynamic mechanical properties of cross-linked rubbers. III. Dicumyl peroxide vulcanizates of natural rubber. J. Phys. Chem. **70,** 2594 (1966).

(Paper 76A1-698)

JOURNAL OF RESEARCH of the National Bureau of Standards—A. Physics and Chemistry
Vol. 76A, No. 1, January–February 1972

Publications of the National Bureau of Standards *

Selected Abstracts

Abramowitz, S., Acquista, N., Thompson, K. R., **The infrared spectrum of matrix-isolated uranium monoxide,** *J. Phys. Chem.* **75,** *No. 15, 2283–2285 (1971).*

Key words: High temperature; infrared; matrix isolation; uranium monoxide; uranium oxides; vibrational frequency.

The infrared spectra of matrix-isolated uranium oxides have been observed. By varying the O/U ratio of the condensed phase from 1.5 to 3.0 and comparing the observed spectra of the matrix-isolated vapors in equilibrium with the condensed phases it has been possible to assign a frequency of 776.0 cm^{-1} to $U^{16}O$. Verification of this assignment has been obtained in similar experiments using oxygen-18 enriched uranium oxides; a frequency of 736.2 cm^{-1} has been observed for $U^{18}O$. This yields a force constant to the harmonic approximation of 5.32 mdyn/Å for this species. A stretching mode of UO_2 has also been assigned for $U^{16}O_2$, $U^{18}O_2$, and $U^{16}O^{18}O$.

Allpress, J. G., Roth, R. S., **The effect of annealing on the concentration of Wadsley defects in the $Nb_2O_5-WO_3$ system,** *J. Solid State Chem.* **3,** *209–216 (1971).*

Key words: Annealing equilibria; electron microscopy; niobium tungsten system; Wadsley defects.

Mixtures of $xNb_2O_5 \cdot yWO_3$ with $x:y = 9:8$, $8:5$, and $8:1$ have been annealed at high temperatures for prolonged periods before quenching to room temperature. The concentration of Wadsley defects, estimated from lattice image electron micrographs of a few fragments in each sample, is reduced during this treatment. The results indicate that (1) the high temperature equilibrium is attained very slowly, and in stoichiometric samples probably involves the complete removal of Wadsley defects; (2) the high temperature situation is not seriously affected by the quenching treatment; and (3) variations in stoichiometry may be accommodated by means other than the presence of Wadsley defects.

Bennett, H. S., **Acoustic phonons in Heisenberg paramagnets,** *J. Phys.* **32,** *No. C1, 526–527 (February/March 1971).*

Key words: Frequency shift; Heisenberg paramagnet; specific heat; spin diffusion; susceptibility; ultrasonic attenuation.

The propagation of sound waves in ferromagnetic and antiferromagnetic insulators is examined in terms of a volume magnetostrictive interaction. Expressions for the ultrasonic attenuation coefficients and for the phonon frequency shifts near the transition temperature are given as functions of the static susceptibilities, the spin diffusion coefficients, and the specific heats. The results agree with scaling law calculations and qualitatively with experiment.

Bloom, D. W., Finegold, L., Lye, R. G., Radebaugh, R., Siegwarth, J. D., **Upper limit on electron-photon interaction in vanadium carbide,** *Physics Letters* **33A,** *No. 3, 137–138 (October 19, 1970).*

Key words: Band structure of solids; cryogenics; superconductivity; transition temperatures; vanadium carbides.

Single crystals of VC_x (× 0.87. 0.84. 0.81. 0.76) were not superconducting above 30 mK, indicating that the electron-phonon enhancement of the densities of states determined from electronic specific heats is less than 30 percent.

Braun, W., Peterson, N. C., Bass, A. M., Kurylo, M. J., **A vacuum ultraviolet atomic emission detector: Quantitative and qualitative chromatographic analysis of typical C, N, and S containing compounds,** *J. Chromatog.* **55,** *237–248 (1971).*

Key words: Analytical; atomic emission; detector; gas chromatography; spectroscopy; vacuum ultraviolet.

Vacuum ultraviolet atomic emission detection of effluent gases from a chromatographic column is a very sensitive and selective method for qualitative and quantitative elemental analysis of carbon, nitrogen, and sulfur compounds. A low pressure microwave discharge through helium, with added trace amounts of molecular oxygen, produced complete fragmentation of all compounds used and generated intense atomic emissions in the vacuum ultraviolet. Photometric measurement of these monochromator-isolated atomic emissions was successfully used to establish absolute concentration calibrations for the elements carbon, sulfur and nitrogen in various compounds. This detection method is sensitive, highly selective, and has a range of linearity greater than four decades.

Bullis, W. M., Editor, **Methods of measurement for semiconductor materials, process control, and devices,** *Quarterly Report October 1 to December 31, 1970, Nat. Bur. Stand. (U.S.), Tech. Note 592, 72 pages (Aug. 1971) 70 cents, SD Catalog No. C13.46:592.*

Key words: Alpha-particle detectors; aluminum wire; base transit time; carrier lifetime; die attachment; electrical properties; epitaxial silicon; gamma-ray detectors; germanium; gold-doped silicon; metallization; methods of measurement; microelectronics; microwave devices; nuclear radiation detectors; probe techniques (a-c); resistivity; semiconductor devices; semiconductor materials; semiconductor process control; silicon; thermal resistance; thermographic measurements; ultrasonic bonder; wire bonds.

This quarterly progress report, tenth of a series, describes NBS activities directed toward the development of methods of measurement for semiconductor materials, process control, and devices. Significant accomplishments during this reporting period include successful application of the surface photovoltage technique, a non-contacting method, to the measurement of carrier diffusion length in silicon epitaxial layers and development of a novel, but simple, method for measurement of acceleration and terminal angular velocity of a photoresist spinner. Work is continuing on measurement of resistivity, carrier lifetime, and electrical inhomogeneities in semiconductor crystals; specification of germanium for gamma-ray detectors; evaluation of wire bonds, metallization ad-

Publications for which a price is indicated are available by purchase from the Superintendent of Documents, U.S. Government Printing Office, Washington, D.C. 20402 (foreign postage, one-fourth additional). The NBS non-periodical series are also available from the National Technical Information Service (NTIS), Springfield, Va. 22151, which was formerly the Clearinghouse. Reprints from outside journals and the NBS Journal of Research may often be obtained directly from the authors.

hesion, and die attachment; measurement of thermal properties of semiconductor devices, transit-time and related carrier transport properties in junction devices, and electrical properties of microwave devices; and characterization of silicon nuclear radiation detectors. Supplementary data concerning staff, standards committee activities, technical services, and publications are included as appendixes.

Byerly, R., Jr., Beaty, E. C., **Sunlight photodetachment of O_3^-,** *J. Geophys. Res.* **76,** *No. 19, 4596–4601 (July 1, 1971).*

Key words: Ion mobility; O_3^-; photodetachment; photodetachment rate detachment; sunlight.

The rate of photodetachment of O_3^- by sunlight has been determined. The O_3^- ions were identified by their mobility as they drifted in a weak field in 1 torr of O_2 buffer gas. This allowed the ions to lose any vibrational or electronic excitation through collisions with the buffer gas. Energy dependence of the cross section was estimated by the use of colored filters in the photon beam. The sunlight photodetachment rate measured was 0.2 ± 0.1 s^{-1}.

Carpenter, B. S., **The use of the nuclear track technique for boron and uranium analyses in botanical material,** *(Proc. American Nuclear Society Meeting, Boston, Mass., June 17, 1971), Trans. Am. Nucl. Soc.* **14,** *No. 1, 130–131 (1971).*

Key words: Alpha tracks; boron; botanical material; fission tracks; kale; orchard leaves; uranium.

The Nuclear Track Technique is used to determine trace quantities of boron and uranium in botanical materials. This technique uses both method of standard additions and the absolute method in its determinations.

Carroll, J. J., Melmed, A. J., **Optical constants of (011) tungsten in the visible region,** *J. Opt. Soc. Am.* **61,** *No. 4, 470–473 (April 1971).*

Key words: Absorption; ellipsometry; refractive index; tungsten.

Optical constants for tungsten measured ellipsometrically at room temperature in the visible spectrum are reported. Results are given for (011)-oriented tungsten characterized as clean by low-energy-electron diffraction, for the same surface saturated with oxygen, and for the surface after exposure to air at atmospheric pressure for several hours. Results are compared with earlier work and differences are attributed primarily to differences of surface contamination.

Cohen, J., Edelman, S., **Piezoelectric effect in oriented polyvinylchloride and polyvinylfluoride,** *J. Appl. Phys.* **42,** *No. 8, 3072–3047 (July 1971).*

Key words: G moduli; piezoelectricity; polyvinylchloride; polyvinylfluoride.

The direct piezoelectric effect has been observed in roll-elongated films of polyvinylchloride and polyvinylfluoride. The effect was produced by applying tensile stress to a clamped specimen at a fixed frequency of 20 Hz. The piezoelectric modulus, g_{31} was determined to be 0.2 to 0.7 $V\ m^{-1}/N\ m^{-2}$ in polyvinylchloride; in polyvinylfluoride $g_{31} \simeq 0.2\ V\ m^{-1}/N\ m^{-2}$ and $g_{32} \simeq 1\ V\ m^{-1}/N\ m^{-2}$. The piezoelectric effect in these films is believed to be due to mechanical distortion of oriented dipoles, resulting from the tensile stress, and the orientation appears to differ in the two materials.

Cornog, J. R., Bunten, E. D., **U.S. Metric Study Interim Report: Nonmanufacturing businesses,** *Nat. Bur. Stand. (U.S.), Spec. Publ. 345–5, 200 pages (July 1971) $1.50, SD Catalog No. C13.10: 345–5.*

Key words: International System of Units; metric conversion; metric system; metric usage; metrication; metrication, attitudes toward; metrication, costs and benefits of; metrication, impact of; nonmanufacturing businesses; SI; U.S. Metric Study.

This publication, prepared pursuant to the U.S. Metric Study Act, reports on the experiences and views of non-manufacturing businesses with regard to metric usage and its increase. The study is based on a survey of more than 2500 companies and firms primarily involved in: agriculture, forestry, fisheries, mining, construction, transportation, communications, utilities, wholesale/retail trade (including exporters/importers), finance, insurance, real estate or services. Information was obtained on: past or present experience with use of the metric system (including perceived advantages and disadvantages thereof), attitudes toward future metrication in a world of increasing metric usage (including preferred U.S. policy regarding), and estimated cost impacts and benefits which would be attendant to a national metrication program.

Coxon, B., **Application of internuclear, double-resonance techniques to carbohydrates. Detection of small coupling-constants,** *Carbohydrates Res.* **18,** *No. 3, 427–442 (1971).*

Key words: 6-Deoxy·α-D-glucofuranose derivative; general Overhauser effect; internuclear double resonance; magnetic equivalence factoring; spin-tickling; transient nutations.

6-Deoxy-1,2:3,5-di-O-isopropylidene-α-D-glucofuranose-d_{12}(**1**-d_{12}) has been synthesized by exchange of its non-deuterated analog (**1**) with acetone-d_6. The p.m.r. spectrum of **1**-d_{12} at 90 MHz has been analyzed iteratively by means of a computer program for magnetic-equivalence factoring. Confirmation of the assignments of lines in the analysis has been investigated by proton–proton, internuclear, double-resonance (i.n.d.o.r.) techniques, which served also for the detection of a small long-range coupling-constant.
Examples of i.n.d.o.r. spectra containing general Overhauser effects, spin-tickling effects, or transient nutations are shown, and are discussed in relation to the experimental power-levels of the observing and double-resonance frequencies, and their sweep-rates.

Dean, J. W., Brennan, J. A., Mann, D. B., Kneebone, C. H., **Cryogenic flow research facility provisional accuracy statement,** *Nat. Bur. Stand. (U.S.), Tech. Note 606, 40 pages (July 1971) 45 cents, SD Catalog No. C13.46:606.*

Key words: Accuracy statement; cryogenic; flow facility; liquid nitrogen; measurement.

The National Bureau of Standards and the Compressed Gas Association have jointly sponsored a research program on cryogenic flow measurement. A cryogenic flow research facility was constructed and ,was first used to evaluate commercially available cryogenic flowmeters operating with liquid nitrogen on a positive displacement principle.
The performance of the flow facility was simultaneously being evaluated during the meter tests. This is a summary report of the performance evaluation of the flow facility. An accuracy statement is given for both totalized mass and volumetric flow.

Dehmer, J. L., Starace, A. F., Fano, U., Sugar, J., Cooper, J. W., **Raising of discrete levels into the far continuum,** *Phys. Rev. Letters* **26,** *No. 25, 1521–1525 (June 21, 1971).*

Key words: Absorption; lanthanides: theory; x-rays.

Broad peaks observed in the photoabsorption spectra of rare earths ~ 10–20 eV above the 4*d* edge are attributed to transitions $4d^{10}4f^N \rightarrow 4d^94f^{N+1}$. Exchange interaction splits the $4d^94f^{N+1}$ configuration and raises some multiplets by ~ 20 eV. Autoionization extends to $4d^9 - 4f^N\epsilon f$ broadens the high levels. The interpretation extends to $p \rightarrow d$ processes observed in the absorption of synchrotron light by transition elements.

DeSimone, D. V., **A Metric America: A decision whose time has come,** *Nat. Bur. Stand. (U.S.), Spec. Publ. 345, 184 pages (July 1971) $2.25, SD Catalog No. C13.10:345.*

Key words: Metric conversion; metric system; metric usage; metrication; Public Law 90–472; U.S. Metric Study.

This publication is the comprehensive report on the U.S. Metric Study undertaken by the National Bureau of Standards pursuant

to Public Law 90–472. The report evaluates and distills the information contained in the twelve interim reports of the study series and also covers what has been learned from Great Britain and other countries that are now in or have been involved in a metric changeover. Data in the report show that America is already metric in some respects and that the great majority of businessmen, educators and other informed participants in the study reported that increased use of the metric system is in the best interests of America. Included in the publication are the recommendations of the Secretary of Commerce to Congress that the United States change to the metric system through a coordinated national program over a ten-year period.

Dickens, B., Brown, W. E., **The crystal structure of $Ca_5(PO_4)_2SiO_4$ (silico-carnotite),** *Tschermaks Mineral. Petrog. Mitt.* **16,** *1–27 (June 1971).*

Key words: Calcium phosphate; calcium phosphate-calcium silicate solid solution; calcium phosphosilicates; calcium silicates crystal structure; glaserite; hydroxyapatite; single crystal x-ray diffraction.

The crystal structure of $Ca_5(PO_4)_2SiO_4$ (silico-carnotite) has been determined from 3358 x-ray diffraction data collected by a counter method and has been refined to $R_w = 0.038$, $R = 0.045$ in space-group Pnma. The unit cell parameters are $a = 6.737(1)$ Å, $b = 15.508$ (2) Å and $c = 10.132(1)$ Å at 24 °C; $Z = 4$. The observed density is 3.06 and the calculated density is 3.03 g · cm^{-3}. The crystal contains about 2.5% V_2O_5 as an impurity. The bond lengths within the tetrahedral anions suggest that substitution or disorder of PO_4^{3-}, SiO_4^{4-} and possibly VO_4^{3-} occurs among the anion sites. The structure has some relationship to that of $Ca_5(PO_4)_3OH$, the predominant inorganic phase in the human body, but suggests that the $Ca_5(PO_4)_3$ OH type structure may not be stable without some of the OH positions being filled. $Ca_5(PO_4)_2SiO_4$ is more closely related to $K_3Na(SO_4)_2$ (glaserite) if it is considered that there are systematic cations vacancies in $Ca_5(PO_4)_2SiO_4$.
This type of structure is consistent with the view that cation vacancies in the glaserite-type structure account for solid solutions between Ca_2SiO_4 and $Ca_3(PO_4)_2$ and between $Ca_3(PO_4)_2$ and $CaNaPO_4$.

Dickens, B., Brown, W. E., **The crystal structure of $Ca_7Mg_9(Ca, Mg)_2(PO_4)_{12}$,** *Tschermaks Mineral. Petrog. Mitt.* **16,** *79–104 (June 1971).*

Key words: Alpha-$Ca_3(PO_4)_2$; calcium magnesium cation vacancies; glaserite; phosphate; single crystal x-ray diffraction.

The unit cell of $Ca_7Mg_9(Ca, Mg)_2(PO_4)_{12}$ is $a = 22.841(3)$ Å, $b = 9.994(1)$ Å, $c = 17.088(5)$ Å, $d = 99.63(3)$ Å at 24 °C. The space-group is C2/c with four formula weights per cell. The crystal structure has been determined from 6330 x-ray reflections measured from a single crystal by a counter method and has been refined to $R_w = 0.044$, $R = 0.046$ (based on 4227 observed reflections and 322 of the unobserved, reflections). One cation site may be occupied by Ca or Mg and gives rise to variability in composition as is reflected in the formula given above. In the sample studied, Ca and Mg occupy the site approximately equally. The $[10\bar{2}]$ direction in the unit cell is pseudo-hexagonal. The structure of $Ca_7Mg_9(Ca, Mg)_2(PO_4)_{12}$ is related to that of $K_3Na(SO_4)_2$ in that along $[10\bar{2}]$ it has columns of cations and columns of cations and anions. These columns are arranged in a $K_3Na(SO_4)_2$-type pseudo-cell. In the cation-anion columns, every other cation site in $K_3Na(SO_4)_2$ is vacant in $Ca_7Mg_9(Ca, Mg)_2(PO_4)_{12}$.

Edelman, S., Grisham, L. R., Roth, S. C., Cohen, J., **Improved piezoelectric effect in polymers,** *J. Acoust. Soc. Am.* **48,** *No. 5, Part 1, 1040–1043 (November 1970).*

Key words: Piezoelectricity; polymers; polyvinylchloride; strain modulus; under water sound receiver.

Improved poling techniques have led to improvement in the piezoelectric activity of bulk polymers. Results now achieved approach the activity of conventional piezoelectric materials such as quartz, and further improvement is anticipated. The measured value of the piezoelectric strain modulus d_{31} of a length expander bar of polyvinylchloride was 0.6×10^{-12} m V^{-1} and the electromechanical coupling factor k_{31} was 0.6 percent. The response of a sample as an underwater sound receiver was −112 dB *re* 1 V/μbar.

Edsinger, R. E., Guildner, L. A., Anderson, R. L., **Precision measurement of internal diameters of long, small bore metal tubing,** *Rev. Sci. Instr.* **42,** *No. 7, 945–950 (July 1971).*

Key words: Capacitance probe; cylindrical gage blocks; inside diameters; small-bore tubes; standard hole, wringing.

Internal diameters of a long, small-bore metal tube were calculated from the measured capacitances between it and a cylindrical coaxial probe of known characteristics. The tube and the probe were used as the electrodes of a three-lead capacitor, measurable with high accuracy in a transformer ratio-arm bridge. For tubes of 0.1 cm bore or less, average diameters as a function of position can be determined by this method with an overall uncertainty of $\pm 6 \times 10^{-5}$ cm over lengths of 1 meter. The method can readily be extended to larger bores and greater lengths.

Fickett, F. R., **Magnetoresistance of very pure polycrystalline aluminum,** *Phys. Rev. B.* **3,** *No. 6, 1941–1952 (March 15, 1971).*

Key words: Aluminum; electron scattering; magnetoresistance; resistance.

The behavior of the resistance of polycrystalline aluminum wires as a function of magnetic field and purity at temperatures of 4, 15, and 19.6K is reported. Both longitudinal and transverse configurations were measured. The residual resistance ratios of the specimens varied from 1600 to 31000. The measured magnetoresistance ($\Delta R/R_o$) is separated into a saturating and a linear part. The value of the saturating component is high at 19.6K but is shown to be less than 6, even in the limit of infinite specimen purity. The linear component varies with both temperature and purity. Possible sources for the large saturating magnetoresistance values and for the variations observed in the linear portion are discussed. An analysis scheme is presented which allows prediction of the saturating component from zero-field resistance values. A deviation from Matthiessen's rule observed here, and by several other experimenters, is presented and discussed.

Gibson, B. F., Williams, H. T., **Virtual photon cross sections for two-body electrodisintegration,** *Nucl. Phys.* **A163,** 193–202 (1971).

Key words: Cross section; electric transition; electrodisintegration; few nucleon systems; long wave.

Two-body electrodisintegration cross sections (differential with respect to the angles of the ejected nuclear fragment) are developed in the long wavelength limit of virtual photon theory for the few-nucleon system. Only the non-spin-flip electric transitions are considered. Contributions from the multipole expansion through the E1–E3 interference terms are retained. Comparable photodisintegration expressions are included to facilitate the extraction of photo cross sections from appropriate inelastic electron scattering data.

Gordon, G. F., **U.S. Metric Study Interim Report: International trade,** *Nat. Bur. Stand. (U.S.), Spec. Publ. 345–8, 188 pages (July 1971)* **$1.50, SD Catalog No. C13.10:345–8.**

Key words: Foreign trade; International System of Units; metric conversion; metric conversion, effect on foreign trade; metric system; metric usage; metric usage, effect on foreign trade; metrication; metrication, impact of on foreign trade; SI; U.S. Metric Study.

This publication, one of a series prepared pursuant to the U.S. Metric Study Act, evaluates the potential effects that a U.S. conversion to the metric system may have on the Nation's foreign trade. The report is based on a survey of exporters and importers trading in measurement-sensitive products, which was conducted by the Bureau of Domestic Commerce of the Department of Commerce.

Hastie, J. W., **Thermodynamic studies, by mass spectrometry, of molten mixed halide systems,** *Chapter 5 in Advances in Molten*

Salt Chemistry **1**, *225–257 (Plenum Press, Inc., New York, N.Y., 1971).*

Key words: Complex molecules; mass spectrometry; molten salt halides; thermodynamics.

The thermodynamic properties of the complex vapors, present in molten mixed halide systems, are reviewed and evaluated. Also, the special techniques required for these studies are critically discussed. A model, based on entropy and enthalpy correlations, is proposed whereby the complex vaporization phenomenon can be rationalized and predictions made for unstudied systems.

Hastie, J. W., Hauge, R. H., Margrave, J. L., **Infrared spectra and geometries for the dichlorides of Ca, Sc, Ti, V, Cr, Mn, Fe, and Ni,** *High Temp. Sci.* **3,** *No. 3, 257–274 (May 1971).*

Key words: Dichlorides of Ca, Sc, Ti, V, Cr, Mn, Fe, Ni, $ScCl_3$, $TiCl_4$, $TiCl_4$; geometry; infrared spectra of species; matrix isolation.

The dichloride species of Ca, Sc, Ti, V, Cr, Mn, Fe, and Ni, prepared by Knudsen cell techniques have been isolated in solid inert gas matrices and infrared spectra obtained over the range 33–1000 cm^{-1}. Spectra were also observed for $ScCl_3$, $TiCl_3$ and $TiCl_4$. Isotope shift measurements and the infrared selection rules indicate each of the dichlorides to be linear $D_{\infty h}$ species within the experimental bond angle uncertainty of about 10°. In several instances the results implied a significant anharmonic effect on the isotope shifts. Significant differences in the geometry and vibrational data between the dichlorides and the corresponding difluorides are noted.

Heuer, A. H., Hockey, B. J., Wiederhorn, S. M., **Discussion of "Observation of plastic deformation in sapphire base ceramics,"** *Metallurgical Trans.* **2,** *1475–1476 (May 1971).*

Key words: Alumina; fracture; mechanical properties; plastic deformation; sapphire; strength.

A paper presented in Metallurgical Abstracts by George F. Hurley is discussed. It is concluded that the observations concerning plastic deformation in sapphire-based ceramics are incorrect and that there is no evidence at present to link plastic deformation and fracture to alumina ceramics.

Kieffer, L. J., **Low-energy electron-collision cross-section data Part III: Total scattering; differential elastic scattering,** *Atomic Data* **2,** *No. 4, 293–391 (June 1971).*

Key words: Atom; cross section; elastic scattering; electron; molecule.

This is the final part of a three part compilation of low-energy electron-collision cross-section data issued by the Joint Institute for Laboratory Astrophysics (JILA) Information Center. Only experimental values are included for all atomic species and for those molecules which are important for aeronomy, astrophysics and plasma physics. The data included here were taken from literature published through July 1970.

Kirsch, R. A., **Computer determination of the constituent structure of biological images,** *Comput. Biomed. Res.* **4,** *315–328 (1971).*

Key words: Artificial intelligence; image processing; pattern recognition.

A class of algorithms is described which enables computer quantized images to be decomposed into constituent parts reflecting the structure of the images. This decomposition is viewed as the morphological precursor to a higher level syntactic analysis. Numerical results for a typical biological image are presented.

Kuriyama, M., **On the principle of x-ray interferometry,** *Acta Cryst.* **A27,** *273–280 (1971).*

Key words: Diffraction theory; lattice constants; measurements; x-ray interferometry; wave optics.

The scattering amplitude of an x-ray interferometer is calculated using a general theory of x-ray diffraction. Analytic expressions are given for the intensities of diffracted beams in interferometry; these expressions include the effect of the positions of each crystal lattice in addition to ordinary dynamical effects. It is concluded that the fringes observed in x-ray interferometry of a lattice spacing are accounted for by an optical effect rather than by dynamical effects of x-ray diffraction.

LaVilla, R. E., **Neon K emission spectrum,** *Phys. Rev. A.* **4,** *No. 2, 476–480 (August 1971).*

Key words: Electron excitation; neon K emission spectrum; x-ray emission; x-ray satellites.

The neon K emission spectrum, excited by direct electron bombardment of the neon gas, has been obtained with photon counting on a single crystal (KAP) planar spectrometer. The measured relative integrated intensity of the $\alpha' \alpha_5 \alpha_4$ and $\alpha_5 \alpha_6$ satellite groups were found to be larger than theoretical prediction but in accord with the trend of previous comparisons for K satellites of neon-like ions in solids. A comparison of the present results for electron excitation and the preliminary results by O. Keski-Rahkonen and T. Åberg for photon excitation indicates that the relative integrated intensity of the neon K satellites is independent of excitation mode at the excess excitation energies employed. A weak increase of intensity on the low energy side of $K\alpha_{1,2}$ in the 803 to 809 eV region was recorded and can be attributed to a radiative Auger transition.

McCarty, R. D., Weber, L. A., **Thermophysical properties of oxygen from the freezing liquid line to 600 R for pressures to 5,000 psia,** *Nat. Bur. Stand. (U.S.), Tech. Note 384, 189 pages (July 1971) $1.50, SD Catalog No. C13.46:384.*

Key words: Density; dielectric constant; enthalpy; entropy; equation of state; fixed points; heat transfer coefficients; index of refraction; Joule-Thomson; latent heat; melting point; Prandtl number; oxygen; specific heat.

Tables of thermophysical properties of oxygen are presented for temperatures from the melting line to 600 R for pressures to 5000 psia. The tables include, entropy, enthalpy, internal energy, density, volume, speed of sound, specific heat, thermal conductivity, viscosity, thermal diffusivity, Prandtl number and the dielectric constant for 79 isobars. Also included in the isobaric tables are quantities of special utility in heat transfer calculations:

$$(\partial P/\partial V)_T,\ 4\#P/\partial T)_p,\ V(\partial H/\partial V)_P,\ V(\partial P/\partial U)_V,$$
$$-V(\partial P/\partial V)_T,\ 1/V(\partial V/\partial T)_P.$$

In addition to the isobaric tables, tables for the saturated vapor and liquid are given which include all of the above properties, plus the surface tension. Tables for the P–T of the freezing liquid, index of refraction and the derived Joule-Thomson inversion curve are also presented. The specific heat of the saturated liquid is given in graphical form. A temperature-entropy chart and a Mollier diagram are also included.

Mohan, R., Danos, M., Biedenharn, L. C., **Three-fluid hydrodynamical model of nuclei,** *Phys. Rev. C.* **3,** *No. 5, 1740–1749 (May 1971).*

Key words: Charge distribution; collective midel; giant resonance; hydrodynamic model; isospin; nuclear structure.

A three fluid-model of nuclei is introduced, the three fluids being the protons, the neutrons of the same orbituals as protons and the excess neutrons, to account for the fact that the excess neutrons interact less strongly with the protons than do the neutrons which occupy the same space-spin states as the protons. Calculations of protons and neutron density distributions, of isotope shifts, and of isospin impurities have been carried out. The giant dipole phenomenon is also studied in the present model. It is found that a considerable improvement is achieved in the results for the protons density distribution and for the isospin impurities as compared with two-fluid model. The other results are found to be consistent with previous calculations.

Moore-Sitterly, C., **The periodic table interpreted from atomic spectra,** *Proc. Mendeleev Conf., Torino-Rome, Italy, September 15–21, 1969, pp. 163–188 (1969).*

Key words: Atomic spectra, regularities; periodic table; regularities, atomic spectra; Spectra, atomic.

The properties of the valence electrons as revealed by the configurations and energy levels in atomic and ionic spectra are discussed by considering four aspects of the periodic Chart of the Atoms.
The series in first spectra of three *vertical* groups are described: similarities in the doublet series Li I, Na I etc.; the significance of the double-electron jump in the spectra Ca I, Sr I, Ba I; the pair-coupling in Ne I, Ar I etc. The importance of Zeeman observations in interpreting spectra of magnetic stars, and similarities in complex spectra such as Mn I and Tc I reveal different types of regularities. In the *horizontal* grouping, the effect of building on electrons with increasing atomic number is illustrated by considering ionization potentials from H through Ca, and by inverted terms in complex spectra.
Isoelectronic sequences are extremely important for the analyses of spectra of highly-ionized atoms. The observations of the solar spectrum and of other stellar spectra from rockets and orbiting telescopes has created a sudden demand for laboratory data on these spectra. Extrapolation of intervals along the sequences of light elements has led to the identification of strong lines in the solar corona. Coronal lines recently identified by B. Edlen are described. A summary of spectra detected in the sun from H through Ni is presented. Finally, the inherent regularities in electron structure revealed by known spectra furnish methods that are a valuable guide in locating overlapping configurations in the complex rare-earth spectra. The theoretical work of G. Racah and the analysis of Yb II are used as examples.

Okabe, H., Laufer, A. H., Ball, J. J., **Photodissociation of $OCCl_2$ in the vacuum ultraviolet: Production and electronic energy of excited Cl_2,** *J. Chem. Phys.* **55,** *No. 1, 373–378 (July 1, 1971).*

Key words: Absorption coefficient; Cl_2; electronic energy; emission; $OCCl_2$; photodissociation; vacuum ultraviolet.

The photodissociation of $OCCl_2$ in the vacuum ultraviolet yields electronically excited Cl_2 producing emission continua in the region 2000–3100 Å. A curve obtained by plotting fluorescence efficiencies as a function of incident wavelength shows diffuse vibrational structure corresponding to the ν_1 symmetric stretching mode of $OCCl_2$, indicating that the process is predissociative. Three main continua at 3063, 2565, and 2460 Å were observed by the photolysis of $OCCl_2$ with the Kr 1236 Å line, while only one continuum at 2580 Å was obtained by the Xe 1470-Å line. From threshold energies of the incident photons to produce each continuum it was possible to obtain electronic energies of excited Cl_2. Electronic energies thus obtained are 7.21 ± 0.05 eV and 7.93 ± 0.03 eV for the upper states associated with the 2580- and 3063-Å continua, respectively. The electronic energy of the upper state responsible for the 2460-Å continuum lies between 7.33 and 8.93 eV. The effect of inert gas on the emission continua was investigated. A comparison has been made of the emission continua obtained by the photolysis of $OCCl_2$ and those produced by an electric discharge of Cl_2. The absorption coefficient of $OCCl_2$ has been measured in the region 1170–1600 Å.

Pilling, M. J., Bass, A. M., Braun, W., **Oscillator strengths of CH_2 and CH_3 in the vacuum ultraviolet,** *Chem. Phys. Letters* **9,** *No. 2, 147–148 (April 15, 1971).*

Key words: Methyl radicals; methylene; oscillator strengths; vacuum UV.

Maximum extinction coefficients and oscillator strength were measured for several CH_2 and CH_3 transitions in the vacuum UV. The method employed involved the vacuum UV flash photolysis of ketene and diazomethane and vacuum UV spectrophotometry.

Reimann, C. W., Zocchi, M., **The crystal structure of *bis*-[μ-(*tri*-1,2,4-triazolo-N¹,N²)-triaquonickel] nickel hexanitrate dihydrate, $[(H_2O)_3(C_2H_3N_3)_3Ni]_2Ni(NO_3)_6(H_2O)_2$,** *Acta Cryst.* **B27,** *Part 3, 682–691 (March 1971).*

Key words: *Bis*-[μ-(tri-1,2,4-triazolo-N¹, N²)-triaquonickel] nickel hexanitrate dihydrate; trinuclear nickel (II) complex; x-ray structure analysis.

The crystal structure of *bis*-[μ-(tri-1,2,4-triazolo-N¹, N²)-triaquonickel] nickel hexanitrate dihydrate, $[(H_2O)_3(C_2H_3N_3)_3Ni]_2Ni(NO_3)_6(H_2O)_2$, was solved by the Patterson method. This compound crystallizes in the monoclinic system with $a = 14.261$ (8), $b = 11.745$ (6), $c = 14.948$ (8) Å, $\beta = 127.13$ (4)°, space group $P2_1/c$, $\rho_c = 1.84$ g · cm^{-3}, and $Z = 2$. The structure consists of discrete centrosymmetric trinuclear cations, $[(H_2O)_3(C_2H_3N_3)_3Ni]_2Ni^{6+}$, in which the central nickel ion is joined to each terminal nickel ion by three planar triazole molecule bridges. The nickel-nickel distance is 3.737 Å. Three molecules of water complete the octahedral coordination of the terminal nickel ions. The N-H groups in the triazole rings and the coordinated water molecules participate in hydrogen bonding with the nitrate groups and non-coordinating water molecules. All hydrogen atoms in this structure were located in a difference map. Final refinement by three-dimensional anisotropic least-squares analysis resulted in an R value of 0.045 based upon 5201 observed reflections.

Ritter, J. J., Coyle, T. D., Bellama, J. M., **Reactions of diboron tetrahalides with haloolefins. Formation of poly(dihaloboryl) ethanes,** *J. Organometal. Chem.* **29,** *175–184 (1971).*

Key words: Boron; boron subhalides; halides; haloolefines; organoboron compounds; tetrachlorodiborane (4); tetrafluorodiborane (4).

Tetrachlorodiborane (4) reacts with vinyl chloride in 2 : 1 ratio to yield 1,1,2-*tris*(dichloroboryl) ethane and boron trichloride. The reaction appears to be general for a variety of haloölefins. Both B_2Cl_4 and B_2F_4 react similarly with haloethylenes containing halogens heavier than the halogen on the diboron moiety. Evidence has been obtained for a reaction sequence involving addition of B_2X_4 to the haloölefin, elimination of trihaloborane, and subsequent addition of B_2X_4 to the resulting vinyldihaloborane.

Sanchez, I. C., DiMarzio, E. A., **Dilute solution theory of polymer crystal growth: A kinetic theory of chain folding,** *J. Chem. Phys.* **55,** *No. 2, 893–908 (July 15, 1971).*

Key words: Chain folding; cilia; localization free energy; nucleation; rate constants.

A kinetic theory of polymer crystallization from dilute solution is formulated for linear chain molecules of finite molecular weight (monodisperse). Two models of crystal growth are considered; both are essentially "regular" chain folding type models. Formulas for the crystal growth rates are derived as a function of the fundamental rate constants associated with the various states of molecular crystallization. These rate constants are evaluated as a function of polymer concentration, molecular weight, crystallization temperature, and crystal thickness. Consideration of finite molecular weight molecules requires an understanding of how these molecules are incorporated into the crystal and what happens to chain ends. Attention is focused on these problems and a description of how "cilia" are formed in polymer crystals is given. A remarkable aspect of cilia formation is that the uncrystallized portion of a chain molecule which dangles in the solution can participate in nucleating a new growth strip (fold plane) on the crystal face—a kind of "self-nucleating" mechanism.

Simmons, J. H., Macedo, P. B., Napolitano, A., Haller, W. K., **Investigation of liquid-liquid phase transitions in oxide melts by viscosity measurements,** *Discussions Faraday Soc., Bristol, England, September 1970, No. 50, 155–165 (1970).*

Key words: Composition fluctuations; glass; immiscibility; phase separation; viscosity; viscous flow.

Results from viscosity measurements conducted above and below the liquid-liquid phase transition of a series of molten oxide glasses are reported in order to analyze the effect of supercritical composi-

tion fluctuations on viscous flow, and to investigate the mechanisms of phase separation. Measurements of four oxide mixtures with similar high temperature structures and widely different critical temperatures, revealed an anomalous increase in viscosity at temperatures above the critical point. The anomalous increase occurs when large composition fluctuations characterizing the critical point are present. The effect is explained in terms of an interaction between viscous flow and the supercritical fluctuations through the structural relaxation process. An analysis of this interaction is presented.
Measurements conducted at temperatures slightly below the critical point of one of these glasses indicate that the microstructure resulting from the phase separation is highly sensitive to the preceding heat-treatment. Phase separation by the formation of isolated spheres of the silica-rich component is identified a few degrees below the critical point. Further measurements of viscosity by a fibre elongation method, conducted far below the critical temperature, are reported in order to analyze the growth mechanisms occurring in the separated phases. In this case, the rearrangment stage of phase separation is characterized by a growing interconnected structure.

Simpson, P. A., Ondrejka, A. R., **Improvements to the NBS rf peak-pulse power standard,** *Instrument Society of America Silver Jubilee International Conference and Exhibit, October 26–29, 1970, Philadelphia, Pa., Paper 709–70, 1–7 (Oct. 26–29, 1970).*

Key words: Peak-pulse power measurement; sampling power measurement; solid state switch.

The National Bureau of Standards maintains a standard for measuring rf peak-pulse power. This standard employs a sampling-comparison method in which a solid state diode switch is used to intercompare equal time-interval samples of cw and pulsed rf power. Recently a new type diode switch has been developed which, when coupled with a sensitive peak detection system, has greatly improved the performance of the standard in two general areas.
The first major improvement is in the frequency coverage. The earlier version of the standard used two separate diode switches to cover the frequency bands 300 to 500 MHz and 950 to 1200 MHz. The new diode switch permits measurements to be made over the frequency range 0.1 to 4.4 GHz because of its low VSWR (typically 1.1 or less).
The other major improvement is in the dynamic power range of the system. The basic range of the earlier version was 0.1 to 1.2 W. The new version operates over a power range of 5 mW to 2 W.
This paper reviews the history of the system, describes its performance characteristics, and gives some of its more important constructional details.

Smith, R. V., **Steam-water, critical flow in a venturi,** *Nat. Bur. Stand. (U.S.), Tech. Note 608, 25 pages (July 1971) 35 cents, SD Catalog No. C13.46:608.*

Key words: Critical flow; pressure profile; steam; venturi; water.

This paper is the second part of an analytical and experimental investigation in which the primary object was to test the hypothesis that the flow of the gas phase controls critical and near critical two-phase flow for cases where the gas and liquid flow essentially in separate streams. In the first part of the investigation, a two-component system (air-water) was used. The results presented here substantiate the hypothesis. The analytical results also indicate the use of one dimensional flow equations with reasonably accurate estimates for droplet size and for the drag and heat transfer coefficients (without consideration of mass transfer—vaporization or condensation) describe critical and near-critical flow reasonably well. This indicates that mass transfer may be a secondary effect for these flow conditions.

Smith, S. J., **Lasers and lengths,** *Comments At. Mol. Phys.* **2,** *No. 3, 92–97, August 1970).*

Key words: Coherence; laser stabilization; length; methane; saturated absorption.

We review here developments which strongly suggest that laser stabilization techniques fully complementary to the amazing coherence properties of the laser will ultimately be found. Indeed progress in hand assures an advance more revolutionary than evolutionary, and discussions of a possible redefinition of the standard of length are now beginning to be taken seriously.

Spencer, L. V., **Remarks on the theory of energy deposition in cavities,** *Acta Radiol.* **10,** *No. 1, 1–20 (February 1971).*

Key words: Bragg-gray principle; cavity; detector response functions; dosimetry; electron-energy deposition; gray medal; ionization.

One can view the problem of energy deposition by fast electrons in cavities in terms of processes occurring throughout the cavity volume, or in terms of an energy deposition function for electrons at initial appearance in the cavity. These two points of view lead to alternative but closely connected statements of the problem. Bragg and Gray apparently had view-point differing in this regard, and more recent work can be better understood in terms of the same dichotomy of view-points. Mathematical development of these points of view proceeds from a general cavity integral expression.

White, H. S., Jr., **Metropolitan Statistical Areas,** *Nat. Bur. Stand. (U.S.), Fed. Info. Process Stand. Publ. (FIPS Pub.) 8–1, 7 pages (1971) 10 cents, SD Catalog No. C13.52:8–1. Supersedes FIPS PUB 8, June 9, 1969.*

Key words: Computers; data processing; national government; Federal Information Processing Standards Publication; Standard Metropolitan Statistical Areas; representations and codes.

This publication provides identification and codes for representing Standard Metropolitan Statistical Areas. It supersedes FIPS PUB 8, same title, dated June 9, 1969. The general concept of a Standard Metropolitan Statistical Area is one of an integrated economic and social unit with a recognized large population nucleus.

Yokel, F. Y., **Stability and load capacity of members with no tensile strength,** *J. Struct. Div. Am. Soc. Civil Engineers* **97,** *No. ST7, 1913–1926 (July 1, 1971).*

Key words: Buckling; compression members; concrete; deflection; equilibrium; load eccentricity; masonry; section cracking; stability; stress distribution; unreinforced concrete.

Information Retrieval Abstract

A mathematical solution is derived, which permits the computation of critical load, deflection and stresses for eccentrically loaded slender prismatic compression members, made of materials that have compressive strength but no tensile strength. A graphical presentation of the solution facilitates its application. In an example of application the solution is used to compute the strength of masonry walls which were tested by the Structural Clay Products Institute. Even though there are limitations to our ability to predict the behavior of a complex material such as masonry by a mathematical solution based on a simplified model, there is good agreement between computed and measured strength.

Civil Engineering Abstract

A mathematical solution is derived which permits the computation of critical load, deflection and stresses for eccentrically loaded slender prismatic compression members, made of materials that have compressive strength but no tensile strength. The solution is applied to predict the strength of masonry walls which were tested by the Structural Clay Products Institute. There is good agreement between computed and measured strength.

Barnes, J. A., **A non-mathematical discussion of some basic concepts of precise time measurement,** *Frequency* **2,** *No. 2, 1–6 (Tracor, Inc., Austin, Texas, May 1971).*

U.S. GOVERNMENT PRINTING OFFICE : 1971 OL—448–417

UNITED STATES
GOVERNMENT PRINTING OFFICE
PUBLIC DOCUMENTS DEPARTMENT
WASHINGTON, D.C. 20402

OFFICIAL BUSINESS
PENALTY FOR PRIVATE USE, $300

U.S. DEPARTMENT OF COMMERCE
POSTAGE AND FEES PAID

U.S.MAIL

JOURNAL OF RESEARCH of the National Bureau of Standards
A. Physics and Chemistry

Vol. 76A, No. 1 January–February 1972

Contents

Page

The absorption spectra of krypton and xenon in the wavelength range 330–600 Å. K. Codling and R. P. Madden. 1

A reference calorimeter for laser energy measurements. E. D. West, W. E. Case, A. L. Rasmussen, and L. B. Schmidt. 13

Accurate calculations of properties of the two-tube electrostatic lens. I. Improved digital methods for the precise calculation of electric fields and trajectories. S. Natali, D. Di Chio, and C. E. Kuyatt. 27

Dielectric constant of compressed gaseous and liquid oxygen. B. A. Younglove. 37

Thermal analysis of calcium sulfate dihydrate and supposed α and β forms of calcium sulfate hemihydrates from 25 to 500° C. James R. Clifton. 41

Modulus of natural rubber cross-linked by dicumyl peroxide. I. Experimental observations. Lawrence A. Wood, George W. Bullman, and George E. Decker. 51

Publications of the National Bureau of Standards. 61

UNIVERSITY MICROFILMS INC

Library of Congress Catalog Card Number: 62–37059

For sale by the Superintendent of Documents, U.S. Government Printing Office, Washington, D.C. 20402. (Order by SD Catalog No. C 13.22/sec.A:76/1). Single copy price varies. This issue $1.25 Subscription price: $9.50 a year; $2.25 additional for foreign mailing.

UNITED STATES GOVERNMENT PRINTING OFFICE, WASHINGTON : 1972